

Master thesis : Image Smoothing in Neuroimaging: Effect of Gaussian vs. Tissue-Specific Approaches on Statistical Analysis

Auteur : Jacquemin, Antoine

Promoteur(s) : Phillips, Christophe

Faculté : Faculté des Sciences appliquées

Diplôme : Master en ingénieur civil biomédical, à finalité spécialisée

Année académique : 2024-2025

URI/URL : <http://hdl.handle.net/2268.2/22438>

Avertissement à l'attention des usagers :

Tous les documents placés en accès ouvert sur le site le site MatheO sont protégés par le droit d'auteur. Conformément aux principes énoncés par la "Budapest Open Access Initiative"(BOAI, 2002), l'utilisateur du site peut lire, télécharger, copier, transmettre, imprimer, chercher ou faire un lien vers le texte intégral de ces documents, les disséquer pour les indexer, s'en servir de données pour un logiciel, ou s'en servir à toute autre fin légale (ou prévue par la réglementation relative au droit d'auteur). Toute utilisation du document à des fins commerciales est strictement interdite.

Par ailleurs, l'utilisateur s'engage à respecter les droits moraux de l'auteur, principalement le droit à l'intégrité de l'oeuvre et le droit de paternité et ce dans toute utilisation que l'utilisateur entreprend. Ainsi, à titre d'exemple, lorsqu'il reproduira un document par extrait ou dans son intégralité, l'utilisateur citera de manière complète les sources telles que mentionnées ci-dessus. Toute utilisation non explicitement autorisée ci-avant (telle que par exemple, la modification du document ou son résumé) nécessite l'autorisation préalable et expresse des auteurs ou de leurs ayants droit.

Image Smoothing in Neuroimaging: Effect of Gaussian vs. Tissue-Specific Approaches on Statistical Analysis

Antoine Jacquemin

Thesis presented to obtain the degree of :
Master of Science in Biomedical Engineering

Thesis supervisor :
Prof. Christophe Phillips

Academic year: **2024 - 2025**

Acknowledgments

The completion of this master's thesis marks a significant milestone in my academic studies at the Faculty of Applied Sciences of the University of Liège. These years of study in biomedical engineering have been enriching, not only in terms of the knowledge acquired but also through the human experiences and challenges encountered along the way.

First, I wish to express my deepest gratitude to my supervisor, Professor Christophe Phillips, for his guidance, insightful advice and the time he generously devoted to me. His expertise and enthusiasm for research and for my master thesis have been a constant source of motivation and inspiration. He made me feeling very welcome in his research team. This inclusion has been an invaluable resource for the work I present today.

I would also like to extend my thanks to the members of my jury, Professor Pierre Sacré and Professor Mohamed Ali Bari, for their interest in my work, their enthusiasm and the time they dedicated to evaluating this thesis.

I am deeply grateful to the *Development in Neuroimaging Data Acquisition and Modeling Laboratory* at the *Cyclotron Research Centre - In Vivo Imaging Unit* for welcoming me into such a stimulating and innovative environment. To the entire CRC team, I extend my thanks for their warm hospitality, friendly atmosphere and for sharing their diverse and enriching experiences that made this work unique. Additionally, I would like to thank professors and members of the Faculty of Applied Sciences of the University of Liège. These five years of study have provided me with a solid foundation of theoretical and practical skills that will accompany me throughout my career.

I would like to express my gratitude to Professor Martina Callaghan from the *Wellcome Trust Centre for Neuroimaging, UCL Institute of Neurology, London, UK*, for her support in sharing data and code, which significantly contributed to the completion of this work. I am also grateful to the *hMRI Group* for their expert and insightful discussions, which greatly stimulated my thinking and deepened my understanding of the topics addressed in this project.

On a personal note, I would like to express my heartfelt gratitude to my family for their unwavering support. They have been my rock throughout these studies. I am especially thankful to my parents for always believing in me and enabling me to pursue these wonderful studies. They have been my foundation, offering strength during challenging times and celebrating my successes during brighter moments. Their presence has been essential to my growth and the successful completion of these studies.

Finally, I would like to thank all my friends who have supported me throughout these studies, through sharing experiences, successful collaborations in forming strong and cohesive teams, all the hours of sports spent together, or simply by all the good times we shared. I feel incredibly fortunate to be surrounded by such inspiring and caring persons.

Quote

"Verum enim vero quum omnes mensurationes atque observationes nostrae nihil sint nisi approximationes ad veritatem, idemque de omnibus calculis illis innitentibus valere debeat, scopum summum omnium computorum circa phaenomena concreta institutorum in componere oportebit, vt ad veritatem quam proxime fieri potest accedamus." [1]

Gauss, 1809

For it is true that all our measurements and observations are nothing but approximations to the truth, and the same must be true of all calculations based on them, that the highest aim of all computations concerning the phenomena of concrete institutions will be to set them in order, that we may approach the truth as closely as possible.

English translation

Contents

1	Introduction	1
1.1	Interest in the human brain	1
1.1.1	Brain Anatomy	1
1.1.2	Brain Histology	2
1.2	Magnetic Resonance Imaging (MRI)	2
1.3	Statistical Analysis & Computational Tools in Brain Imaging	3
2	State of the Art	5
2.1	Types of MRI techniques	5
2.1.1	Functional MRI (fMRI)	5
2.1.2	Diffusion-Weighted Imaging (DWI)	6
2.1.3	Quantitative MRI (qMRI)	7
2.2	Data Preprocessing in Neuroimaging	9
2.2.1	Realignment	9
2.2.2	Slice Timing Correction	10
2.2.3	Coregistration	10
2.2.4	Tissue Segmentation	11
2.2.5	Normalization	11
2.2.6	Smoothing	12
	Objective	14
3	Data & Methods	15
3.1	Data	15
3.1.1	qMRI	15
3.1.2	fMRI	19
3.2	Smoothing Methods	20
3.2.1	Gaussian Smoothing (GS)	21
3.2.2	Tissue-Weighted Smoothing (TWS)	21
3.2.3	Tissue-Specific smOOthing compeNsated (TSPOON)	23
3.3	Comparison Strategy on the qMRI Dataset	26
3.3.1	Statistical Approaches	26
3.3.2	Differences Induced By Smoothing	29
3.3.3	Brain 1D Profile	30
3.4	Comparison Strategy on the fMRI Dataset	30
4	Analysis & Results	32
4.1	qMRI	32
4.1.1	Results Comparison & Statistical Analysis	32
4.1.2	Differences Induced By Smoothing	46

TABLE OF CONTENTS

4.1.3	Brain 1D Profile	48
4.2	fMRI	56
5	Discussion	60
5.1	Quantitative MRI	60
5.1.1	SPM-Based	60
5.1.2	Smoothed Quantitative Maps -Based	63
5.2	Functional MRI	65
5.3	Global Discussion	65
6	Conclusions & perspectives	68
6.1	Conclusions	68
6.2	Perspectives	69
A	Methods: Additional Discussions & Examples	71
A.1	Discussion on different methods to apply GS	71
A.2	TSPOON: Discussion about Handling Division by Zero	71
A.3	Comparison between Jaccard, Dice & Cohen's kappa	72
A.4	Additional Information: One-Sample T-Test & F-Test	74
A.4.1	One-Sample T-Test Pipeline	74
A.4.2	F-Test Pipeline	75
B	Additional qMRI Results	77
B.1	Comparing Results	77
B.2	Effective Smoothing	82
B.3	Similarity Metrics	83
B.4	Threshold Scatter Plot	84
B.5	Brain 1D: merged signals	86
C	Additional fMRI Results	89
D	Additional Results for Discussion	96
	Bibliography	104

List of Figures

3.1	Overview of the method followed to reproduce and compare the smoothed results by different approaches of the article by Callaghan and al. [2]. Acronyms: qMRIs for quantitative maps and SPMs for statistical parametric maps. The solid arrows represent all the image processing performed in this thesis, while the dotted arrows represent the image processing that was originally performed when designing the article. Information about smoothing can be found in the appropriate Section 3.2.	17
3.2	Overview of the method to preprocess and prepare fMRI data before smoothing. This workflow is applied for each subjects independently.	20
3.3	Construction of the generalized TSPOON denominator (example with GM maps). (a): probability map (input); (b): gaussian smoothed probability map; (c): "majority and above 20%" binary mask; (d): gaussian smoothed mask; (e) gaussian smoothed mask after thresholding at 0.05.	25
3.4	Method overview to observe the spatial differences over all the population between the smoothed images on which a different smoothing method is applied.	31
4.1	Statistical parametric maps identifying regions (red for GM and blue for WM) in which MTsat significantly decreased (AR-) with age at the $p < 0.05$ FWE corrected level. The results are superimposed on the mean MT map for the cohort in MNI space. The four axial slices are located at $z = -11, 10, 33$ and 45 mm, from left to right, as illustrated on the sagittal slice (right). The top row shows results obtained from TSPOON, while the bottom row, the TWS ones.	33
4.2	Statistical parametric maps identifying regions (red for GM and blue for WM) in which PD significantly increased (AR+) with age at the $p < 0.05$ FWE corrected level. The results are superimposed on the mean MT map for the cohort in MNI space. The four axial slices are located at $z = -17, 1, 7$ and 39 mm, from left to right, as illustrated on the sagittal slice (right). The top row shows results obtained from TSPOON, while the bottom row, the TWS ones.	33
4.3	Statistical parametric maps identifying regions (red for GM and blue for WM) in which R1 significantly decreased (AR-) with age at the $p < 0.05$ FWE corrected level. The results are superimposed on the mean MT map for the cohort in MNI space. The four axial slices are located at $z = -14, -3, 5$ and 11 mm, from left to right, as illustrated on the sagittal slice (right). The top row shows results obtained from TSPOON, while the bottom row, the TWS ones.	34
4.4	Statistical parametric maps identifying regions (red for GM and blue for WM) in which R2* significantly increased (AR+) with age at the $p < 0.05$ FWE corrected level. The results are superimposed on the mean MT map for the cohort in MNI space. The four axial slices are located at $z = -5, 5, 57$ and 74 mm, from left to right, as illustrated on the sagittal slice (right). The top row shows results obtained from TSPOON, while the bottom row, the TWS ones.	34

4.5	Mean FWHM for TWS and TSPOON indicating the effective smoothing applied to the contrast images. These values are the same for all SPMs (AR+, AR- and AR) for each combination of qMRI parameter and tissue class. The mean value was calculated using the (x,y,z) components of FWHM. Full results are displayed in Appendix in Table B.1. . . .	37
4.6	Bland-Altman plots (GM on the left and WM on the right) comparing the T-values of the AR- statistical parametric maps for the MTsat parameter obtained using TWS and TSPOON.	38
4.7	Bland-Altman plots (GM on the left and WM on the right) comparing the T-values of the AR+ statistical parametric maps for the PD parameter obtained using TWS and TSPOON.	38
4.8	Bland-Altman plots (GM on the left and WM on the right) comparing the T-values of the AR- statistical parametric maps for the R1 parameter obtained using TWS and TSPOON.	39
4.9	Bland-Altman plots (GM on the left and WM on the right) comparing the T-values of the AR+ statistical parametric maps for the R2* parameter obtained using TWS and TSPOON.	39
4.10	Scatter plot of AR+ representing the different possible combinations of qMRI parameters and tissue class. The coordinates of these points represent the threshold above which a voxel will be considered significant depending on the smoothing method (TWS and TSPOON here). In the order of position starting from the origin of the graph: R1-WM, R2*-WM MTsat-WM, PD-WM, PD-GM, R2*-GM, R1-GM, MTsat-GM and the order is the same for AR+, AR- and AR.	43
4.11	Logarithmic distribution in base 10 followed by the sizes of distinct clusters in the case of an increase in R2* parameter in GM from the AR+ statistical parameter map smoothed with TSPOON.	44
4.12	Statistical parametric maps in MNI space showing regions where MTsat maps are significantly affected by the difference between TWS and TSPOON, at the $p < 0.001$ uncorrected level. Regions in red correspond to GM, and regions in blue correspond to WM. Axial sections are displayed in a multislice format at $z = -14, -3, 15$ and 32 mm, from left to right, as illustrated on the sagittal slice (right).	46
4.13	Statistical parametric maps in MNI space showing regions where PD maps are significantly affected by the difference between TWS and TSPOON, at the $p < 0.001$ uncorrected level. Regions in red correspond to GM, and regions in blue correspond to WM. Axial sections are displayed in a multislice format at $z = -14, -3, 15$ and 32 mm, from left to right, as illustrated on the sagittal slice (right).	46
4.14	Statistical parametric maps in MNI space showing regions where R1 maps are significantly affected by the difference between TWS and TSPOON, at the $p < 0.001$ uncorrected level. Regions in red correspond to GM, and regions in blue correspond to WM. Axial sections are displayed in a multislice format at $z = -14, -3, 15$ and 32 mm, from left to right, as illustrated on the sagittal slice (right).	47
4.15	Statistical parametric maps in MNI space showing regions where R2* maps are significantly affected by the difference between TWS and TSPOON, at the $p < 0.001$ uncorrected level. Regions in red correspond to GM, and regions in blue correspond to WM. Axial sections are displayed in a multislice format at $z = -14, -3, 15$ and 32 mm, from left to right, as illustrated on the sagittal slice (right).	47
4.16	1D profile selected in the warped MTsat map in MNI space of the first subject according to axial and sagittal cuts.	48
4.17	Brain 1D profile warped into MNI space for MTsat parameter, subject 1. Graph A show WTA masks. Graphs B and D show the TWS and TSPOON denominator signals and the tissue density signal. Graphs A and E show the TWS and TSPOON smoothed signals and the original one. The results are showed in both GM and WM.	50

4.18	Brain 1D profile warped into MNI space for PD parameter, subject 1. Graph A show WTA masks. Graphs B and D show the TWS and TSPOON denominator signals and the tissue density signal. Graphs A and E show the TWS and TSPOON smoothed signals and the original one. The results are showed in both GM and WM.	51
4.19	Brain 1D profile warped into MNI space for R1 parameter, subject 1. Graph A show WTA masks. Graphs B and D show the TWS and TSPOON denominator signals and the tissue density signal. Graphs A and E show the TWS and TSPOON smoothed signals and the original one. The results are showed in both GM and WM.	52
4.20	Brain 1D profile warped into MNI space for R2* parameter, subject 1. Graph A show WTA masks. Graphs B and D show the TWS and TSPOON denominator signals and the tissue density signal. Graphs A and E show the TWS and TSPOON smoothed signals and the original one. The results are showed in both GM and WM.	53
4.21	Brain 1D Profile for R1 parameter, subject 1: TWS and TSPOON smoothed and merged signals.	55
4.22	Quantitative maps warped into MNI space and smoothed using TWS (top image) and TSPOON (bottom image) for subject 1 and MTsat parameter. The four axial slices are located at $z = -18, -3, 17$ and 37 mm, from left to right, as illustrated on the sagittal slice (right).	56
4.23	Data on the statistical parametric map showing regions where the contrast map <i>Faces</i> > <i>Scrambled Faces</i> is significantly affected by the smoothing methods in GM, at the $p < 0.001$ uncorrected level.	57
4.24	Data on the statistical parametric map showing regions where the contrast map <i>Faces</i> > <i>Scrambled Faces</i> is significantly affected by the smoothing methods in WM, at the $p < 0.001$ uncorrected level.	58
4.25	Statistical parametric maps identifying regions (red for GM and blue for WM) in which the contrast map <i>Faces</i> > <i>Scrambled Faces</i> is significantly affected by the smoothing methods, at the $p < 0.001$ uncorrected level. The results are superimposed on the mean T1w anatomical map for the cohort in MNI space. The four axial slices are located at $z = -31, 17, 28$ and 47 mm, from left to right, as illustrated on the sagittal slice (right). . .	59
A.1	The image on the right shows the contrast smoothed by <i>spm_smooth</i> , while the one on the left is smoothed with <i>imgaussfilt3</i>	72
B.1	Statistical parametric maps identifying regions (red for GM and blue for WM) in which MTsat significantly decreased (AR-) with age at the $p < 0.05$ FWE corrected level. The results are superimposed on the mean MT map for the cohort in MNI space. The four coronal slices are located at $z = -47, -16, 0$ and 31 mm, from left to right, as illustrated on the sagittal slice (right). The top row shows results obtained from TSPOON, while the bottom row, the TWS ones.	78
B.2	Statistical parametric maps identifying regions (red for GM and blue for WM) in which R2* significantly increased (AR+) with age at the $p < 0.05$ FWE corrected level. The results are superimposed on the mean MT map for the cohort in MNI space. The four coronal slices are located at $z = -21, -15, -3$ and 9 mm, from left to right, as illustrated on the sagittal slice (right). The top row shows results obtained from TSPOON, while the bottom row, the TWS ones.	79
B.3	Statistical parametric maps identifying regions (red for GM and blue for WM) in which R2* significantly decreased (AR-) with age at the $p < 0.05$ FWE corrected level. The results are superimposed on the mean MT map for the cohort in MNI space. The four axial slices are located at $z = -29, 6, 9$ and 28 mm, from left to right, as illustrated on the sagittal slice (right). The top row shows results obtained from TSPOON, while the bottom row, the TWS ones.	80

B.4	Statistical parametric maps identifying regions (red for GM and blue for WM) in which PD significantly decreased (AR-) with age at the $p < 0.05$ FWE corrected level. The results are superimposed on the mean MT map for the cohort in MNI space. The four axial slices are located at $z = -7, 9, 26$ and 63 mm, from left to right, as illustrated on the sagittal slice (right). The top row shows results obtained from TSPOON, while the bottom row, the TWS ones.	81
B.5	Jaccard index, Dice coefficient and Cohen's kappa between the significant regions ($p < 0.05$ FWE corrected level) derived from the corresponding contrast maps (AR+ called T1, AR- called T2 and AR called F3) of TWS and TSPOON for each combination of a qMRI parameter and a tissue class.	83
B.6	Jaccard index, Dice coefficient and Cohen's kappa between TWS and TSPOON for each contrast maps (AR+ called T1, AR- called T2 and AR called F3) of a combination of a qMRI parameter and a tissue class.	84
B.7	Scatter plot of AR- representing the different possible combinations of qMRI parameters and tissue class. The coordinates of these points represent the threshold above which a voxel will be considered significant depending on the smoothing method (TWS and TSPOON here). In the order of position starting from the origin of the graph: R1-WM, R2*-WM MTsat-WM, PD-WM, PD-GM, R2*-GM, R1-GM, MTsat-GM and the order is the same for AR+, AR- and AR.	85
B.8	Scatter plot of AR representing the different possible combinations of qMRI parameters and tissue class. The coordinates of these points represent the threshold above which a voxel will be considered significant depending on the smoothing method (TWS and TSPOON here). In the order of position starting from the origin of the graph: R1-WM, R2*-WM MTsat-WM, PD-WM, PD-GM, R2*-GM, R1-GM, MTsat-GM and the order is the same for AR+, AR- and AR.	86
B.9	Brain 1D Profile for MTsat parameter: TWS and TSPOON smoothed and merged signals.	87
B.10	Brain 1D Profile for PD parameter: TWS and TSPOON smoothed and merged signals.	87
B.11	Brain 1D Profile for R2star parameter: TWS and TSPOON smoothed and merged signals.	88
C.1	Statistical parametric map showing regions where the contrast map <i>Faces > Scrambled Faces</i> is significantly increased by gaussian smoothing in GM, at the $p < 0.001$ uncorrected level.	90
C.2	Statistical parametric map showing regions where the contrast map <i>Faces > Scrambled Faces</i> is significantly increased by gaussian smoothing in WM, at the $p < 0.001$ uncorrected level.	91
C.3	Statistical parametric map showing regions where the contrast map <i>Faces > Scrambled Faces</i> is significantly increased by TWS in GM, at the $p < 0.001$ uncorrected level.	92
C.4	Statistical parametric map showing regions where the contrast map <i>Faces > Scrambled Faces</i> is significantly increased by TWS in WM, at the $p < 0.001$ uncorrected level.	93
C.5	Statistical parametric map showing regions where the contrast map <i>Faces > Scrambled Faces</i> is significantly increased by TSPOON in GM, at the $p < 0.001$ uncorrected level.	94
C.6	Statistical parametric map showing regions where the contrast map <i>Faces > Scrambled Faces</i> is significantly increased by TSPOON in WM, at the $p < 0.001$ uncorrected level.	95
D.1	Statistical parametric maps showing regions where R2* is affected by the difference between TWS and TSPOON in gray matter.	96
D.2	Statistical parametric maps showing regions where R2* is affected by the difference between TWS and TSPOON in white matter.	97
D.3	Quantitative map for subject 1 and MTsat qMRI parameter showing the difference TWS and TSPOON in the white matter.	97

D.4 Quantitative map for subject 1 and R2* qMRI parameter showing the difference TWS and TSPOON in the white matter. 98

D.5 Statistical parametric maps showing regions where MTsat is significantly affected by the difference between TWS and TSPOON, at the $p < 0.05$ FWE corrected level. Regions in red correspond to GM, and regions in blue correspond to WM. Axial sections are displayed in a multislice format. 98

List of Tables

4.1	Age-related effect for qMRI parameters and brain matters. The age-related increase is written AR+ while the age-related decrease AR-.	36
4.2	Jaccard index, Dice coefficient and Cohen's kappa between the significant regions ($p < 0.05$ FWE corrected level) derived from the corresponding statistical parameter maps (AR+ and AR-) of TWS and TSPOON for each combination of a qMRI parameter and a tissue class.	41
4.3	T-value threshold at $p < 0.05$ FWE corrected level for TWS and TSPOON for AR+ and AR- SPM. These values are the same both for AR+ and AR- SPM.	42
4.4	Tables showing the number of significant voxels ($p < 0.05$ FWE corrected level), the number of clusters they form, as well as the median size of these clusters for each combination of qMRI parameter and tissue class. Each table is related to a smoothing method (TWS or TSPOON) and a statistical parametric map (AR+ or AR-).	45
B.1	FWHM for TWS and TSPOON indicating the effective smoothing applied to the contrast images. These values are the same for all contrasts (AR+, AR- and AR) for each combination of qMRI parameter and tissue class.	82
B.2	F-value threshold at $p < 0.05$ FWE corrected level for TWS (left) and TSPOON (right) for AR.	86

Chapter 1

Introduction

1.1 Interest in the human brain

The human brain, an organ of immense complexity and beauty, serves as the control center for all bodily functions, emotions, thoughts, and actions. It is the most complex structure known to science, even yet it only weighs around 1.35 kg and is mostly made up of proteins, water and fat. Comprising billions of neurons connected through intricate networks, the brain processes information through electrical and chemical signals. These neural communications underpin every aspect of our existence, from the basic functions of breathing and heartbeat regulation to sophisticated cognitive processes such as decision-making, learning and memory [3].

1.1.1 Brain Anatomy

The human brain is a complex and well-organized system that embodies an impressive balance of complexity and efficiency. Its anatomy demonstrates an intelligent structure designed to conduct a wide range of functions, from the most basic reflexes to the most sophisticated kinds of reasoning. At its heart, the brain functions as the human body's command and control center, integrating sensory inputs, interpreting information, and orchestrating reactions with precision. This complex organ functions on two levels: a decisional level, which governs conscious cognition and purposeful actions, and an execution level, which unconsciously manages a wide range of activities and interactions between brain centers. Understanding the brain's anatomical design is critical for understanding its operation, as each morphological characteristic is inextricably linked to its role in sustaining life and developing human potential [4].

The brain is made up of three types of tissues, each with a different anatomical and functional role: gray matter (GM), white matter (WM) and cerebrospinal fluid (CSF) [4] [5].

- **Gray Matter (GM):** This tissue primarily consists of neuronal cell bodies, dendrites, and synapses. It is the seat of computation and processing in the brain, playing a pivotal role in sensory perception, muscle control, memory, and decision-making. Found predominantly in the cerebral cortex and subcortical nuclei, gray matter forms the brain's functional hub, enabling complex cognitive and motor functions.
- **White Matter (WM):** White matter is composed of myelinated axons that create an intricate network of connections between different brain regions. Myelin, a lipid-rich sheath surrounding axons, gives this tissue its characteristic white appearance and facilitates rapid electrical signal transmission. White matter ensures efficient communication between gray matter areas and integrates information across the brain.
- **Cerebrospinal Fluid (CSF):** CSF is a clear, colorless liquid that circulates within the brain's ventricular system and the subarachnoid space surrounding the brain and spinal cord. It provides mechanical

protection, acting as a cushion against external impacts, and contributes to homeostasis by removing metabolic waste, delivering nutrients, and maintaining a stable environment for neural tissues.

1.1.2 Brain Histology

Prior to the development of contemporary imaging techniques such as structural magnetic resonance imaging (MRI), the study of the brain was mainly based on histological investigation of postmortem human tissue. By examining brain parts under a microscope, researchers were able to gain extensive insights into the structure and composition of neural tissues. This method was critical in determining the cellular and molecular basis of a variety of neurological diseases, including Alzheimer's disease. It allowed scientists to identify crucial pathological features like amyloid plaques, neurofibrillary tangles, and aberrant tau protein phosphorylation, paving the way for a better understanding of the disease's course [6].

Histology, however, has its limitations. The invasive nature of the technique required access to post-mortem tissues, often making longitudinal studies of brain changes in living individuals impossible. Additionally, histology lacked the ability to provide a global view of the brain's architecture and function in its entirety. These constraints prompted the need for non-invasive methods to study the living brain, leading to the development and widespread adoption of structural MRI.

Structural MRI revolutionized neuroscience by enabling high-resolution, three-dimensional imaging of the brain in vivo [5]. Unlike histology, MRI provides a non-invasive approach to examine the brain's anatomy, allowing researchers to study structural variations and monitor changes over time. With its ability to differentiate between gray matter, white matter, and cerebrospinal fluid, MRI became an essential tool for mapping the brain's complex architecture and identifying early markers of diseases like Alzheimer's. Moreover, MRI paved the way for a deeper understanding of how structural abnormalities correlate with clinical symptoms and cognitive decline.

The transition from histological studies to MRI exemplifies the evolution of neuroscience from descriptive postmortem analyses to dynamic and non-invasive exploration of living systems. This paradigm shift has not only expanded our ability to investigate brain disorders but also fostered new approaches to early diagnosis and intervention, significantly enhancing our understanding of the brain's structure and function [4].

1.2 Magnetic Resonance Imaging (MRI)

MRI has revolutionized neuroscience and clinical medicine by providing a non-invasive window into the intricate architecture of the human brain. Utilizing strong magnetic fields and radio waves, MRI enables the visualization of both structural and functional aspects of the brain with precision. Structural MRI, in particular, has been a cornerstone in understanding brain morphology, allowing researchers and clinicians to quantify and map variations in gray and white matter across individuals. These insights have proved critical in advancing our knowledge of normal brain development, neurological disorders, and even subtle variations linked to individual differences in behavior and cognition [4].

A notable strength of structural MRI lies in its ability to uncover patterns and anomalies that might otherwise remain undetected. For instance, a study of over 2,500 healthy young males revealed that intracranial abnormalities such as arachnoid cysts and vascular malformations occur at rates higher than previously expected, despite their minimal impact on health for most individuals. These findings not only highlight the importance of routine imaging in specific populations, such as military pilots, but also underscore MRI's role in identifying silent conditions that might predispose individuals to future neurological

issues [7].

MRI has also paved the way for exploring brain-behavior relationships, as exemplified by studies linking social network size to structural variations in regions like the amygdala. This work has provided fascinating insights into how our social lives are mirrored in the architecture of our brains. For example, while earlier studies like those of Bickart et al. demonstrated a correlation between amygdala volume and the size of real-world social networks, subsequent research extended this association to online networks, highlighting a convergence between digital and physical social interactions. Intriguingly, regions like the superior temporal sulcus and entorhinal cortex have been implicated in online social networking, suggesting distinct neural substrates for different dimensions of sociality [8]. Moreover, the use of advanced MRI techniques, such as high-field imaging at 7 Tesla, has further refined our ability to detect subtle variations in brain structure. These methods have been instrumental in replication studies of small-effect phenomena, such as the link between amygdala gray matter volume and social behaviors [9].

MRI also serves as a tool for uncovering the unexpected and ethically profound. For instance, the application of functional MRI (fMRI) in patients diagnosed as vegetative has revealed preserved brain function in some cases, challenging traditional diagnostic criteria. These discoveries have opened doors to new methods of communication with non-verbal patients, where task-dependent neural activation can serve as evidence of conscious awareness. This remarkable intersection of structural and functional imaging demonstrates the versatility of MRI as both a diagnostic tool and a means of exploring the frontiers of human consciousness [10].

Futhermore, MRI has been recognized as a highly sensitive tool in the detection of acute intracerebral abnormalities, often outperforming other imaging techniques like computed tomography (CT) in specific contexts. For instance, Kidwell et al. (2004) demonstrated the superior accuracy of MRI in detecting acute intracerebral hemorrhages compared to CT in patients presenting with stroke symptoms. Their findings highlighted MRI's ability to provide detailed insights into brain pathology within critical diagnostic windows, thereby underscoring its value not only in routine neuroimaging but also in emergency medical settings. This capacity for precise and timely diagnostics has established MRI as a cornerstone of modern brain imaging [11].

Through its capacity to illuminate the unseen, MRI has not only enhanced our understanding of the brain's structure and function but also provoked deeper questions about the nature of individuality, sociality, and consciousness. To fully leverage the potential of MRI, particularly in advanced modalities such as multiparametric mapping (MPM), reducing noise and increasing the signal-to-noise ratio (SNR) is critical [4] [5]. A higher SNR improves the accuracy and reliability of data, enabling clearer insights into subtle brain structures and functions. Techniques such as spatial smoothing can play a pivotal role in this process by effectively reducing noise, thereby boosting SNR and enhancing the quality of imaging data. This balance between detail preservation and noise reduction underscores MRI's indispensable role in both clinical and research settings, as it continues to reveal the brain's enigmatic complexity.

1.3 Statistical Analysis & Computational Tools in Brain Imaging

The increasing complexity and scale of modern neuroscience research necessitate robust statistical analyses and computational tools to process and interpret imaging data effectively. In studies involving tens or even hundreds of subjects, manual analysis is neither practical nor reliable, making the use of advanced algorithms and software indispensable. These tools allow to extract meaningful insights from vast datasets, uncover patterns across populations and establish statistically significant relationships between brain structure, function and behavior [12].

One of the key challenges in such studies is the variability in individual brain anatomy and the subtlety of the differences being investigated. To address this, image preprocessing techniques, such as spatial normalization, segmentation and smoothing, are employed. Spatial normalization ensures that brain images from different individuals are aligned to a standard template, allowing voxel-wise comparisons across subjects. Segmentation enables the differentiation of brain tissues (GM, WM and CSF), while smoothing enhances signal-to-noise ratio (SNR) by averaging data across neighboring voxels, thereby mitigating noise and improving the detection of underlying patterns [13] [14].

Image smoothing, in particular, plays a critical role in statistical parametric mapping (SPM) and other voxel-based analyses [15]. By applying Gaussian filters to the imaging data, smoothing helps to increase statistical power, reduce false positives and accommodate anatomical variability across individuals. This preprocessing step is especially vital when analyzing large cohorts, where subtle effects may otherwise be obscured by noise or inter-subject differences. The present work focuses on this specific aspect, highlighting its significance in ensuring the reliability and robustness of findings in neuroimaging studies[16].

Moreover, the vast quantities of imaging data generated in such studies demand high-performance computational infrastructure. Software tools like Statistical Parametric Mapping (SPM) [17], FMRIB Software Library (FSL) (where FMRIB stands for the Oxford Centre for Functional MRI of the Brain) [18] and Analysis of Functional NeuroImages (AFNI) [19] have become standard in the field, enabling automated processing pipelines that integrate multiple preprocessing steps, statistical analyses and visualization techniques. These platforms allow researchers to manage large-scale datasets efficiently, perform complex analyses and validate results across diverse conditions and populations.

The combination of sophisticated computational tools and rigorous statistical methods has not only facilitated the exploration of brain-behavior relationships but also advanced our understanding of neurological and psychiatric disorders. By integrating image preprocessing techniques such as smoothing, this work contributes to the ongoing effort to refine imaging methodologies and enhance the reproducibility of findings in the field of brain imaging. This foundation sets the stage for the subsequent analysis and discussion of image smoothing methods, which are pivotal for achieving high-quality results in neuroimaging research.

Chapter 2

State of the Art

2.1 Types of MRI techniques

MRI is a versatile imaging technique. Thanks to the physical principles it relies on and technological developments, one can acquire images whose signal is sensitive to various properties of the brain tissues. An introduction to functional magnetic resonance imaging (fMRI), which measures variations in blood flow to record brain activity, opens this section. This method is essential for mapping neural networks and comprehending how the brain operates. We then explore Diffusion Weighted Imaging (DWI), a technique that highlights the connectivity and integrity of white matter pathways by mapping the diffusion of water molecules in brain tissue. The third technique described here is quantitative MRI (qMRI), which provides maps of microstructural properties in the brain by providing accurate measures of tissue characteristics.

2.1.1 Functional MRI (fMRI)

Functional magnetic resonance imaging (fMRI) is a neuroimaging technique used to investigate brain function by detecting changes in blood oxygenation and flow that occur in response to neural activity [4]. This method relies on the "Blood-Oxygen-Level-Dependent" (BOLD) signal, which measures fluctuations in the ratio of oxygenated and deoxygenated blood as a proxy for neural activity. fMRI has become an essential tool for understanding the human brain's functional organization, offering insights into both intrinsic and task-evoked neuronal processes.

The technique can be broadly categorized into two approaches: resting-state fMRI (rs-fMRI) and task-based fMRI (tb-fMRI). rs-fMRI examines spontaneous neuronal activity while the subject is at rest, revealing patterns of functional connectivity within the brain's intrinsic networks, such as the default mode network (DMN) and the salience network (SN). These networks are critical for baseline brain function, integrating sensory information, and preparing for cognitive tasks. Conversely, tb-fMRI focuses on brain activity elicited by specific tasks, such as motor movements, language processing, or memory recall [5]. By correlating task stimuli with regional BOLD signal changes, tb-fMRI maps brain regions associated with specific cognitive or behavioral functions.

One key application of fMRI lies in studying brain plasticity, the capacity of the brain to reorganize itself in response to injury, learning, or experience. For example, fMRI can reveal changes in functional connectivity patterns following cognitive training, highlighting how new neural networks emerge or existing ones adapt. In clinical contexts, fMRI is used to assess recovery after stroke, monitor neurodegenerative diseases, and evaluate treatment efficacy in psychiatric disorders. By understanding how functional networks adapt, researchers and clinicians can design targeted interventions to support rehabilitation or mitigate disease progression [5].

Despite its immense potential, fMRI has several challenges. The BOLD signal is inherently noisy, influenced by factors such as physiological fluctuations (e.g., respiration and heart rate) and scanner artifacts. Preprocessing steps, including realignment, normalization, and smoothing, are crucial to enhance data quality. Smoothing, typically achieved using a Gaussian kernel, improves the signal-to-noise ratio (SNR) by averaging voxel intensities over a neighborhood. However, this process introduces trade-offs: while smoothing enhances signal detectability, it can blur activation boundaries, merge distinct regions, and obscure fine-grained functional details [20]. This paper, such as those exploring the effects of smoothing on group-level functional connectivity, underscore the importance of kernel size selection. Smoothing influences connectivity metrics, graph-theoretical properties, and analyses like independent component analysis (ICA) and principal component analysis (PCA). For instance, inappropriate kernel sizes may mask subtle differences in functional connectivity or distort network structures. These effects have significant implications for both rs-fMRI and tb-fMRI, where functional connectivity maps must balance noise reduction with preserving spatial resolution.

In sum, fMRI is a cornerstone of modern neuroscience, enabling comprehensive exploration of the brain's functional organization and adaptability. Advances in preprocessing techniques and data analysis continue to refine its accuracy and applicability, offering new avenues for understanding brain plasticity and addressing clinical challenges.

2.1.2 Diffusion-Weighted Imaging (DWI)

Diffusion-weighted imaging (DWI) is a magnetic resonance imaging technique that measures the random motion of water molecules within tissues, providing insights into tissue microstructure. Building upon this, Diffusion Tensor Imaging (DTI) extends the capabilities of DWI, enabling the visualization and quantification of the microstructural integrity of white matter in the brain. Unlike standard imaging techniques, which primarily provide anatomical details, DTI captures the directional movement of water molecules, a phenomenon known as anisotropic diffusion. This characteristic is particularly significant because water molecules preferentially diffuse along axonal fibers in white matter, providing insight into the organization and orientation of these tracts [4].

The metrics derived from DTI, such as fractional anisotropy (FA) and mean diffusivity (MD), are central to understanding its utility. FA measures the degree of directionality in water diffusion, ranging from 0 (completely isotropic) to 1 (highly anisotropic), and reflects the structural coherence of white matter tracts. In contrast, MD quantifies the average magnitude of diffusion, offering insights into overall tissue integrity. These parameters are sensitive to changes in the brain's microenvironment, making DTI an invaluable tool for detecting early signs of pathological processes that may not yet be visible on conventional MRI. For instance, a decrease in FA and an increase in MD are often observed in regions where tumor cells infiltrate white matter, disrupting normal structural patterns.

In the context of glioblastoma (GBM), DTI has emerged as a crucial imaging modality for addressing the limitations of traditional MRI in detecting tumor progression [21]. Conventional MRI struggles to distinguish between infiltrative tumor cells and surrounding edema in non-enhancing regions, complicating early detection and treatment planning. DTI, however, excels in this regard by revealing subtle disruptions in white matter integrity that correlate with tumor invasion. Studies have shown that GBM cells tend to migrate along white matter tracts, mirroring the patterns of anisotropic water diffusion. By capturing these microstructural changes, DTI allows clinicians to identify areas of occult tumor infiltration, even before they become apparent on standard imaging.

Moreover, advanced DTI-derived metrics, such as axial and radial diffusivity, provide additional layers of detail. Axial diffusivity reflects diffusion along the principal direction of white matter fibers, while radial diffusivity measures diffusion perpendicular to this axis. These parameters offer a nuanced understanding of

how GBM alters white matter tracts, enabling the prediction of both local and distant tumor progression. For example, the ability of DTI to map tractography and identify migratory pathways has significant implications for surgical planning, radiotherapy targeting and long-term surveillance. However, the primary limitations of DTI include the simplicity of the model, which fails to capture complex fiber configurations such as crossing fiber bundles and the challenges in biologically interpreting the model and its derived parameters (e.g., FA and MD).

2.1.3 Quantitative MRI (qMRI)

Quantitative Magnetic Resonance Imaging (qMRI) represents a major advance in computational neuroanatomy. Unlike conventional weighted MRI techniques, which produce qualitative images that depend on tissue properties but also on acquisition parameters and site-specific variation, qMRI allows quantification of physical properties of brain tissue in standardized units [22]. This greatly improves comparability across studies, sites, and time periods, while providing increased sensitivity to brain microstructures such as myelin and iron. qMRI is essential for longitudinal studies of neurological development, plasticity, and disease.

qMRI relies on biophysical models of magnetic relaxation and on precise adjustments of the acquisition data, such as instrumental biases (inhomogeneities of the emission and reception fields). By calibrating the measurements, qMRI provides quantitative maps of the intrinsic parameters of the tissues: the longitudinal relaxation rate (R_1), the effective transverse relaxation rate (R_2^*), the proton density (PD) and the saturation by magnetization transfer (MTsat). These parameters, obtained by multiparametric mapping (MPM) protocols, make it possible to link the macroscopic and microscopic properties of the brain to its functioning.

The following parameters are measured by qMRI:

- **Magnetization Transfer Saturation (MTsat):** MTsat measures the amount of bound protons in macromolecules, such as myelin, by quantifying the energy transfer between these protons and those in free water. This parameter is an excellent indicator of myelin density in the white and gray matter of the brain. MTsat analysis allows the study of pathologies affecting myelin, such as multiple sclerosis and the assessment of neuronal connectivity in normal and pathological contexts. MTsat is a semi-quantitative measure typically reported in arbitrary units (AU).
- **Proton Density (PD):** PD measures the proportion of protons available to generate an MR signal. It is directly related to the water content of tissues. PD maps are useful for distinguishing gray, white, and cerebrospinal fluid regions. In clinical neurology, PD is used to identify abnormalities such as edema or myelin loss, while providing a complementary perspective to other qMRI parameters. PD is a quantitative measure expressed as a percentage or in mole fraction.
- **Longitudinal Relaxation Rate (R_1):** R_1 , which corresponds to the inverse of the longitudinal relaxation time T_1 , reflects the speed at which protons aligned by the magnetic field return to their equilibrium state after excitation. It is sensitive to changes in tissue composition, such as myelin and water content. R_1 maps provide quantitative indices of brain tissue density and structure and allow the study of specific regions such as the cortex or basal ganglia with increased precision. R_1 is a quantitative measure expressed in units of s^{-1} .
- **Effective Transverse Relaxation Rate (R_2^*):** R_2^* , the inverse of the effective transverse relaxation time (T_2^*), is particularly sensitive to local variations in magnetic susceptibility, such as those induced by iron or deoxyhemoglobin. This makes it a key tool for studying iron deposits in the brain, which are involved in neurodegenerative diseases such as Parkinson's or Alzheimer's. In functional neuroimaging, R_2^* also contributes to the study of brain activation thanks to its relationship with the BOLD signal. R_2^* is a quantitative measure expressed in units of s^{-1} .

qMRI, combined with advanced biophysical models, paves the way for in vivo histology (hMRI) [23]. This allows the study of brain microstructure non-invasively and with a precision that was previously only possible with ex vivo techniques. The increasing use of open source software such as the hMRI-toolbox [24] facilitates the standardization and access to these methods, expanding their potential in basic and clinical research. These innovations make possible a better understanding of the relationships between brain structure, function and behavior, while improving diagnostic and therapeutic tools.

Using qMRI, the development of multi-center studies offers unique opportunities to analyze subtle effects, explore anatomical variations in global populations, and study rare diseases [25]. However, the success of these studies relies on the reliability and sensitivity of the data obtained, including their comparability between different centers and time points. The article highlights the challenges and solutions associated with the standardization of MRI data, focusing on the innovative approach of quantitative mapping, which allows to obtain precise and reproducible measurements of brain tissue.

In multicenter studies, inter-site variations represent a major challenge. Conventional T1-weighted (T1w) images are often subject to systematic biases between sites, complicating their use for morphometric analyses. Although statistical adjustments can partially compensate for these differences, they do not entirely eliminate the problem. qMRI aims to address this problem by providing absolute and reproducible measurements. However, so far, few protocols have been validated in multicenter settings. The paper [25] describes a rigorous validation of the MPM approach in a multi-center setting, involving three imaging sites and five volunteers. The results show low inter-site variation. This performance exceeds that of traditional T1w, where inter-site bias and variability affect the reliability of the analyses. In addition, MT maps, used to generate gray matter (GM) probabilities, have a higher reproducibility than maps derived from T1w images. This improvement reinforces the interest of quantitative parameters for morphometric studies.

Beyond the technical part, the scope of application of qMRI is very large. A recent study explored the potential of quantitative histological MRI (hMRI) as a biomarker for monitoring high-grade gliomas (HGGs), focusing on its ability to identify regions at risk for tumor recurrence [26]. HGGs are aggressive brain tumors with a poor prognosis due to their tendency to recur despite advances in surgical and therapeutic approaches. Conventional MRI struggles to distinguish between brain tissue microscopically invaded by gliomas and healthy brain parenchyma. By contrast, hMRI provides detailed measurements of brain microstructure through parameters such as MTsat, PD, R1 and R2*. Using hMRI, researchers assessed the perioperative zone (IPZ) around the surgical cavity and identified areas of eventual tumor recurrence (extension zone, EZ) upon follow-up. Parameters were compared across three key regions: the overlap between IPZ and EZ, the peritumoral brain zone outside recurrence and the recurrence zone itself. Results highlight hMRI's sensitivity to microstructural alterations associated with HGG recurrence, providing a potential biomarker for early detection. Unlike traditional MRI, which is limited by its qualitative nature, hMRI's quantitative approach allows for reproducible measurements of physical MR parameters across different participants and imaging systems. This capability positions hMRI as a promising tool for tracking postoperative brain changes and identifying areas at risk of tumor progression well before conventional imaging methods can detect recurrence.

Futhermore qMRI was also used in a recent study exploring brain alterations associated with multiple sclerosis (MS), providing insight into microstructural changes in the brain over a 30-month follow-up period [27]. This approach, using a multiparametric mapping (MPM) protocol, generates four parametric maps (MTsat, PD, R1, and R2*) reflecting physical tissue properties, including iron and myelin content. These parameters provide a detailed view of tissue damage and repair mechanisms in MS. The observations made suggest repair mechanisms involving an increase in axonal density and/or myelin content, as well as a resorption of edema and inflammation. MTsat and R2* parameters, in particular, appear to be

sensitive markers of these repair processes, although they are also influenced by initial demyelination and axonal loss.

The potential of qMRI has been also highlighted in several neurological conditions [28]. In multiple sclerosis (MS), qMRI has revealed microstructural changes in normal-appearing white and gray matter that are undetectable with traditional methods. These changes, including increased T1, T2, and PD values and decreased MTR, correlate with disease progression and patient cognitive status. Importantly, these alterations have been observed even in the early stages of MS, emphasizing qMRI's utility for early diagnosis and tracking subtle disease-related changes over time. In epilepsy, qMRI has been instrumental in identifying epileptogenic lesions such as focal cortical dysplasia (FCD) and quantifying hippocampal damage in temporal lobe epilepsy (TLE). Advanced qMRI techniques, including T1/T2 mapping and surface-based analyses, have improved lesion visualization and diagnostic accuracy, even in patients whose conventional MRI appears normal. These advancements enhance the identification of seizure onset zones and other critical regions, addressing one of the key challenges in epilepsy diagnostics.

To conclude this section, although qMRI is extremely promising, there are technical limitations to consider, including long acquisition times and the need for advanced data processing to mitigate potential biases. Despite these challenges, the reproducibility and sensitivity of qMRI make it an invaluable tool for multi-center studies and longitudinal research. Its ability to provide a comprehensive characterization of microstructural tissue integrity positions it as a critical advancement in the field of neuroimaging, with far-reaching implications for understanding and treating neurological diseases.

2.2 Data Preprocessing in Neuroimaging

Data preprocessing in neuroimaging is an essential step to ensure the quality and comparability of results. Brain images, whether from anatomical MRI, functional imaging (fMRI), diffusion weighted imaging (DWI) or quantitative imaging (qMRI), often contain artifacts and unwanted variations due to physiological factors (respiratory movements, heartbeats) or technical factors (equipment noise, magnetic field inhomogeneity). Preprocessing aims to minimize these sources of errors while aligning the data to a standardized space to allow inter- and intra-subject comparisons [5].

2.2.1 Realignment

Head movement, during a single run and head position between runs can disrupt the spatial consistency of acquired images. Such motion results in the misalignment of the brain's position across images, potentially leading to errors like voxels containing mixed tissue signals or data loss, particularly at the image volume edges. Additionally, head motion alters the magnetic field uniformity, which has been finely shimmed for a specific head position and can disrupt the timing and pattern of slice-specific excitation pulses. To address these issues, motion correction techniques aim to adjust the image series, typically fMRI and DWI, ensuring the brain appears consistently positioned across all volumes. It is important to note that this discussion pertains to images of the same modality and nature, often involving one or multiple series of fMRI or DWI scans.

The process of realignment [29] [30] employs co-registration, a technique that spatially aligns successive image volumes in a time series to a chosen reference volume using rigid-body transformation. This method assumes identical size and shape for the volumes, requiring adjustments through three translational and three rotational parameters. Algorithms determine the optimal transformation by minimizing differences between volumes, quantified via a cost function that calculates voxel-by-voxel intensity discrepancies. Once the best-fit parameters are established, the original data are resampled through spatial

interpolation to estimate the values that would have been captured in a motion-free scenario.

Selecting the appropriate reference volume is critical. In fMRI common choices include the first usable volume, often minimally affected by movement, or an average volume. While the first volume closely reflects the initial anatomical scan, an average volume incorporates broader information. However, since an average derived from unaligned volumes may pose challenges, two-pass averaging methods are employed to iteratively refine alignment.

In addition to realignment, motion-related artifacts can be mitigated by regressing out motion parameters during statistical analysis. By incorporating these parameters—typically six regressors representing translational and rotational movements—into the General Linear Model (GLM), residual motion effects can be accounted for. Many workflows combine both approaches, using preprocessing realignment alongside motion regressors to ensure robust correction. This comprehensive approach to motion correction enhances the reliability and interpretability of neuroimaging data, maintaining spatial fidelity and reducing confounding artifacts introduced by head movement.

2.2.2 Slice Timing Correction

During MRI acquisitions, the brain is scanned slice by slice throughout the repetition time (TR), which can last several seconds (typically 3s for fMRI and DWI). Slices are typically acquired using either ascending/descending order (sequential acquisition) or an interleaved order, where odd-numbered slices are collected first, followed by even-numbered slices. Interleaved acquisition minimizes cross-slice excitation but introduces temporal discrepancies between adjacent slices within a single TR [31].

These discrepancies mean that different parts of the brain are sampled at slightly different times. For example, the BOLD signal in slices acquired late in the TR may appear temporally shifted compared to slices acquired earlier, even though the underlying neural activity is synchronous. If left uncorrected, this timing mismatch can distort the temporal alignment of signals across slices, complicating the interpretation of brain activity over time. Ideally, we aim to align the signal across all slices to represent the same moment within the TR.

Slice timing correction [31] resolves this issue using temporal interpolation, which estimates the signal for each slice as if it had been acquired at a common reference time point. The reference is often the acquisition time of the first slice or the midpoint of the TR. While choosing the first slice simplifies subsequent analyses, selecting the midpoint reduces interpolation requirements, as the maximum timing discrepancy is halved. Sinc interpolation, a widely used method, leverages data from neighboring time points to reconstruct the signal for each slice.

The necessity of slice timing correction can depend on the experimental design and TR length. For shorter TRs, the sluggish nature of the hemodynamic response may make correction less critical. However, studies [32] suggest that while slice timing correction may not always dramatically change results, it frequently enhances accuracy, particularly in event-related designs.

Slice timing correction is inherently constrained by variability in experimental data, especially noise unrelated to the task. An alternative approach involves creating separate analysis models for each slice, incorporating timing discrepancies into the analysis rather than preprocessing.

2.2.3 Coregistration

Another preprocessing step in neuroimaging is coregistration [33] [34], which spatially aligns images of different nature acquired from the same subject. Functional activity can be mapped onto anatomical

structures thanks to this method, which ensures that functional and structural images from the same person are precisely aligned.

The fundamental disparities between images of different modalities, e.g. functional and anatomical images, from the same subject render their alignment difficult. While functional images are usually blurrier, of lower resolution and more prone to geometric aberrations, structural images offer high-resolution, well defined anatomical boundaries. By optimizing a cost function, the coregistration method reduces disparities between the two image types in order to get around these issues. Complex distortions in functional data may require more sophisticated algorithms or additional parameters for scaling along the x, y, or z axes, even though rigid-body transformations with six parameters (translation and rotation) are adequate for simpler instances. Furthermore, given the contrasting intensity profiles of functional and structural images, mutual information is often used as the cost function instead of simpler measures like the sum of squared differences.

Coregistration ensures precise alignment of functional and structural data, facilitating accurate localization of brain activity and supporting robust subsequent analyses, such as normalization and statistical modeling.

2.2.4 Tissue Segmentation

Tissue segmentation [35] [36] is a crucial step in neuroimaging data processing, allowing to classify different brain structures into distinct classes. It typically relies on the use of high-resolution anatomical images to distinguish gray matter (GM), white matter (WM) and cerebrospinal fluid (CSF) as well as non-brain tissues (skull, muscles, fat, skin, etc.) and air. Tissue classes are defined depending on the specific needs of the studies. However, in practice, tissue segmentation presents many challenges, including acquisition noise, partial volume effects (where a single voxel may contain multiple tissue types) and residual magnetic field inhomogeneities.

To overcome these limitations, modern segmentation algorithms exploit complementary information, such as tissue a priori probability maps (e.g., in SPM [17]) and the geometric structure of the gray-white matter interface (e.g., in FreeSurfer [37]). These approaches combine probabilistic models and sophisticated algorithms to improve the accuracy and robustness of segmentations.

2.2.5 Normalization

Spatial normalization [38] [34] is a vital step in neuroimaging that addresses the inherent variability in brain size and shape among individuals. This variability poses challenges for comparing brain function across subjects, as corresponding regions may not align directly. Spatial normalization resolves this by transforming individual brain images into a shared reference frame within a standardized three-dimensional coordinate system, making them directly comparable.

At the heart of spatial normalization is the use of templates-reference images that represent average anatomical features in a defined coordinate space. Early efforts, such as the Talairach atlas [39], laid the foundation by defining a coordinate system anchored to key anatomical landmarks like the anterior and posterior commissures. Modern neuroimaging relies heavily on more advanced templates, such as those developed by the Montreal Neurological Institute (MNI) [40], which are based on the averaging of numerous MRI scans to provide a robust and representative standard [41] [42].

Normalization methods vary depending on the level of detail and focus. Landmark-based normalization uses specific anatomical points to align images piece by piece. Volume-based approaches maximize voxel overlap between individual brains and templates using statistical measures like the normalized correlation

coefficient. Surface-based normalization, in contrast, focuses solely on the cortical surface, aligning features for studies targeting cortical structures.

Quality control is essential in normalization to ensure accuracy. Researchers evaluate the overlap between the normalized images and the template, inspect average images for outliers, or view sequences of normalized brains to identify abnormalities. By ensuring precise alignment across subjects, spatial normalization enables meaningful group comparisons and facilitates insights into brain structure and function.

A notable method in the field of normalization is the Diffeomorphic Anatomical Registration Through Exponentiated Lie Algebra (DARTEL) algorithm [43]. DARTEL is designed to perform deformable (non-linear) image registration, used to align brain images by integrating diffeomorphic deformations. This algorithm is distinguished by its ability to model complex transformations while ensuring that these transformations are inverse-consistent. DARTEL uses a local optimization strategy based on Levenberg-Marquardt and a fast computation method via a constant Eulerian velocity framework.

Segmentation is a critical preprocessing step that typically precedes normalization. In the classical approach implemented in SPM, segmentation and normalization are combined in a framework known as "unified segmentation." This process involves segmenting brain tissues into categories such as gray matter (GM), white matter (WM), and cerebrospinal fluid (CSF), which provides the foundational maps needed for subsequent analysis.

DARTEL builds upon this by requiring segmented tissue maps, particularly GM and WM maps, as input to perform accurate inter-subject alignments. By refining the spatial correspondence of segmented tissues, DARTEL produces high-quality normalizations that reduce variability across subjects. For example, by aligning images to fit into a common space, it helps minimize bias in comparative analyses, whether to differentiate between sexes or to predict parameters such as age from brain morphology.

2.2.6 Smoothing

Image smoothing is a fundamental step in image processing, initially introduced to improve visual quality and facilitate the analysis of digital data. Its principle is based on the application of a filter, most often a Gaussian function, in order to reduce rapid variations in the intensity of pixels or voxels in an image. In practice, this amounts to replacing the value of a given point by a weighted average of its neighbors, where the weight is determined by the distance between the points, with closer voxels contributing more than more distant ones [15]. The primary goals of smoothing are to reduce the high frequency random noise inherent in image capture and reduce the inter-subject anatomical variability, that remains after the normalization step.

Smoothing reduces random signal fluctuations due to noise, thus improving the signal-to-noise ratio (SNR). Then, it compensates for spatial normalization errors by ensuring better superposition of structures between subjects. By combining neighboring signals, smoothing also makes statistical analyses more robust to inter-individual variations and reduces the number of multiple comparisons in statistical tests, thus increasing their power.

Gaussian smoothing, also called Gaussian blurring, is a standard method in neuroimaging to attenuate noise and highlight structures of interest [44]. This technique involves applying a Gaussian filter to an image, which mathematically amounts to convolving the image with a Gaussian function. The Gaussian function, characterized by its symmetrical bell curve, is defined by its standard deviation (σ) which determines the intensity and extent of the smoothing. As a low-pass filter, Gaussian smoothing attenuates high-frequency components of the image, reducing fine details and noise.

However, smoothing is not without tradeoffs. Using an isotropic Gaussian kernel, for example, can lead to a loss of anatomical accuracy, by diluting signals and merging adjacent structures. This poses a particular challenge in the analysis of small brain regions, such as the amygdala or thalamic nuclei, where smoothing can introduce bias by mixing signals from different tissues or structures inducing the partial volume effect.

Partial volume effect (PVE) [45] [46] is an inherent limitation of imaging techniques, particularly MRI, that occurs when the spatial resolution of the scanner is insufficient to clearly differentiate tissues within a voxel. Each voxel may then contain a mixture of signals from different tissue types (e.g., white matter, gray matter, and cerebrospinal fluid). This leads to ambiguity in data interpretation, as the measured signal reflects a weighted average of the properties of the tissues present in the voxel, rather than the precise characteristics of a single tissue type.

In quantitative studies such as quantitative MRI (qMRI) [47] [2] or diffusion tensor imaging (DTI) [48], where measurements depend on precise physical or physiological parameters (such as relaxation constants or diffusion values), partial volume effect can bias results and limit the accuracy of analyses. To mitigate these effects, tissue-specific smoothing methods have been developed. Unlike traditional isotropic smoothing techniques that apply uniform filtering across the entire image, these specific approaches consider tissue boundaries and composition within each voxel. By segmenting the image into different tissue types (e.g., using probability maps of gray matter, white matter, and cerebrospinal fluid), these methods selectively adjust smoothing to preserve details across tissue types while reducing noise within each homogeneous tissue. By combining precise segmentation and adapted smoothing, these approaches reduce the influence of mixed voxels and promote more reliable data interpretation. This work will focus on developing and refining these techniques to enhance the accuracy and reliability of neuroimaging data analysis.

Objective

This master thesis, entitled "Image Smoothing in Neuroimaging: Effect of Gaussian vs. Tissue-Specific Approaches in Statistical Analysis" directly addresses the pressing need for tissue-specific smoothing in advanced MRI applications, including qMRI, DWI/DTI and fMRI. This has also potential for other imaging modalities, such as PET imaging, but that lies outside the scope of this work.

Tissue-specific approaches, such as Tissue-Weighted Smoothing (TWS) [47] and Tissue-Specific smOOthing CompeNsated (TSPOON) [48], aim to preserve anatomical specificity while reducing noise and partial volume effects. These methodologies mitigate potential biases caused by conventional smoothing techniques, offering more accurate insights into tissue microstructure. As such, this work aligns closely with the overarching goal of refining data processing pipelines to maximize the utility of qMRI in neuroscience.

Spatial smoothing is a fundamental step in the statistical analysis of neuroimaging data, aimed at reducing the high frequency random noise and improving the signal-to-noise ratio (SNR). Traditional isotropic Gaussian smoothing [44], while effective, often introduces biases near tissue boundaries due to partial volume effects (PVE), resulting in mixed signals and reduced specificity in tissue analysis.

To address these limitations, tissue-specific smoothing methods have been developed to preserve anatomical and microstructural specificity. For example, the TWS framework combines Gaussian smoothing with tissue probability weighting, while the TSPOON method applies a smoothing-compensation mechanism to correct biases and maintain the integrity of microstructural measurements. These techniques enhance specificity.

By systematically comparing these methods, this master thesis contributes to a deeper understanding of the trade-offs between noise reduction and anatomical specificity, paving the way for more robust and accurate statistical analyses in neuroimaging.

The primary objectives of this work are threefold. First, it involves the implementation of a generalized TSPOON method, designed to extend its applicability beyond white matter (WM) in diffusion tensor imaging (DTI) analysis. This generalized approach ensures that TSPOON can be effectively applied to tissue-specific analyses in qMRI and fMRI data. The second goal of this thesis is to compare the effects of TSPOON versus TWS on already published qMRI results. The objective is to determine whether one approach is superior or more appropriate. The third goal expands the analysis to fMRI data, comparing the effects of three smoothing methods: Gaussian smoothing (GS), TWS and generalized TSPOON. This includes two sub-goals: first, to evaluate the advantages of tissue-specific smoothing (TWS and TSPOON) over GS, and second, to compare TWS and TSPOON directly, as done for qMRI.

Collectively, these analyses aim to refine the understanding of smoothing techniques across multiple imaging modalities, offering practical guidelines for researchers and enhancing the reliability of neuroimaging studies.

Chapter 3

Data & Methods

3.1 Data

In this section, the two datasets used in this master thesis are presented. The data and their processing provided are described. For each dataset, the images of interest for smoothing are also highlighted.

3.1.1 qMRI

The dataset used for quantitative MRI (qMRI) is described and used for the first time in the article by Prof. M. Callaghan [2] describing a study conducted to understand microstructural changes in the human brain related to normal aging. The main objective of the study was to dissociate age-related changes from signs of pathological neurodegeneration, particularly those that are not immediately apparent at the cognitive level. The study aimed to explore age-related differences in brain microstructure, particularly myelination and iron levels, which are parameters sensitive to aging-related changes. The authors sought to establish baseline quantitative benchmarks of these changes in a healthy population, in order to better differentiate normal aging from pathological neurodegeneration.

This dataset consists of data from 138 subjects with an age range spanning from 19 to 75 years, with a mean age of 46.6 years. It is structured according to the brain imaging data structure (BIDS) [49] [50]. This cohort includes 49 male and 89 female participants. Participants were recruited through local advertisements and screened for exclusion criteria such as metallic implants, epilepsy, and neurologic disorders. Cognitive integrity of older adults was ensured using the Mini Mental State Examination (MMSE), with a cutoff score of 28 or higher.

Scanning was conducted on two 3T MRI systems using a multi-parameter mapping (MPM) protocol [25]. For each subject, the acquisitions aim to create high-resolution, quantitative maps of brain tissue properties and include four distinct types of quantitative maps: Proton Density (PD) maps, Magnetization Transfer Saturation (MTsat) maps, Longitudinal Relaxation Rate (R1) maps and Effective Transverse Relaxation Rate (R2*) maps.

The dataset consisted of MPM-derived maps of MTsat, R1, PD and R2*, calculated using regression and signal averaging techniques to enhance signal-to-noise ratio. Data preprocessing included correction for RF transmit field inhomogeneities and adjustments for spatial variations in relaxation times and flip angles to improve map accuracy. These quantitative maps were further normalized to the Montreal Neurological Institute (MNI) [40] space while preserving tissue-specific parameter values and smoothing to reduce residual misregistration artifacts. Brain microstructure analyses involved voxel-based quantification (VBQ) for MR parameters and voxel-based morphometry (VBM) for gray matter volume, employing statistical parametric mapping (SPM8) tools [17]. This preprocessing pipeline ensured quantitative accuracy

and comparability across participants. Measures included signal correction for RF field inhomogeneities and calibration against established values, enhancing reliability.

Statistical analyses examined age-related differences in MR parameters across gray and white matter using linear regression models as general linear model (GLM), controlling for factors like age, gender, total intracranial volume and scanner type. These regressors describe subject-specific demographic and imaging parameters:

- Age: expressed in years.
- Gender: encoded as 1 for male and 0 for female.
- Total Intracranial Volume (TIV): This is the total volume of space inside the skull (measured in liters). It includes GM, WM and cerebrospinal fluid (CSF). The TIV is often used as a covariate in volumetric analyses of the brain to correct for variations in head size between individuals. This allows for more accurate comparisons of the volumes of different brain structures while taking into account overall head size.
- Scanner type: Two types of scanner were used during the acquisitions. They are encoded as 0 for *Quatro* and 1 for *Trio*.

Hypotheses about decreases in MTsat and R1 with age, indicative of demyelination, were tested using one-tailed t-tests, while two-tailed tests were used for PD and R2*. Significance thresholds were adjusted for multiple comparisons, ensuring robust results across all brain analyses. Thus a p-value of 0.05 family-wise error (FWE) corrected level is applied as a threshold on the contrast maps resulting from the GLM.

The objective of this master thesis is to compare the effects of smoothing. To do this, we will use:

- **Warped Quantitative Maps (w-qMaps):** These are the preprocessed and normalized quantitative maps in the MNI space of the four quantitative parameters for gray and white matter. Tissue-specific smoothing approaches (Sections 3.2.2 and 3.2.3) will be applied to these data.
- **Modulated Waped Tissue-Specific Maps:** These are the probability maps of each tissue (GM, WM and CSF) in the MNI normalized space. These maps are also modulated. Voxel values are scaled based on the amount of deformation during spatial normalization, thus preserving the total tissue volume. These modulated maps not only represent the spatial distribution of tissue types, but also preserve volumetric information, making them ideal for subsequent tissue-specific smoothing.
- **Originally Smoothed Maps:** These are the originally preprocessed, MNI-space normalized and smoothed maps from the article.

These data are available on the database linked to the article by Callaghan and al. [2]. The method involves two main steps. First, tissue-specific smoothing is applied to the w-qMaps using both the updated TWS approach and the generalized TSPOON method. Second, a General Linear Model (GLM) analysis is performed on the resulting eighth maps, which represent two tissues and four qMRI parameters (MTsat, PD, R1 and R2*). The overall method can be followed in the Figure 3.1 and the implemented scripts have been written thanks to SPM12 toolbox [17].

GLM Description

A batch script is used to execute the GLM analysis. The input data includes smoothed w-qMaps and originally smoothed maps. The batch uses a factorial design specification module. The specified design is a mutiple regression, incorporating the four relevant covariates: age, sex, TIV and scanner type. The last

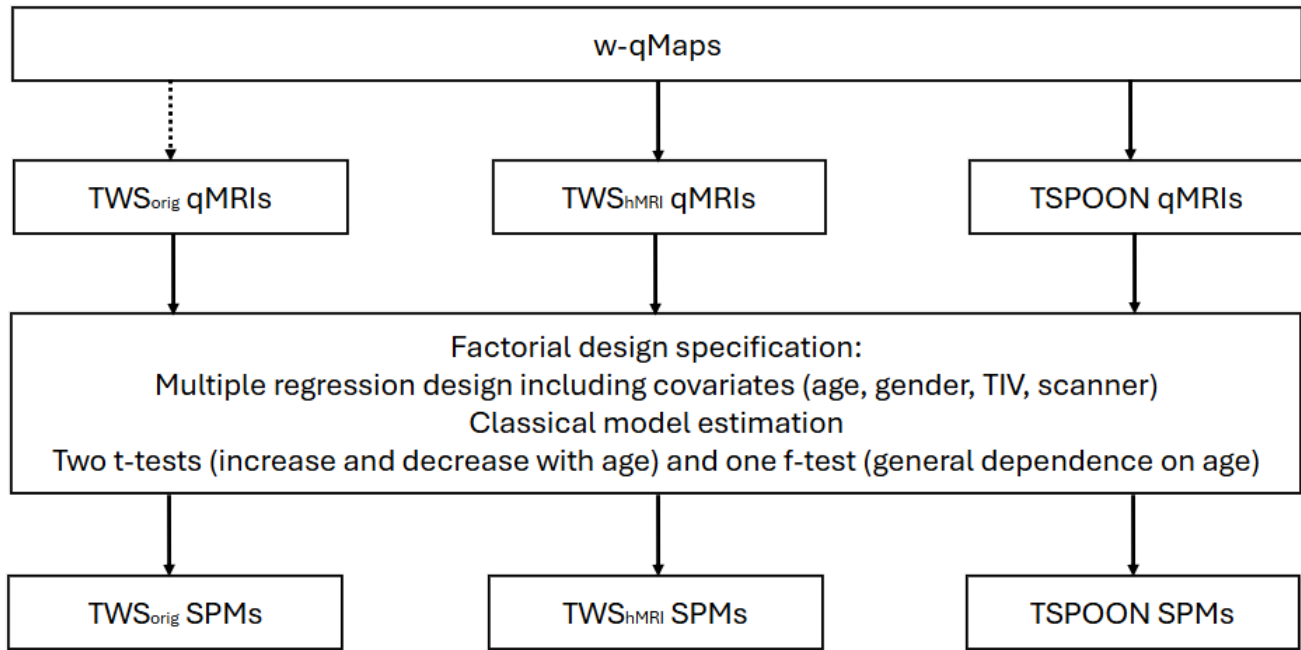


Figure 3.1: Overview of the method followed to reproduce and compare the smoothed results by different approaches of the article by Callaghan and al. [2]. Acronyms: qMRIs for quantitative maps and SPMs for statistical parametric maps. The solid arrows represent all the image processing performed in this thesis, while the dotted arrows represent the image processing that was originally performed when designing the article. Information about smoothing can be found in the appropriate Section 3.2.

three covariates are included in the model to account for their potential confounding effects, while age is the factor of interest. All covariate were mean centered and the model includes a constant term. Finally the intercept is included.

Following the specification of the factorial design [51], the script estimates the GLM parameters (classical model estimation) and sets up contrasts to evaluate specific hypotheses. These contrasts are designed to test for age-related increases and decreases (t-test) in qMRI measures, as well as general dependence (f-test) on age. The contrasts are applied to the estimated model, producing statistical maps that highlight the effects of interest.

Thresholding Methods for Statistical Analysis

In GLM analysis, statistical thresholding is used to identify voxels deemed significant based on a chosen criterion. Two primary approaches are employed, each with distinct purposes and implications for the robustness of the results.

The first approach involves correcting p-values for multiple comparisons to account for the vast number of statistical tests performed across the brain's voxels. This correction can be implemented in various ways, including controlling the Family-Wise Error Rate (FWER) or the False Discovery Rate (FDR). FWER corrections ensure that the probability of any false positives across all tests remains below a specified level (e.g., $p < 0.05$). Methods for FWER correction include parametric approaches like Bonferroni correction and Gaussian Field Theory, as well as non-parametric methods based on permutations. These strategies are highly robust and reduce the likelihood of false positives, making them particularly suited for confirmatory analyses. However, they can be conservative, potentially missing true effects in the data. In the article by Callaghan and al. [2], a $p < 0.05$ FWER corrected level was chosen.

The second approach uses uncorrected p -value thresholds, such as $p < 0.001$. This method applies the significance threshold independently to each voxel, without adjusting for the number of comparisons or correlations among voxels (e.g. due to the image smoothness). While this approach is more sensitive and well-suited for exploratory analyses, it carries a higher risk of false positives, as it does not account for the multiple testing problem. Consequently, results identified through uncorrected thresholds typically require further validation to confirm their robustness but can still be informative.

Effective Smoothing

Effective smoothing, as evaluated in the context of GLM analysis, represents the cumulative smoothness imparted to the data through various processing steps. This includes contributions from MR image reconstruction, motion correction, spatial normalization, explicit smoothing and the residuals of the GLM itself. Effective smoothing is quantified using the Full Width at Half Maximum (FWHM), a measure of the spatial spread of the signal that describes the extent of smoothness in the data.

The FWHM reflects the width of a Gaussian kernel that would produce an equivalent level of smoothness. For instance, if a 6 mm FWHM kernel is applied during preprocessing, the resulting effective FWHM may exceed 6 mm due to additional smoothing introduced by the inherent properties of the data or other preprocessing steps. Furthermore, the FWHM can vary across dimensions, reflecting anisotropic characteristics of the data or uneven smoothing. Calculating the effective FWHM from the residuals of the GLM provides a more accurate estimate of the actual smoothness achieved after all processing stages.

This metric is particularly relevant for our context, where identical preprocessing steps are applied except for the explicit smoothing step which relies on different approaches (Section 3.2).

Creation of Tissue-Specific Mask

Tissue-specific masks are used to delineate the regions where a tissue class (TC) is located. They can be generated from the group-averaged tissue probability maps (GM, WM and CSF) using the following steps [2] [47]:

1. **Initial Smoothing:** The tissue probability maps for each subject are first smoothed using an isotropic Gaussian kernel to reduce high-frequency noise and improve the signal-to-noise ratio. These smoothed maps are then averaged across all subjects to produce group-level tissue probability maps.
2. **Applying the "Majority and Greater than 20%" Criterion:** For the group-averaged probability maps, each voxel is assigned to the tissue type with the highest probability, provided that this probability exceeds 20%. This threshold ensures specificity by excluding low-probability regions that might represent ambiguous tissue classifications. The result is a set of binary masks for each tissue type (GM, WM, and CSF), clearly delineating regions dominated by a single tissue type across the group.
3. **Filtering and Finalization:** The binary masks derived from the group-level tissue probability maps are refined to ensure that they represent high-probability regions specific to each tissue type. These final masks serve as a reference for subsequent analyses.

This approach ensures robust and representative tissue-specific masks based on group-averaged data. These masks improve the accuracy of subsequent analyses by delineating distinct tissue regions and minimizing contamination from low-probability areas or noise.

Creation of Winner-Takes-All (WTA) Mask

Tissue-specific winner-takes-all (WTA) masks play a crucial role in accurately delineating regions dominated by a particular tissue type within the intracranial volume (ICV). This type of mask is used in particular to reconstruct the complete image of the brain from tissue-specific images. These masks provide a clear demarcation of GM, WM and CSF regions by precisely identifying tissue-dominant voxels [2].

To create these masks, segmented and normalized MNI-space tissue probability maps are first aggregated across all subjects (i.e. 138) in the qMRI dataset. Each voxel's intensity is averaged over the population, generating an average tissue probability map for GM, WM, and CSF. Next, the "winner-takes-all" principle is applied: for each voxel, the tissue class with the highest average intensity is selected, assigning that voxel to the corresponding tissue type. This ensures that every voxel is attributed to the tissue class it most likely represents, based on population-level probabilities.

An additional step is performed to ensure anatomical accuracy. An ICV mask, derived from the population data, is applied to the WTA masks. This step eliminates extraneous regions outside the cranial box, such as scalp or background areas, preserving only the voxels located within the brain. The resulting tissue-specific WTA masks provide a refined and population-informed representation of GM, WM, and CSF, which can be directly utilized in subsequent analyses.

3.1.2 fMRI

The *ds000117 v6* dataset on OpenNeuro is a comprehensive dataset built from multi-modal neuroimaging data acquired from 19 healthy volunteers [52] [53]. This dataset includes both functional and structural imaging modalities, enabling extensive analyses of neural activity and connectivity. Functional data comprise electroencephalography (EEG), magnetoencephalography (MEG), and functional magnetic resonance imaging (fMRI) recorded while participants performed a perceptual task involving pictures of familiar, unfamiliar, and scrambled faces across two laboratory visits. Structural data include T1-weighted MPRAGE scans, Multi-Echo FLASH sequences, and diffusion-weighted MR images, providing complementary information on brain anatomy and microstructure. The dataset, despite its small sample size, serves as a valuable resource for developing methods for multi-modal integration, improving spatial and temporal resolution and benchmarking neuroimaging analyses.

The MRI data were collected using a Siemens 3T TIM TRIO scanner. Structural imaging involved a high-resolution 1 mm isotropic T1-weighted MPRAGE sequence. For functional imaging, a gradient-echo EPI sequence was employed to capture blood oxygenation level-dependent (BOLD) signals, with 33 axial slices acquired per volume at 3 mm thickness and a 2-second repetition time. Functional runs consisted of 210 volumes each, with three initial volumes discarded to allow for T1 saturation. Additional Multi-Echo FLASH sequences were acquired at varying echo times and flip angles to enhance contrast and calculate quantitative maps, along with a field map for distortion correction.

In the framework of this master thesis, we are only interested in:

- **Structural Data (T1-weighted MPRAGE):** These data will serve as input for the tissue segmentation step in the preprocessing. This will allow to have tissue-specific maps (GM, WM and CSF) for each subject.
- **Functional Data (fMRI):** These data will serve as input to the GLM after a partial preprocessing (realignment, coregistration, segmentation and normalization).

The structural and functional data sought are present for 16 of the 19 participants. After downloading, the data are extracted and put into the standard BIDS format [49] [54]. The fMRI data underwent a

standard preprocessing by being realigned, coregistered, segmented using unified-segmentation to derive normalization parameters [35] and normalized. The description of the different steps is given in Section 2.2. These normalized data will then serve as input into a general linear model (GLM) [55] which is a first-level statistical analysis.

The GLM includes a session-specific input files (e.g., scans, regressors, and conditions), a high-pass filtering with a cutoff of 128 seconds to remove low-frequency noise and the use of the canonical hemodynamic response function (HRF) with time and dispersion derivatives for modeling neural activity. The batch script also specifies contrasts to test hypotheses, such as four T-tests for specific comparisons like *Faces > Scrambled Faces* and separate tests for *Famous*, *Unfamiliar* and *Scrambled faces*.

Multiple smoothing approaches (Section 3.2) can be applied to the contrasts resulting from the GLM. In this study, smoothing is performed after the GLM for each subject. This choice is justified by the linear nature of the GLM operation, which ensures that smoothing can theoretically be applied either before or after the GLM without altering the statistical outcomes. However, applying smoothing after the GLM simplifies the process by reducing the number of images to be smoothed. The overall method can be followed in the Figure 3.2 and the implemented scripts have been written thanks to SPM12 toolbox [17].

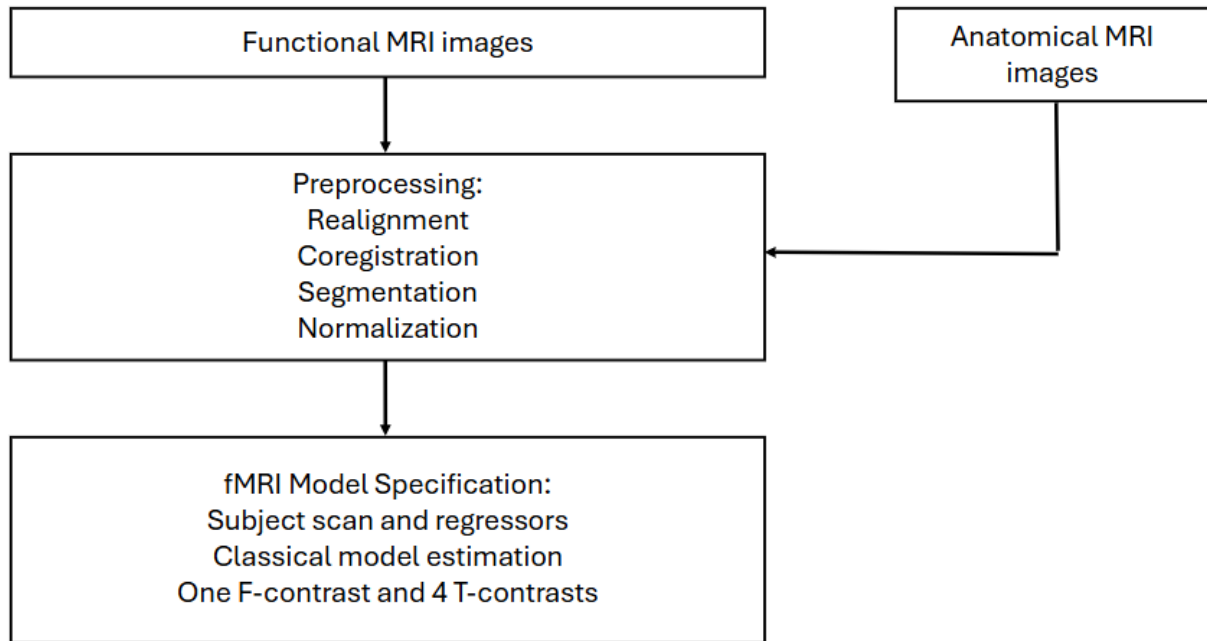


Figure 3.2: Overview of the method to preprocess and prepare fMRI data before smoothing. This workflow is applied for each subjects independently.

3.2 Smoothing Methods

In this section, the three smoothing methods used in this master thesis will be described and explained. The images of interest from the qMRI dataset (Section 3.1.1) are smoothed with the two tissue-specific approaches (Sections 3.2.2 and 3.2.3), while those from the fMRI dataset (Section 3.1.2) are smoothed with all three approaches.

3.2.1 Gaussian Smoothing (GS)

Gaussian Smoothing (GS) [44] is a widely used technique in neuroimaging, achieved by performing a three-dimensional convolution of the input image with a Gaussian kernel of a specified width in each direction. The primary goals of this process are to reduce high-frequency noise and enhance the signal-to-noise ratio, albeit at the expense of spatial resolution. This method operates by averaging voxel intensities based on their spatial proximity, with each voxel weighted according to the Gaussian kernel. The degree of smoothing is governed by the Full Width at Half Maximum (FWHM) parameter, which defines the kernel's width at half of its maximum amplitude. A larger FWHM corresponds to increased smoothing, allowing a greater contribution from neighboring voxels to the intensity of the voxel being processed.

The Gaussian convolution operates by taking each voxel in the input image and replacing its value with a weighted sum of the surrounding voxels. The weights are defined by the Gaussian kernel, which assigns weights decreasing with the distance to the target voxel, following a Gaussian distribution. This kernel is normalized so that the sum of its coefficients equals unity, ensuring that the overall intensity of the image is preserved. The smoothing can be isotropic, where the FWHM is identical along all three spatial dimensions (x, y, z), or anisotropic, with distinct FWHM values for each axis. Mathematically, the Gaussian kernel $G(x, y, z)$ is defined as:

$$G(x, y, z) = \frac{1}{(2\pi)^{3/2}\sigma_x\sigma_y\sigma_z} \exp - \left(\frac{x^2}{2\sigma_x^2} + \frac{y^2}{2\sigma_y^2} + \frac{z^2}{2\sigma_z^2} \right),$$

where $\sigma_x, \sigma_y, \sigma_z$ represent the standard deviations of the Gaussian distribution along the x, y , and z axes, respectively. The relationship between the FWHM and the standard deviation σ is given by:

$$\text{FWHM} = 2\sqrt{2\ln(2)} \cdot \sigma.$$

This formulation ensures flexibility in adapting the smoothing process to various imaging requirements.

GS implementation is included in the Statistical Parametric Mapping (SPM) toolbox [17], but is also available in the Analysis of Functional NeuroImages (AFNI) software toolbox [19] and the FMRIB Software Library (FSL) diffusion toolbox [18], where FMRIB stands for the Oxford Centre for Functional MRI of the Brain. In this master's thesis, the SPM toolbox will be used. A toy comparison is made between the Gaussian smoothing function *spm_smooth*, implemented in the SPM toolbox and *imgaussfilt3*, implemented in the MATLAB Image Processing Toolbox [56] in Appendix A.1.

3.2.2 Tissue-Weighted Smoothing (TWS)

The Tissue-Weighted Smoothing (TWS) method was first introduced in the article by Draganski and al. [47]. It is an advanced approach used to improve the specificity of voxel-based quantification (VBQ) analyses. It aims to minimize the undesirable effects related to the partial volume effect (PVE) (Section 2.2.6), which occurs when voxels contain a mixture of multiple tissue types (e.g., GM and WM). The method corrects for the influence of voxels containing a mixture of tissues, improving the accuracy of measurements at the individual tissue level. TWS allows for more precise differentiation of tissue-specific changes, such as aging-related alterations in GM and WM. This method is compatible with classical workflows of spatial statistical analysis (e.g., SPM) [17]. The TWS approach proposes to smooth any quantitative map (e.g. qMRIs) for a specific tissue class (TC) according to the following mathematical expression:

$$\text{signal}(x) = \frac{g * (w \cdot s(\phi))}{g * w} \quad ; \quad \text{TPM} > 0.05 \quad \& \quad g * w > 0.05 \quad (3.1)$$

where:

- $s(\phi)$ is the quantitative map in standard space warped by ϕ .
- w are the modulated tissue-weights warped in standard space constructed from $w = |\phi|t(\phi)$ where $|\phi|$ are the Jacobian determinants of deformation ϕ and $t(\phi)$ the tissue class image warped by ϕ .
- $g*$ denotes convolution with the Gaussian smoothing kernel.
- $signal(x)$ are the TWS tissue-specific maps.
- $g * w > 0.05$ indicates the division is done under the condition that the denominator is greater than 5%.
- $TPM > 0.05$ indicates the product $w.s(\phi)$ is done under the condition that the TPM is greater than 5%.

The numerator $g * (w \cdot s(\phi))$ in Equation 3.1 is obtained by convolving the TC-weighted MPMs with isotropic Gaussian smoothing. These TC-weighted MPMs are generated by multiplying the modulated tissue weights with the MPMs in standard space warped by ϕ and masking them with a threshold of 0.05 applied to the prior tissue probability maps (TPM) values.

As for the denominator $g * w$ in Equation 3.1, it is derived by convolving the modulated tissue weights with isotropic Gaussian smoothing using the same kernel width as that used for the numerator's convolution.

Finally, the smoothed signal is obtained by dividing the smoothed TC-weighted MPMs by the smoothed modulated tissue weights, specific to the respective tissue class. This division is performed under the condition that the denominator is greater than 0.05, thereby limiting the multiplicative factor to 20.

Different implementations of TWS

This smoothing approach was notably used in the article by Callaghan and al. [2], the same one that presents the qMRI dataset in Section 3.1.1. Age-related differences were analyzed using a VBQ approach. This method allowed for a whole-brain analysis, taking into account tissue-specific effects on quantitative parameters. A key aspect of the analysis is the use of tissue-weighted smoothing, the TWS approach, which was applied to reduce partial volume effects and preserve the specificity of parameter maps across tissue types.

However, the TWS implementation used in the article comes from an older version of the toolbox and is different from the current implementation from the hMRI toolbox [23] [24]. To avoid confusion, the older version of TWS will be referred to as TWS_{orig} while the current one as TWS_{hMRI} , or simply TWS hereafter.

TWS_{orig} applies a tissue-weighted smoothing pipeline. This method uses the tissue segmentation of the unique person to define the final voxel mask for each qMRI parameter (e.g., MTsat, R2*), rather than relying on a consistent tissue probability map (TPM) of SPM for all parameters. As a result, the number of retained voxels (non-zero, non-NaN, non-Infinite) in the smoothed pictures varies according to the individual estimated tissue map. This variability is due to the subject-specific tissue segmentation utilized to construct the voxel mask, which may result in variances between qMRI parameter maps.

TWS_{hMRI} uses a voxel mask based on TPMs for all qMRI parameter maps for the same subject, ensuring that the same set of important voxels is used independent of the parameter being evaluated (e.g., MTsat or R2*). This standardization is based on TPMs (from the SPM toolbox) rather than subject-specific segmentation, which addresses the inconsistencies noted with TWS_{orig} . In view of this standardization and its novelty, it is the TWS_{hMRI} implementation which is described and used in this master thesis.

3.2.3 Tissue-Specific smOothing compeNsated (TSPOON)

The Original Approach

The Tissue-Specific smOothing compeNsated (TSPOON) approach [48] was developed to take care of spatial smoothing in voxel-based analyses (VBA) of diffusion tensor imaging (DTI) data (Section 2.1), particularly in white matter (WM) regions. This method is applied to DTI data, specifically focusing on fractional anisotropy (FA) and mean diffusivity (MD) measures derived from the eigenvalues of the diffusion tensor in the WM regions.

The compensation of smoothing effects was achieved by dividing the smoothed, segmented DTI maps by the corresponding smoothed WM masks. Since both the DTI maps and WM masks underwent the same smoothing, this division effectively counteracted the blurring effect, restoring the values to resemble the original unsmoothed data more closely. TSPOON's effectiveness was tested using root mean squared error (RMSE) to quantify discrepancies between smoothed and original data. It demonstrated reduced smoothing artifacts compared to traditional smoothing methods (SEG and UNSEG). TSPOON was particularly effective at mitigating edge effects near boundaries of WM and other tissues. TSPOON was also applied to WM morphometry analyses. By dividing smoothed WM density maps by the corresponding smoothed WM masks, TSPOON removed edge effects that typically confound traditional VBM methods, improving the accuracy of tissue density assessments.

Apart from the written description, the paper did not include a mathematical formula to explain its novel white matter-specific smoothing approach in DTI. However, one could try to formulate its mathematical expression 3.2 using the descriptions provided such as:

$$signal_{WM}(x) = \frac{g * (M_{WM} \cdot s(\phi))}{g * M_{WM}} \quad (3.2)$$

where:

- $g*$ indicates a convolution with the Gaussian isotropic smoothing kernel.
- M_{WM} = white matter mask (from mFAST algorithm for DTI), normalized in standard space warped by ϕ .
- $s(\phi)$ = normalized multi-parametric map in standard space warped by ϕ .

The Generalized TSPOON Approach

We will now seek to generalize and standardize this smoothing approach so that it can be applied to both white matter and gray matter so that it can be applied to qMRI, fMRI data as well.

Smoothing using the generalized TSPOON method can be mathematically expressed using the following formula:

$$signal_{TC}(x) = \frac{g * (M_{TC} \cdot s(\phi))}{g * M_{TC}} \quad ; \quad g * M_{TC} > 0.05 \quad (3.3)$$

where:

- $s(\phi)$ is the quantitative map in standard space warped by ϕ .
- M_{TC} are the binary tissue-specific masks, normalized in standard space warped by ϕ .
- $g*$ indicates a convolution with the Gaussian isotropic smoothing kernel.
- $signal_{TC}$ are the generalized TSPOON tissue-specific maps.

- $g * M_{TC} > 0.05$ indicates the division is done under the condition that the denominator is greater than 5%.

The main computational steps include the numerator calculation. $g * (M_{TC}.s(\phi))$ in Equation 3.3 is obtained by multiplying tissue-specific masks by a normalized multi-parameter map, followed by Gaussian isotropic smoothing. This process generates tissue-specific signal maps. The denominator is then calculated. $g * M_{TC}$ (Equation 3.3) is created by applying Gaussian isotropic smoothing to tissue-specific masks. This calculation, including the specific steps for forming the mask and applying the 5% threshold, can be found in Figure 3.3. Then comes the final division. Smoothed tissue-specific maps are obtained by dividing the numerators by their respective denominators, provided that $g * M_{TC} > 0.05$ (Equation 3.3). This condition ensures that regions with insufficient masks do not lead to exaggerated intensities in the final signal. A 5% threshold is applied to avoid divisions by values close to zero, thus preserving numerical stability. A discussion on how to handle values close to zero is available in Appendix A.2. This division step compensates for the effects of smoothing and limits the PVE.

An important step in the generalization of TSPOON is the creation of tissue-specific masks. The definition of these masks is crucial. It must be standardized in such a way that it is easily possible to perform it for any tissue class and any MRI type in Section 2.1.

Tissue-Specific Mask

The white matter segmentation of DTI images presented in the original article [48] uses the mFAST algorithm [57] which is present in the FSL toolbox [18] and not in the SPM toolbox [17] and seems to be specific to DTI images. Therefore, the formation of the generalized TSPOON mask cannot rely on this method.

To create the tissue-specific masks M_{TC} , the steps described in Section 3.1.1 can be used by proceeding by subject and no longer by group. This allows the creation of GM and WM masks for TSPOON smoothing.

This choice of mask formation method is well-founded. First, the 20% threshold eliminates low-probability voxels, thus avoiding contributions from other tissues or noise. This ensures that each mask faithfully represents tissue-specific regions, improving specificity. Second, the binary mask-based approach is computationally simple and widely used in the literature. It allows these masks to be easily integrated into subsequent steps of the TSPOON computation, making this approach simple and efficient.

Furthermore, the 20% threshold is a compromise validated by previous works [2] [47], ensuring a good balance between specificity and accuracy. This threshold is therefore compatible with existing standards. Finally, this approach presents a certain numerical robustness. By excluding low-intensity regions, this method reduces the risk of artifacts due to divisions by values close to zero in subsequent steps.

Thus these tissue-specific masks M_{TC} are adaptable to different types of tissues or MPMs from different types of MRIs $s(\phi)$, making them versatile for various analyses. This mask formation thus has widespread applications.

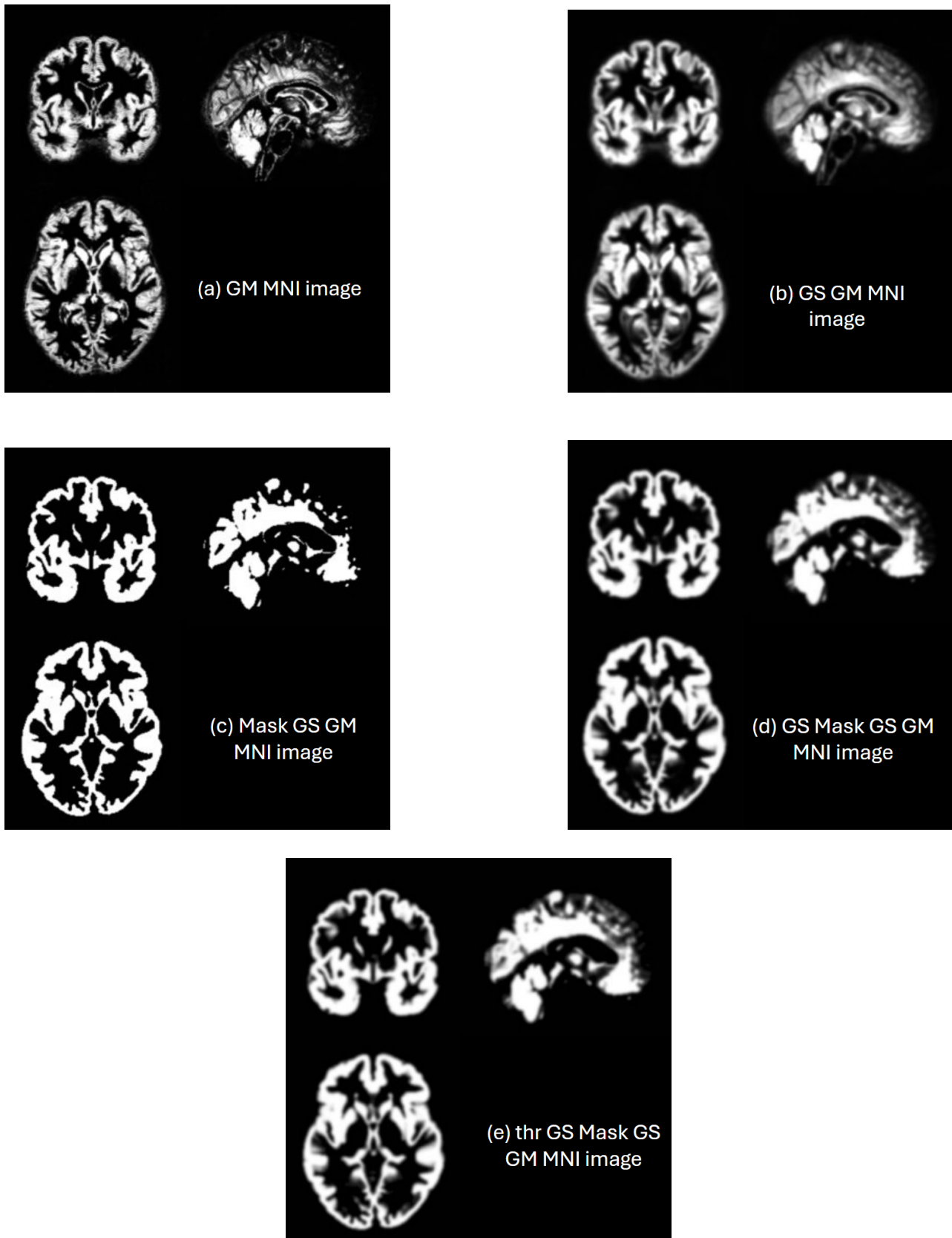


Figure 3.3: Construction of the generalized TSPOON denominator (example with GM maps). (a): probability map (input); (b): gaussian smoothed probability map; (c): "majority and above 20%" binary mask; (d): gaussian smoothed mask; (e) gaussian smoothed mask after thresholding at 0.05.

Comparison of TWS and TSPOON Approaches

Both TWS and TSPOON approaches share the core principle of smoothing the tissue-weighted map and dividing by the smoothed tissue-weight. However, the key difference lies in how tissue-weights are handled. TWS relies on subject-specific tissue probability maps with continuous values between 0 and 1 and a modulation scaling. In contrast, TSPOON employs binarized version of the tissue maps.

3.3 Comparison Strategy on the qMRI Dataset

The same GLM (Section 3.1.1) is run on three sets of images, smoothed in three slightly different ways (i.e. TWS_{orig} , TWS_{hMRI} and generalized TSPOON), leading to similar but slightly different contrasts and statistical maps. The point is thus to compare those results. First, the significant regions after thresholding the statistical maps, e.g. at $p < 0.05$ FWER corrected, can be visually compared with those of the article, then through more quantitatively with some statistical approaches in Section 3.3.1.

Before applying the GLM, the difference induced by smoothing can also be estimated using directly the smoothed quantitative maps (qMRIs). One way to estimate this difference is to calculate the difference between the qMRIs resulting from different smoothings and applies a one-sample T-test to this difference (Section 3.3.2). This approach makes it possible to highlight the brain regions on which the smoothing method induces a significant difference. It is carried out on the entire population and is specific to each qMRI parameter and each tissue class.

Another way to estimate this difference is more intuitive. It considers only a 1D signal extracted from the 3D volume that represents an qMRIs. This approach will make it possible to compare the 1D signals extracted on the same brain profile but resulting from different smoothing methods (Section 3.3.3). However, it is specific to the subject, the profile, the qMRI parameter and the tissue class.

3.3.1 Statistical Approaches

In this section, different statistical approaches will be described in order to analyze and compare the statistical maps, created from the smoothed qMRIs according to the different approaches, resulting from the qMRI dataset in Section 3.1.1.

Bland-Altman Plot

A Bland-Altman plot [58]¹ is a graphical method used to assess the agreement between two different measurement methods or instruments. It is widely applied in clinical and scientific research to evaluate whether two approaches produce similar results and to identify potential biases or systematic differences. The plot visualizes the relationship between the differences of paired measurements and their averages, offering insights into the magnitude of discrepancies and their consistency across the range of measurements.

The primary goal of the Bland-Altman plot is to determine whether two methods can be used interchangeably. Instead of relying solely on correlation coefficients, which measure linear relationships but do not assess agreement, this method evaluates the closeness of measurements in absolute terms. By plotting the differences against the means, the Bland-Altman plot reveals systematic biases, trends and the range of agreement between the methods. This information can be critical for deciding whether a new method can replace or complement an established one.

¹Additional Note: The Bland-Altman method's widespread utility is evidenced by the original paper's high citation count [58]. The paper published by Bland and Altman in The Lancet is among the top 30 most-cited papers of all time (at least in 2014), with over 23,000 citations. This highlights the method's significant impact on the scientific and medical communities.

The Bland-Altman implementation in the context of neuroimages handles two 3D matrices of measurements, flattens them into vectors and removes invalid or irrelevant values (e.g., NaN, Inf, or zeros) to focus on meaningful data points. Then it computes the mean and difference for each pair of measurements. The mean difference (bias), standard deviation, and limits of agreement are derived from these differences. Finally one can plot the Bland-Altman plot $S(x, y)$ following the formula:

$$S(x, y) = \left(\frac{S_1 + S_2}{2}, S_1 - S_2 \right) \quad (3.4)$$

where:

- S_1 is the first value of a pair of matching values, from the first quantitative map.
- S_2 is the second value of a pair of matching values, from the second quantitative map.

Similarity Metrics

Jaccard Index [59], Dice Coefficient [60], and Cohen's Kappa [61] are widely used similarity metrics that evaluate the level of overlap or agreement between two binary datasets, often in the context of binary masks or regions of interest in image processing or neuroimaging. Despite slight differences in their formulations and purposes, these metrics share the fundamental goal of quantifying similarity and agreement between two sets of data, making them ideal for assessing classification performance, segmentation results, or spatial overlaps. Grouping them under the term "similarity metrics" is appropriate because they all provide a numerical measure of how well two datasets match.

The Jaccard Index (JI) [59] measures similarity by comparing the intersection and union of two binary sets (A and B). Mathematically, it is defined as:

$$JI(A, B) = \frac{|A \cap B|}{|A \cup B|} = \frac{|A \cap B|}{|A| + |B| - |A \cap B|} \quad (3.5)$$

Here, $|A \cap B|$ represents the number of elements common to both sets, while $|A \cup B|$ is the total number of unique elements across both sets. A Jaccard Index of 1 indicates perfect similarity, while a value of 0 means no overlap. It is particularly useful in situations where the size of the union is important for evaluating similarity, such as in spatial data or set comparisons.

The Dice Coefficient (DC) [60] is another measure of overlap, closely related to the Jaccard Index but with a focus on the size of the intersection relative to the combined sizes of the two sets (X and Y). Its formula is:

$$DC(X, Y) = \frac{2|X \cap Y|}{|X| + |Y|} \quad (3.6)$$

The Dice Coefficient emphasizes the balance between the two sets and tends to be higher than the Jaccard Index for the same datasets. It is particularly suited for binary mask comparisons.

Cohen's Kappa (κ) [61] evaluates agreement between two sets, accounting for the possibility of random agreement. It is defined as:

$$\kappa = \frac{p_o - p_e}{1 - p_e} \quad (3.7)$$

where:

- p_o is the observed agreement and is computed as the fraction of matching voxels between the two images over the total number of voxels.

- p_e is expected agreement and is computed as:

$$p_e = p_a * p_b + (1 - p_a) * (1 - p_b) \quad (3.8)$$

where p_a is the fraction of significant voxels in the first image and p_b is the fraction of significant voxels in the second image.

Cohen's Kappa ranges from -1 to 1 , where 1 indicates perfect agreement, 0 suggests agreement equivalent to random chance, and negative values indicate systematic disagreement. Unlike Jaccard and Dice, Kappa accounts for random or chance agreement, making it suitable for tasks where random overlap could occur. In our case, the essential difference is that Cohen's Kappa adjusts its result based on the agreement expected by chance. In other words, even if the two evaluators agree most of the time, κ will reduce this apparent agreement if part of that agreement can be explained by chance. An example illustrating this difference, as well as an additional discussion comparing Jaccard and Dice, is presented in Appendix A.3.

The implementation of these three metrics first ensures that the two input matrices have the same dimensions. It converts all non-zero values in the matrices to binary values, creating two masks. Then the intersection $|A \cap B|$ is computed as the number of overlapping non-zero voxels between the two masks, while the union $|A \cup B|$ is the total number of unique non-zero voxels. After that, the size of each binary mask ($|A|$ and $|B|$) and the intersection are used to compute the Dice Coefficient using its formula. This step emphasizes the overlap relative to the individual sizes of the sets. Finally, the total number of voxels (N) is used to calculate the observed agreement (P_o) and the expected agreement by chance (P_e). P_o is the proportion of matching voxels, while $|P_e|$ is derived from the proportions of significant voxels in each mask. Edge cases, such as perfect agreement ($P_e = 1$), are handled by issuing warnings and returning NaN.

As a practical summary, the three metrics can be summarized as follows:

- Jaccard index measures the intersection over the union of significant regions identified by TWS and TSPOON. It ranges from 0 (no overlap) to 1 (perfect overlap). Lower values indicate less similarity in the identified regions between the two methods.
- Dice Coefficient evaluates the overlap of significant regions by comparing twice the intersection to the total size of both regions combined. It also ranges from 0 (no overlap) to 1 (perfect overlap). It is typically higher than the Jaccard index for the same dataset, as it weights the intersection more heavily.
- Cohen's Kappa measures agreement between TWS and TSPOON, accounting for the possibility of agreement occurring by chance. Values range from -1 (complete disagreement) to 1 (perfect agreement), with 0 indicating random agreement.

Threshold Scatter Plot

This section focuses on the thresholds, denoted as T_{thresh} , which represent the critical T-values used to identify significant voxels in statistical maps. These thresholds are defined based on a $p < 0.05$ FWER corrected level, aligning with the methodology described in the article by Callaghan and al. [2] (Section 3.1.1). The T_{thresh} values are not intrinsic voxel intensities but rather statistical thresholds derived from the GLM analysis. They indicate the T-value at which a voxel becomes statistically significant. These thresholds are specific to the smoothing method, contrast and tissue class being analyzed.

The scatter plot in this section visualizes these thresholds for different smoothing methods. Each axis corresponds to the T_{thresh} values calculated for a specific smoothing method. Each point in the scatter plot represents a pair of T_{thresh} values for a given combination of qMRI parameter, tissue class and contrast. The plot enables the identification of patterns such as:

- Agreement: Points close to the diagonal line ($y = x$) indicate consistent thresholds across smoothing methods.
- Systematic Bias: Points consistently above or below the diagonal suggest a systematic difference between methods.
- Discrepancies: Widely scattered points may indicate variability or noise in the threshold determination.

This visualization is particularly valuable for assessing how different smoothing methods influence the statistical thresholds and, by extension, the detection of significant regions.

Cluster Level Comparison

A cluster can be defined in this context as a group containing one or more adjacent voxels that are significant after the application of the $p < 0.05$ FWER corrected level on the statistical maps resulting from the previously described GLM (Section 3.1.1). The number of significant voxels as well as the number of clusters contained in a contrast image are extracted from the SPM results.

Moreover, from the image of the significant results, one can obtain even more information about the clusters. Thus, by binarizing the image of the significant results, the number of voxels contained in each cluster can be counted, which provides new important information about the size of the clusters. Indeed, these cluster sizes can vary depending on the smoothing method used. Next come the calculations of mean, median, standard deviation, and percentiles related to the size of the clusters for each statistical map.

3.3.2 Differences Induced By Smoothing

This section describes how the difference between the smoothed maps can be directly assessed. This relies on a one-sample t-test model and an F-test. Location where significant differences are induced by different smoothing approaches can then be highlighted by thresholding the resulting statistical map with an appropriate threshold.

General Linear Model (GLM) Setup and Testing

The General Linear Model (GLM) used in this analysis includes one constant term (intercept) and four regressors corresponding to covariates: age, sex, total intracranial volume (TIV) and scanner type (Section 3.1.1). The design matrix for the GLM thus takes the following form:

$$X = \begin{bmatrix} 1 & \text{age}_1 & \text{sex}_1 & \text{TIV}_1 & \text{scanner}_1 \\ 1 & \text{age}_2 & \text{sex}_2 & \text{TIV}_2 & \text{scanner}_2 \\ \vdots & \vdots & \vdots & \vdots & \vdots \\ 1 & \text{age}_n & \text{sex}_n & \text{TIV}_n & \text{scanner}_n \end{bmatrix}$$

Here, the first column represents the intercept, capturing the mean effect across all subjects, while the subsequent columns account for variability due to the covariates.

The primary analysis tests whether the parameter associated with the intercept is significantly different from zero using an one-sample t-test. This approach is chosen because there is no prior hypothesis regarding the direction of the effect. By focusing on the intercept, the test evaluates whether the average difference between the TWS and TSPOON methods is statistically significant, independent of the effects of age, sex, TIV and scanner. More information on this analysis is available in Appendix A.4.

F-Test Thresholding

After performing the F-test on the intercept, we will focus on the regions where the difference between the two smoothing methods is significant. After performing the F-test on the intercept, we focus on regions where the difference between the two smoothing methods is significant. However, the choice of the threshold for defining significance depends on the balance we wish to achieve between specificity and sensitivity, as well as the type of inference we aim to draw. Within the context of this master thesis, this concept remains exploratory. Hence, it is appropriate to employ an uncorrected p-value of 0.001 (Section 3.1.1).

3.3.3 Brain 1D Profile

Another way to perceive the differences induced by the different smoothing methods is to consider only a 1D signal from a smoothed qMRIs for a subject and a qMRI parameter. The primary goal of this section is to visualize and compare the smoothed tissue-specific signals extracted from different smoothing approaches. It allows for direct comparison between normalized MNI, TWS_{hMRI} and generalized TSPOON signals.

The results are presented through a series of plots illustrating the differences in intensity profiles and segmentation masks for GM and WM. The interest lies in understanding how different smoothing techniques (TWS and TSPOON) perform in retaining signal fidelity and segmentation precision. Comparing 1D profiles highlights variations in signal intensity attributable to smoothing. It allow us to compare the preservation of anatomical boundaries in segmentation and to compare the smoothed signals against a standard (normalized MNI signal as reference) and population-level masks.

In order to reconstruct the final image of the brain, ICV WTA tissue-specific masks (Section 3.1.1) are applied to the smoothed qMRIs using tissue-specific smoothing methods before adding them together to reform the complete image of the brain, including gray and white matter.

Note: The contribution of the CSF to the reconstruction of the complete image of the brain is not useful in this case. Only the boundary between gray matter and white matter is of interest to us. Moreover, at present, neuroscience studies are largely focused on gray and white matters.

3.4 Comparison Strategy on the fMRI Dataset

First, the dataset processed in this section comes from fMRI (Section 3.1.2). fMRI MPMs aim to show the brain activation areas under certain tasks. Consequently, they have no quantitative power. For this reason, we will proceed with a qualitative analysis of the difference between the results from the different smoothing methods.

To compare the smoothing methods (i.e., GS, TWS and TSPOON), a factorial design is set up for second-level statistical analysis to evaluate the differences among the smoothing methods. In SPM, factorial designs are specifically designed for robust statistical analyses on data from brain imaging studies (such as fMRI or diffusion MRI).

Smoothed contrast images are organized into separate groups for each smoothing method. Explicit tissue-specific masks are applied to exclude irrelevant regions. These masks are generated over all the population. The preprocessed tissue-classified MPMs for GM, WM and CSF are averaged for each tissue class and the population tissue-specific masks are created using the "majority and above 0.2" thresholding criterion, as seen in Section 3.1.1.

The next step estimates the model and defines contrasts to assess the impact of smoothing methods. F-contrasts are configured to compare all spatial differences, as well as pairwise differences between GS, TWS and TSPOON. Additional T-contrasts are specified to identify increases in signal associated with each smoothing method. This method can be seen in Figure 3.4. A statistical threshold of 0.001 is applied to spot regions where the smoothed contrast images show some significant difference. This threshold is chosen to favour sensitivity over specificity, as this is an exploratory study (Section 3.1.1).

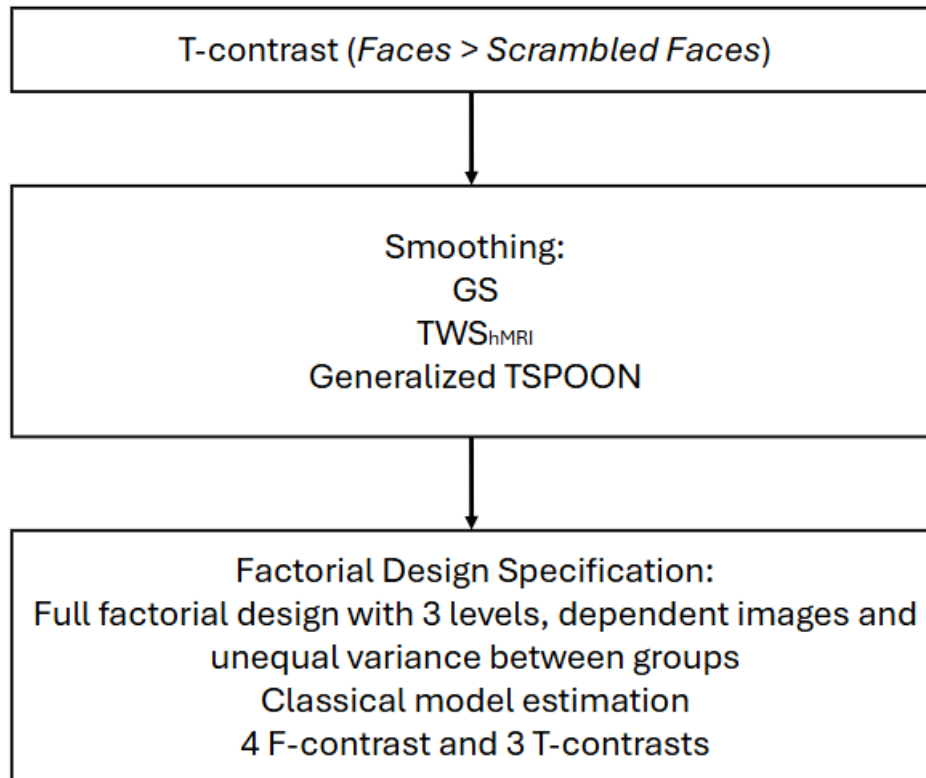


Figure 3.4: Method overview to observe the spatial differences over all the population between the smoothed images on which a different smoothing method is applied.

Chapter 4

Analysis & Results

4.1 qMRI

This section will present the results obtained following the three major analyses carried out (Section 3.3) on the qMRI dataset (Section 3.1.1).

4.1.1 Results Comparison & Statistical Analysis

The statistical maps created (Section 3.3) from different smoothing methods (Section 3.2) will be presented, as described in Methods (Section 3.3). However, not all results are displayed. Only the most relevant ones are presented in this section while the others are located in Appendix B.1.

Displaying Results

Only the areas where a significant increase or difference is detected were displayed without a color scale. Indeed, in the context of statistical parametric maps for qMRI results, such as identifying regions where a qMRI parameter significantly increases with age at the $p < 0.05$ FWE-corrected level, using a single, uniform color rather than a gradient color scale is more appropriate. The purpose of such maps is to highlight regions that are statistically significant. Using a color gradient might inadvertently suggest a varying magnitude of significance, which is misleading, as p-values below the threshold are binary: they either pass the threshold or they don't. A single color uniformly applied to significant regions ensures clarity and avoids misinterpretation.

Furthermore, these results are displayed in two single colors to separate the significant regions coming from gray matter (shown in red) and white matter (shown in blue). This allows for the preservation of important information in the display of the results. Finally, the statistically significant regions were superimposed on the average MT maps of the population in the MNI normalized space to more easily perceive the position of the significant regions.

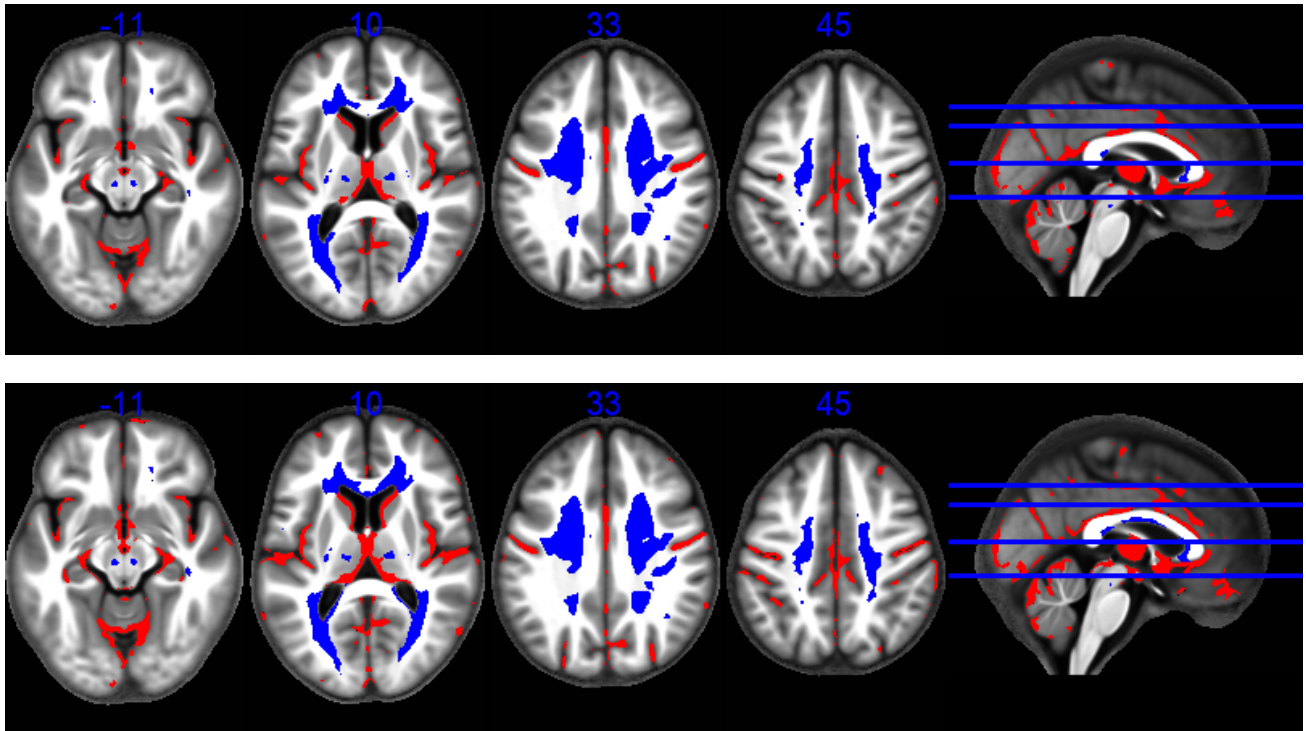


Figure 4.1: Statistical parametric maps identifying regions (red for GM and blue for WM) in which MTsat significantly decreased (AR-) with age at the $p < 0.05$ FWE corrected level. The results are superimposed on the mean MT map for the cohort in MNI space. The four axial slices are located at $z = -11, 10, 33$ and 45 mm, from left to right, as illustrated on the sagittal slice (right). The top row shows results obtained from TSPOON, while the bottom row, the TWS ones.

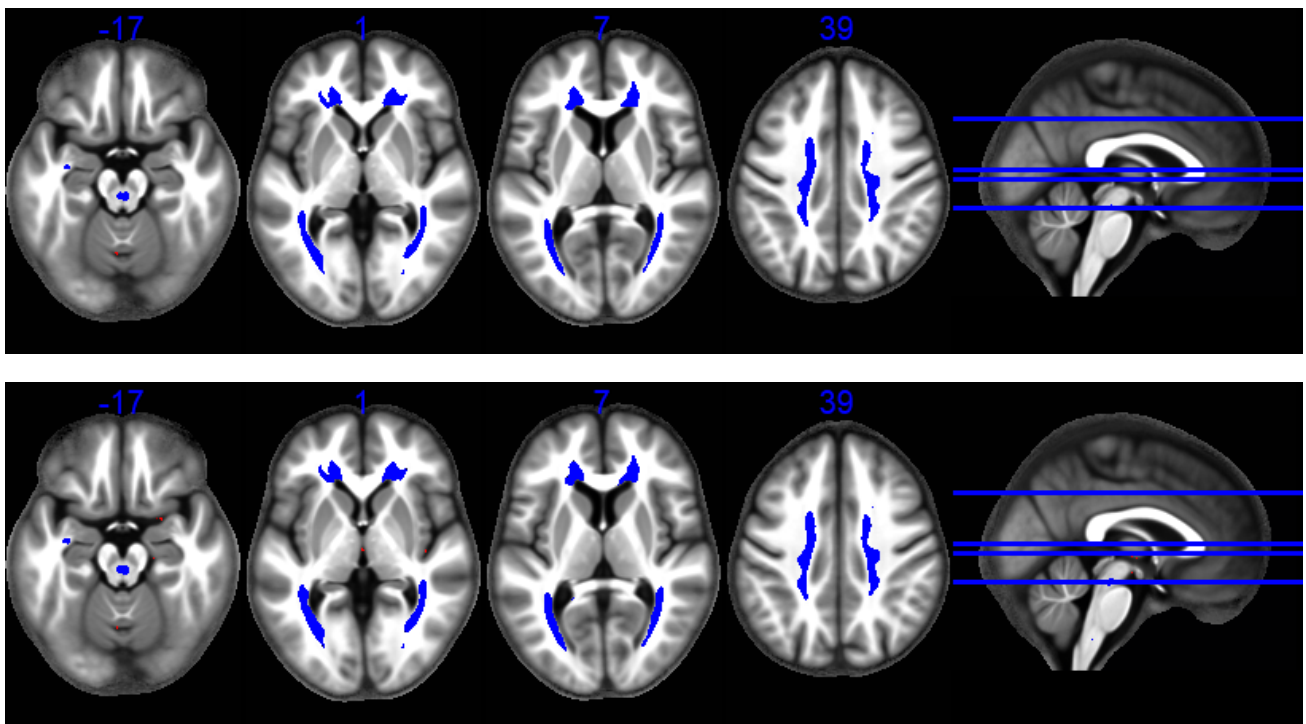


Figure 4.2: Statistical parametric maps identifying regions (red for GM and blue for WM) in which PD significantly increased (AR+) with age at the $p < 0.05$ FWE corrected level. The results are superimposed on the mean MT map for the cohort in MNI space. The four axial slices are located at $z = -17, 1, 7$ and 39 mm, from left to right, as illustrated on the sagittal slice (right). The top row shows results obtained from TSPOON, while the bottom row, the TWS ones.

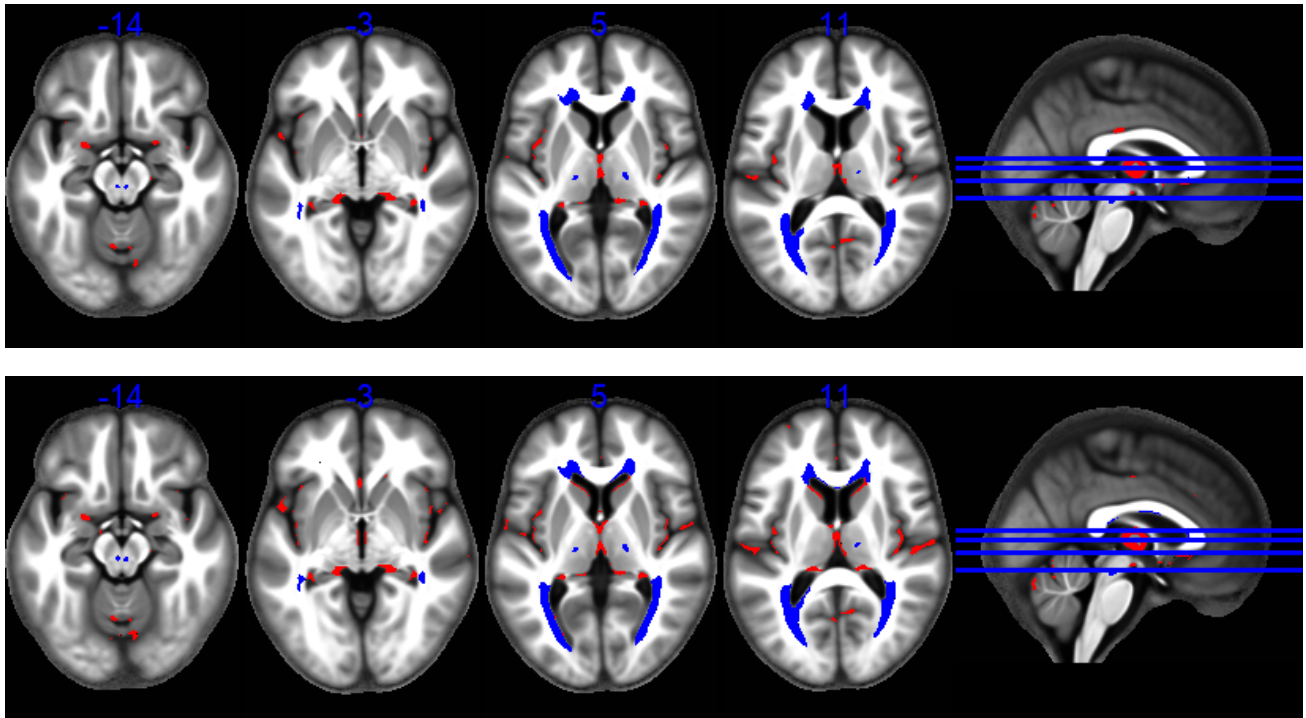


Figure 4.3: Statistical parametric maps identifying regions (red for GM and blue for WM) in which R1 significantly decreased (AR-) with age at the $p < 0.05$ FWE corrected level. The results are superimposed on the mean MT map for the cohort in MNI space. The four axial slices are located at $z = -14, -3, 5$ and 11 mm, from left to right, as illustrated on the sagittal slice (right). The top row shows results obtained from TSPOON, while the bottom row, the TWS ones.

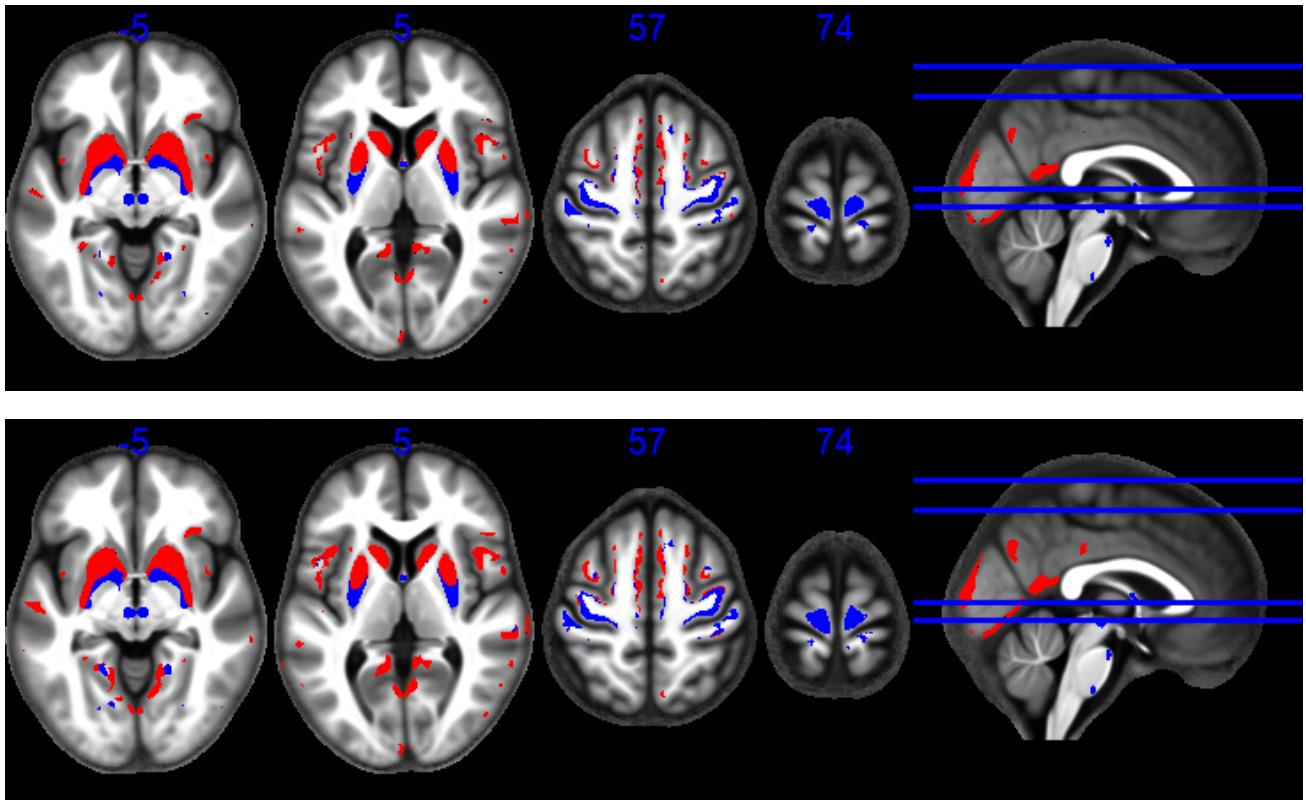


Figure 4.4: Statistical parametric maps identifying regions (red for GM and blue for WM) in which $R2^*$ significantly increased (AR+) with age at the $p < 0.05$ FWE corrected level. The results are superimposed on the mean MT map for the cohort in MNI space. The four axial slices are located at $z = -5, 5, 57$ and 74 mm, from left to right, as illustrated on the sagittal slice (right). The top row shows results obtained from TSPOON, while the bottom row, the TWS ones.

Comparing Results

The regions where **MTsat** decreases significantly with age (Figure 4.1) exhibit considerable similarity between the results obtained using TWS and TSPOON methods. This consistency reinforces the observation that age has a measurable effect on these brain regions as assessed by the qMRI MTsat parameter.

However, subtle differences are evident. In transverse slice at $z = -11$ mm, the significant regions within the white matter are nearly identical between the two methods, whereas disparities are more pronounced in the gray matter. Specifically, TWS reveals a larger number of small significant regions in the anterior part of the brain (towards the top of the axial slices shown in the figure), while TSPOON demonstrates larger significant regions in the central and posterior parts (towards the bottom of the axial slices).

Similar patterns emerge in transverse slice at $z = 10$ mm, where TWS identifies more abundant significant regions in the lateral and central parts of the gray matter compared to TSPOON. Additionally, TWS highlights some small significant regions in the posterior gray matter that are absent in TSPOON. Regarding white matter, significant regions in the anterior part are larger when using TWS, while in the posterior regions, TSPOON exhibits more extensive significant areas, particularly on the left lateral side.

For transverse slices at $z = 33$ mm and $z = 45$ mm, observations in the gray matter align with those described for earlier slices, with TWS highlighting more small significant regions. In contrast with WM, significant regions in the GM appear similarly represented across both methods.

The regions where the **PD** parameter increases significantly with age are shown in Figure 4.2. Notably, neither TWS nor TSPOON reveals significant regions within the gray matter. Although this observation cannot be directly corroborated with prior literature, the significant regions identified by both methods are located in the same areas.

When comparing the results from TWS and TSPOON, their overall similarity is striking, with no region being significant in one method but not the other. However, closer examination reveals subtle differences, particularly in slice at $z = 1$ mm, where the left anterior lateral significant region appears slightly more extensive in TWS compared to TSPOON. Despite these differences, the overall agreement between the methods remains high.

The regions where the **R1** parameter decreases significantly with age are presented in Figure 4.3. In slice 14, the significant regions identified by TWS and TSPOON are highly similar for both gray and white matter.

Transverse slices at $z = -3$ mm, $z = 5$ mm and $z = 11$ mm also display consistent results for white matter across the two methods. For gray matter, the primary significant regions are similarly located; however, TWS consistently identifies a greater number of small significant regions and generally shows larger significant areas compared to TSPOON.

The regions where the **R2*** parameter increases significantly with age are shown in Figure 4.4. For the slice at $z = -5$ mm, significant regions in the white matter are comparable between TWS and TSPOON, though minor differences are observed. In particular, the left posterior lateral significant regions are larger with TWS. Similarly, in the gray matter, TWS highlights larger posterior and lateral significant areas compared to TSPOON, although the main significant regions within the gray matter remain nearly identical between the two methods.

For the slice at $z = 5$ mm, significant regions in the white matter are highly consistent between TWS

and TSPOON, while in the gray matter, TWS identifies larger regions in the lateral and posterior areas. Nonetheless, the primary significant regions in the gray matter remain similar across both methods.

Slices at $z = 57$ mm and $z = 74$ mm represent the upper regions of the brain. In the slice $z = 57$ mm, the significant gray matter regions are slightly larger for TWS, particularly in the anterior part. Conversely, TSPOON shows larger significant regions in the white matter, particularly in the lateral areas. However, on slice at $z = 74$ mm, the significant regions in the white matter are more extensive with TWS compared to TSPOON.

Statistical Analysis

The results of the statistical approaches (Section 3.3.1) are presented in this section. To avoid comparing all the statistical parameter maps (SPM) (Section 3.3), we will statistically analyze those coming from the SPM which have the most biological interest.

qMRI parameter	GM	WM
MTsat	AR-	AR-
PD	AR+	AR+
R1	AR-	AR-
R2*	AR+	AR+

Table 4.1: Age-related effect for qMRI parameters and brain matters. The age-related increase is written AR+ while the age-related decrease AR-.

The Table 4.1 shows age-related effect to use (AR+ or AR-) for each qMRI parameter and tissue class, based on the article by Callaghan and al. [2]. An increase in voxel intensity for R2* and PD is observed, while a decrease is observed for MTsat and R1. Biologically, a decrease in MTsat is explained by the demyelination of axons as well as by certain changes in macromolecules. An increase in PD could be due to an increase in water content, while a decrease in R1 could be explained by a loss of myelin and changes within the different tissues. (GM and WM especially). Finally, an age-related increase in the R2* parameter would be due to an accumulation of iron in the various tissues, more pronounced in gray matter than in white matter.

Effective Smoothing

The results of the effective smoothing, as presented in Figure 4.5, reveal several notable patterns. For the MTsat parameter, TWS demonstrates a stronger smoothing effect in white matter (WM) compared to gray matter (GM), with full-width at half-maximum (FWHM) values reaching approximately 7.8 mm in WM versus 6 mm in GM. In contrast, TSPOON applies a slightly lower degree of smoothing overall, particularly in GM, where the FWHM values are consistently reduced across all dimensions.

Similar trends are observed for the PD parameter. While the smoothing applied to GM and WM is more comparable, TSPOON again applies marginally less smoothing than TWS.

For the R1 parameter, TWS exhibits significantly higher smoothing in WM, with FWHM values exceeding 8.8 mm, while the smoothing effect in GM is more moderate, around 6.5 mm. TSPOON follows the same general pattern but with slightly reduced FWHM values, particularly in GM.

The R2* parameter also demonstrates a pronounced smoothing effect in WM for both TWS and TSPOON. TWS achieves FWHM values of approximately 8.5 mm, whereas TSPOON applies slightly less

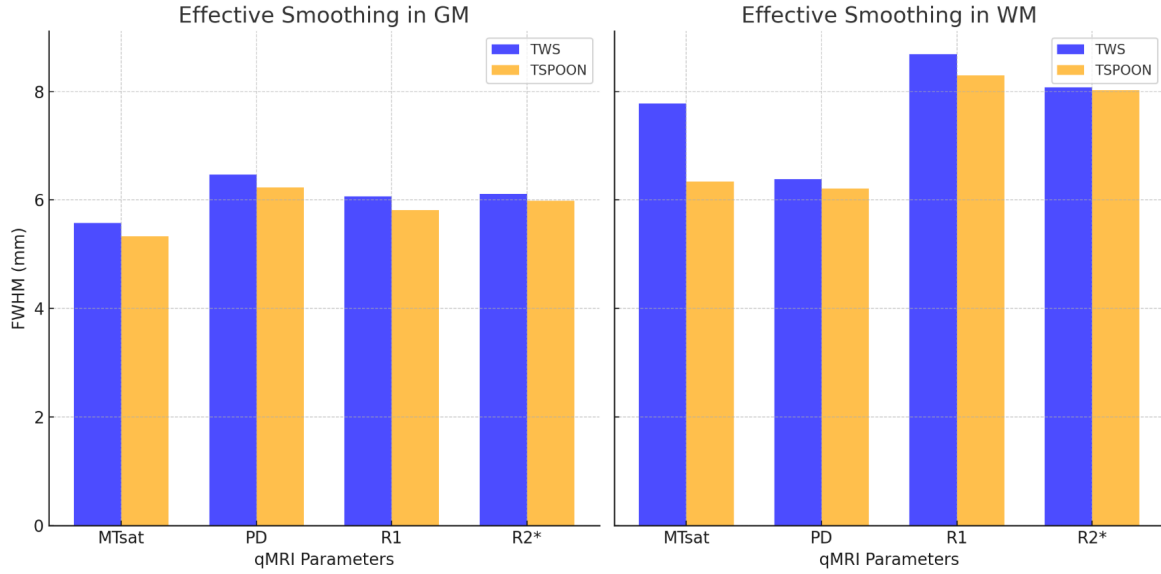


Figure 4.5: Mean FWHM for TWS and TSPOON indicating the effective smoothing applied to the contrast images. These values are the same for all SPMs (AR+, AR- and AR) for each combination of qMRI parameter and tissue class. The mean value was calculated using the (x,y,z) components of FWHM. Full results are displayed in Appendix in Table B.1.

smoothing across all dimensions.

In summary, the analysis highlights consistent differences in the degree of smoothing between GM and WM, with WM consistently experiencing stronger smoothing effects. Across all parameters and tissue classes, TSPOON applies slightly less smoothing than TWS, a distinction that may influence the sensitivity to subtle regional variations, particularly within GM.

Bland-Altman Plot

The Bland-Altman plots presented in this section are derived from AR+ SPM from TWS and TSPOON. The plots created on AR- SPMs are simply the opposite plot of the corresponding AR+ one, as expected as the contrast used simply switches from 1 to -1 .

We will interpret these Bland-Altman plots according to the following criteria:

- Mean Difference (Global Bias):** The mean difference represents the systematic bias between the two methods. It indicates whether one of the methods consistently produces higher or lower values than the other. A mean difference close to zero indicates good overall agreement. A significant mean difference may reflect a bias related to a difference in smoothing algorithms.
- Overall trend of the Average of paired measurements:** The x-axis (average of paired measurements) allows for the visualization of the different averages of corresponding point pairs. This also allows us to see the overall trend of the averages. An average close to 0 indicates a rather weak signal, while a global trend further from 0 indicates a stronger signal.
- Agreement limits ($\pm 1.96SD$):** These limits define the range within which 95% of the differences should fall if the two methods are comparable. Narrow limits indicate a strong concordance between the methods. Wide limits may reflect significant differences in how the two methods handle certain structures or specific intensities. If certain points exceed these limits, it may indicate areas where the two methods diverge significantly (for example, edge or low signal regions).

- **Shape of the point cloud:** The shape and distribution of the points on the Bland-Altman plot provide clues about the differences between the methods. A random and homogeneous distribution around the mean difference indicates good overall agreement without systematic bias or dependence. A clear structure or pattern (for example, a cone or a gradient) can reveal specific differences between smoothing methods:

- Cone effect: The differences increase with the average value, often due to a scaling effect or contrast preservation in high-intensity areas.
- Clustered Points: Groupings in certain intensity ranges can indicate specific behaviors of the methods in these regions.

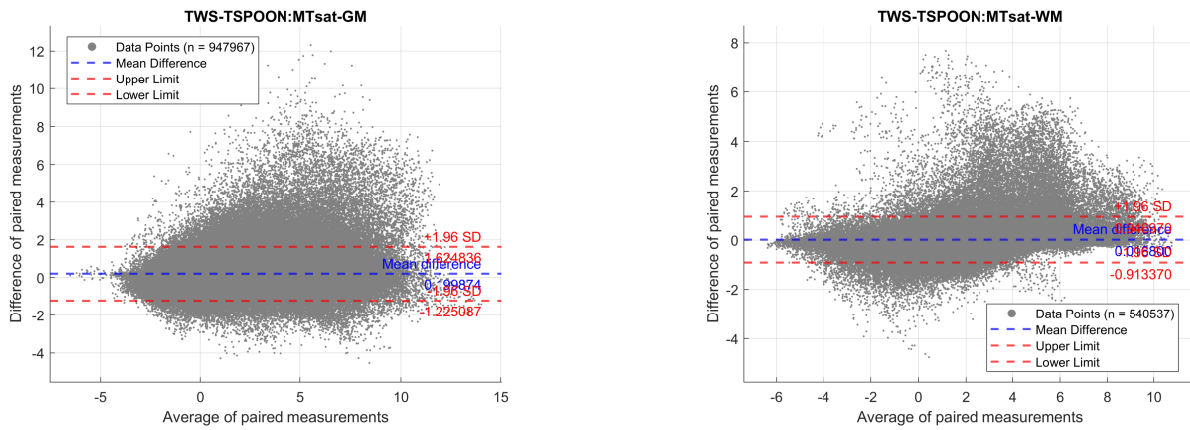


Figure 4.6: Bland-Altman plots (GM on the left and WM on the right) comparing the T-values of the AR- statistical parametric maps for the MTsat parameter obtained using TWS and TSPOON.

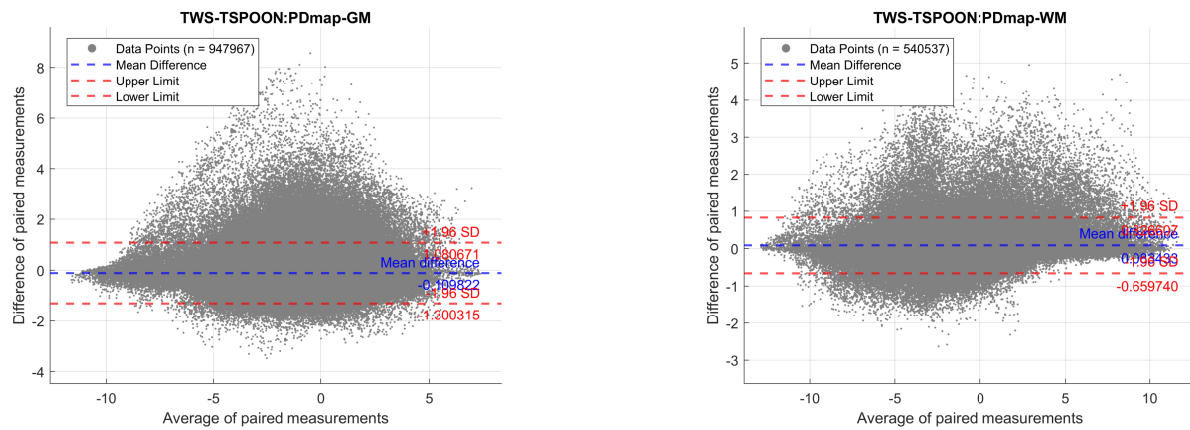


Figure 4.7: Bland-Altman plots (GM on the left and WM on the right) comparing the T-values of the AR+ statistical parametric maps for the PD parameter obtained using TWS and TSPOON.

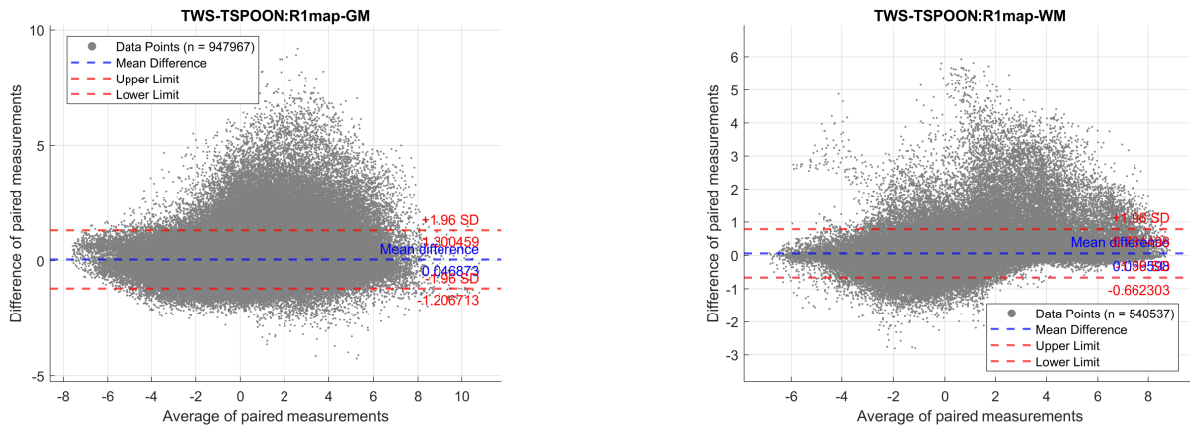


Figure 4.8: Bland-Altman plots (GM on the left and WM on the right) comparing the T-values of the AR- statistical parametric maps for the R1 parameter obtained using TWS and TSPOON.

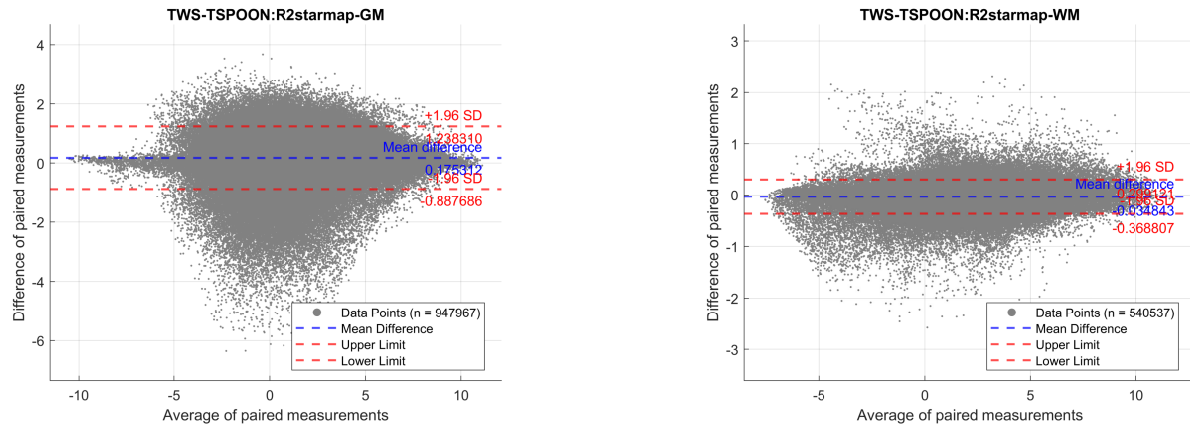


Figure 4.9: Bland-Altman plots (GM on the left and WM on the right) comparing the T-values of the AR+ statistical parametric maps for the R2* parameter obtained using TWS and TSPOON.

For the AR+ SPM related to the **MTsat** parameter (Figure 4.6), a slightly positive mean difference is observed in both gray matter (GM) and white matter (WM), suggesting that the TSPOON SPM tends to exhibit slightly lower T-values than the TWS image. However, the proximity of the mean difference to zero indicates good overall agreement between the two methods. Regarding the overall trend of average T-values, the SPMs generally exhibit medium and positive intensity, particularly in GM.

The limits of agreement are closely aligned with the mean difference, further demonstrating concordance between the methods. Additionally, the point cloud does not reveal any cone or clustering patterns, which suggests no systematic bias. Nevertheless, both GM and WM plots feature extreme points with very small differences, indicating that certain extreme T-values in the TWS SPM are significantly larger than their corresponding T-values in the TSPOON image.

For the **PD** parameter (Figure 4.7), the average differences exhibit opposite signs in GM and WM, indicating good overall agreement between the SPMs of TWS and TSPOON. However, it is noteworthy that TSPOON SPMs show slightly higher T-values than TWS in GM. The average T-values are predominantly negative and remain relatively close to zero, suggesting a generally weak and negative SPM for both methods.

Once again, the limits of agreement are close to the mean difference, reinforcing the strong agreement between the TWS and TSPOON SPMs. The point cloud for both GM and WM do not exhibit any discernible patterns, indicating no clear systematic bias. However, in contrast to the MTsat results, the extreme points show that TWS SPM T-values are much higher than those of TSPOON, in both GM and WM.

For the **R1** parameter (Figure 4.8), the mean differences for both GM and WM are slightly positive and very small, underscoring a strong agreement between the SPMs derived from the TWS and TSPOON smoothing methods. The average T-values appear to be predominantly positive and of low intensity.

The limits of agreement are closely aligned with the mean difference, particularly in WM, further confirming strong overall concordance. The point cloud do not reveal any distinct patterns or dependencies, suggesting the absence of systematic biases. However, it is noteworthy that extreme points tend to exhibit very positive T-values, indicating that certain TWS SPM T-values are significantly higher than those derived from the TSPOON SPMs.

For the **R2*** parameter (Figure 4.9), the mean differences show opposing signs between GM and WM. In WM, the difference is exceptionally small, signifying excellent agreement between the SPMs of TWS and TSPOON. In contrast, the mean difference in GM is relatively high compared to those observed in the other plots, indicating that the overall intensity of the TWS SPM is stronger than that of TSPOON.

The average T-values exhibit a moderate and positive intensity for both methods. The limits of agreement for WM are very close to the mean difference, indicating excellent alignment between the two SPMs. Conversely, in GM, the limits of agreement are noticeably wider, reflecting a less precise alignment, though not to a problematic degree.

The scatter plots for both GM and WM do not exhibit any discernible patterns, suggesting the absence of specific biases or dependencies. However, it is noteworthy that for extreme points, the TSPOON SPM exhibits much higher intensities than the TWS image in GM. In WM, no clear trend is observed for the extreme points.

Similarity Metrics

For the first Table 4.2 dealing with the AR+ SPM, we observe:

- **MTsat-GM:** High agreement with a Jaccard index (JI) of 0.72222 and Dice coefficient (DC) of 0.83871. Cohen's kappa (κ) is also high (i.e. 0.83871), suggesting strong similarity and reliable identification of regions between TWS and TSPOON. **MTsat-WM:** Slightly lower similarity than GM, with a Jaccard index of 0.63249, reflecting moderate overlap. The Dice coefficient (0.77488) and Cohen's kappa (i.e. 0.77486) indicate reasonably strong agreement.
- **PD-GM:** Very low Jaccard index (0.29595) and Dice coefficient (0.45673), along with a low Cohen's kappa (0.45669). This indicates poor agreement in identifying significant regions. **PD-WM:** Exceptionally high similarity (JI = 0.89339, DC = 0.94369, κ = 0.94353), showing excellent agreement between methods.
- **R1-GM and R2*-GM:** Moderate agreement for R1 (JI = 0.6009) and strong agreement for R2* (JI = 0.73129). DC and κ values reflect this trend, with higher agreement for R2*. **R1-WM and R2*-WM:** Strong agreement for both R1 (JI = 0.75472, DC = 0.86022) and R2* (JI = 0.75579, DC = 0.86091), with high κ values supporting these observations.

qMRI Parameter	Tissue Class	Jaccard	Dice	Cohen's Kappa
MTsat	GM	0.72222	0.83871	0.83871
	WM	0.63249	0.77488	0.77486
PDmap	GM	0.29595	0.45673	0.45669
	WM	0.89339	0.94369	0.94353
R1map	GM	0.6009	0.7507	0.75063
	WM	0.75472	0.86022	0.86019
R2*map	GM	0.73129	0.84479	0.84397
	WM	0.75579	0.86091	0.86051

Comparison between the TWS and TSPOON methods for AR+.

qMRI Parameter	Tissue Class	Jaccard	Dice	Cohen's Kappa
MTsat	GM	0.59994	0.74995	0.74786
	WM	0.88199	0.9373	0.93666
PDmap	GM	0.69691	0.82139	0.82073
	WM	0.80304	0.89076	0.89033
R1map	GM	0.40337	0.57486	0.57437
	WM	0.81251	0.89656	0.89633
R2*map	GM	0.63973	0.78029	0.78025
	WM	0.83657	0.91101	0.91097

Comparison between the TWS and TSPOON methods for AR-.

Table 4.2: Jaccard index, Dice coefficient and Cohen's kappa between the significant regions ($p < 0.05$ FWE corrected level) derived from the corresponding statistical parameter maps (AR+ and AR-) of TWS and TSPOON for each combination of a qMRI parameter and a tissue class.

For the second Table 4.2 dealing with the AR- SPM, we observe:

- **MTsat-GM:** Moderate similarity (JI = 0.59994, DC = 0.74995). Cohen's kappa (0.74786) reflects consistent but less robust agreement compared to AR+. **MTsat-WM:** High similarity and agreement (JI = 0.88199, DC = 0.9373, κ = 0.93666), consistent with the trend observed in AR+.
- **PD-GM:** Moderate agreement (JI = 0.69691, DC = 0.82139, κ = 0.82073), suggesting better overlap than AR+. **PD-WM:** Strong agreement (JI = 0.80304, DC = 0.89076, κ = 0.89033), slightly lower than AR+ but still robust.
- **R1-GM** and **R2*-GM:** Poor agreement for R1 (JI = 0.40337, DC = 0.57486, κ = 0.57437). Moderate agreement for R2* (JI = 0.63973, DC = 0.78029, κ = 0.78025). **R1-WM** and **R2*-WM:** Strong agreement for both R1 (JI = 0.81251, DC = 0.89656) and R2* (JI = 0.83657, DC = 0.91101). Cohen's kappa values are high, indicating consistent results across methods.

From a global perspective, we notice a better agreement in WM than GM: Across both AR+ and AR-, significant regions in WM show consistently higher agreement metrics (Jaccard, Dice, and Kappa) than GM, suggesting that the methods yield more similar results in WM. Moreover, in AR+, PDmap-GM shows exceptionally low agreement, while AR- exhibits moderate agreement. This may reflect differences in sensitivity between methods for detecting significant regions in PDmap. We also notice consistency between metrics. Indeed, Dice and Cohen's kappa generally align closely, with Jaccard being slightly lower due to its stricter calculation of overlap.

Note that Jaccard index, Dice coefficient and Cohen's kappa between the significant regions derived from the corresponding SPM (AR) of TWS and TSPOON are in Appendix B.3.

Threshold Scatter Plot

Thresholds at which the intensity of a voxel in a statistical parameter map (SPM) is sufficient to be considered significant will be highlighted. Significance is estimated by applying a threshold at $p < 0.05$ FWER corrected level (Section 3.3.1).

qMRI Parameter	GM	WM
MTsat	5.3558	4.9896
PD	5.2595	5.1249
R1	5.3027	4.9143
R2*	5.2972	4.9649

TWS

qMRI Parameter	GM	WM
MTsat	5.3797	5.0147
PD	5.2747	5.1309
R1	5.3216	4.9305
R2*	5.3019	4.9548

TSPOON

Table 4.3: T-value threshold at $p < 0.05$ FWE corrected level for TWS and TSPOON for AR+ and AR- SPM. These values are the same both for AR+ and AR- SPM.

Based on the intensity values from which a voxel is considered significant (T-values threshold) according to a combination of the considered qMRI parameters and tissue, a scatter plot can be constructed where each point will be a combination while the axes will be the T-values threshold according to one or the other smoothing method. In statistical terms, the interpretation of points in a scatter plot depends on their distribution relative to the line $x = y$:

- **All points on the line $x = y$:** If all points lie exactly on the diagonal $x = y$, it indicates that the thresholds from the two smoothing methods (TWS and TSPOON) are identical for all combinations of qMRI parameters and tissue classes. Statistically, this suggests perfect agreement between the two methods, meaning they yield equivalent results under all conditions tested.
- **All points above the line $x = y$:** If all points are above the line $x = y$, this means that the thresholds determined by TSPOON are consistently higher than those determined by TWS. Statistically, this indicates that TSPOON requires stricter conditions (higher thresholds) for a voxel to be considered significant compared to TWS. This could reflect a systematic difference in the sensitivity of the two methods, with TSPOON being less permissive in identifying significant voxels.
- **All points below the line $x = y$:** Conversely, if all points are below the line $x = y$, the thresholds from TSPOON are systematically lower than those from TWS. This suggests that TSPOON is more permissive and considers voxels significant under less strict conditions compared to TWS.

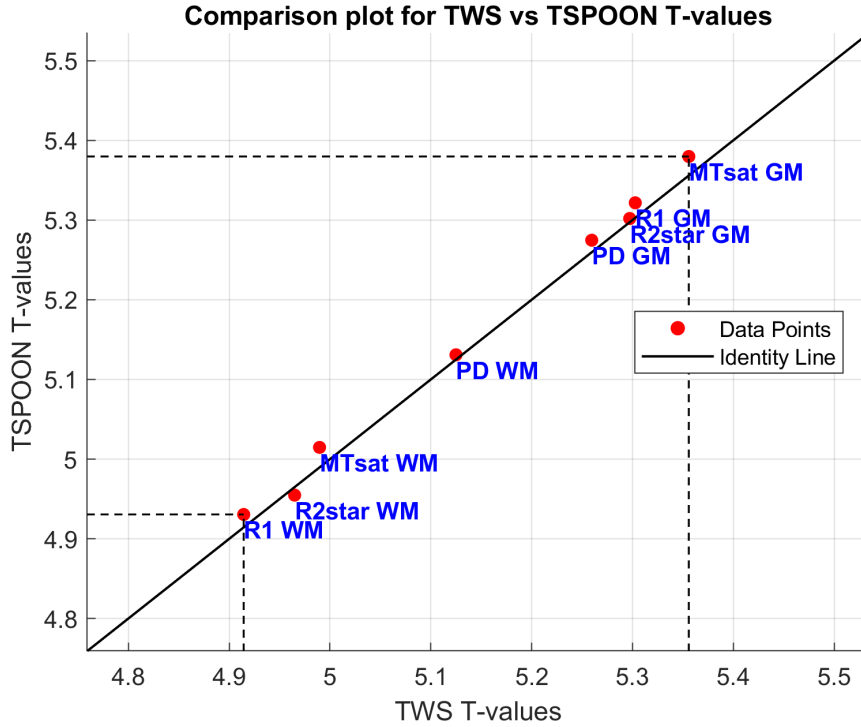


Figure 4.10: Scatter plot of AR+ representing the different possible combinations of qMRI parameters and tissue class. The coordinates of these points represent the threshold above which a voxel will be considered significant depending on the smoothing method (TWS and TSPOON here). In the order of position starting from the origin of the graph: R1-WM, R2*-WM MTsat-WM, PD-WM, PD-GM, R2*-GM, R1-GM, MTsat-GM and the order is the same for AR+, AR- and AR.

We can observe in Figure 4.10 that all points except one are above the line $x = y$, it indicates that TSPOON generally leads to slightly higher thresholds than TWS for most combinations of qMRI parameters and tissue classes, but there is a specific case where this pattern is not followed. The only divergent point corresponds to the R2* map in the white matter. Statistically, this single deviation might point to a unique sensitivity of TWS for that specific parameter/class combination or a specific characteristic of the parameter/tissue class combination that interacts differently with the methods.

The graph observed in the case of the AR- SPM is exactly the same as for AR+, which makes sense since the thresholds are identical between these two SPMs (Table 4.3). For the AR SPM, the scatter plot has a similar appearance, presenting the same results with simply different threshold values. These AR- and AR scatter plots are in Appendix B.4.

Cluster Level Comparison

This section presents information on the clusters that include voxels, significant at $p < 0.05$ FWE corrected level. Overall, these clusters exhibit extremely variable sizes, from a single voxel to 6580 voxels. As one might expect, the distribution of cluster sizes is not normal nor uniform but is rather similar to a decreasing exponential distribution in Figure 4.11). For these reasons, we only consider the numbers of significant voxels, distinct clusters and the median sizes of the different clusters to be useful information. These values are presented in Table 4.4.

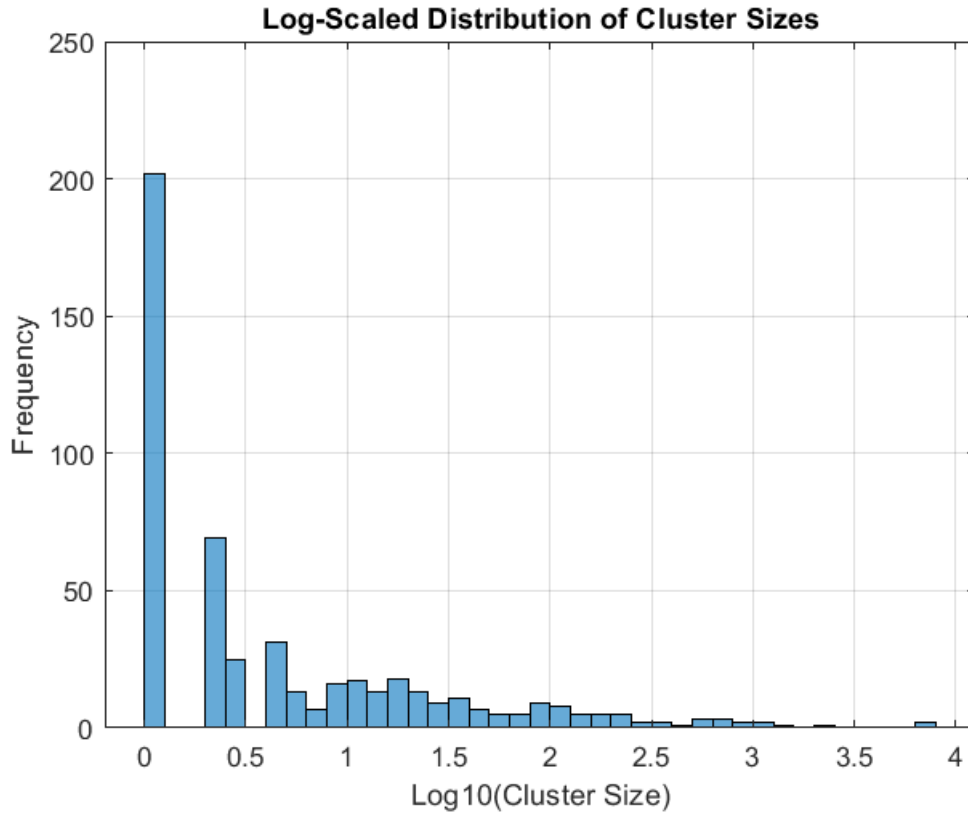


Figure 4.11: Logarithmic distribution in base 10 followed by the sizes of distinct clusters in the case of an increase in $R2^*$ parameter in GM from the AR+ statistical parameter map smoothed with TSPOON.

Overall, one can notice that the number of significant voxels is higher for TWS than for TSPOON for both considered SPMs (AR+ and AR-), with the exception of three combinations of qMRI parameters and tissue class (i.e., MTsat-GM, R1-WM, $R2^*$ -GM). These three combinations have no qMRI parameter or tissue class in common.

For the AR+ SPM, it is observed that the number of clusters detected using images from TSPOON is always lower than that corresponding to TWS. It is almost the same for the AR- SPM, where only the PD-WM and $R2^*$ -WM combinations have a higher number of clusters from TSPOON than from TWS. We notice that these two combinations have in common that they are white matter.

On the other hand, the median cluster sizes from TSPOON are always greater than or equal to those from TWS for the AR- SPM. It is more difficult to observe a trend on the AR+ SPM side where the median cluster size does not seem to be correlated with a smoothing method, qMRI parameter, or tissue class.

qMRI Parameter	Tissue Class	# Significant Voxels	# Clusters	Median Cluster Size
MTsat	GM	14	1	14
	WM	553	11	32
PD	GM	812	83	2
	WM	21481	33	5
R1	GM	2150	37	4
	WM	1096	17	9
R2*	GM	41221	659	2
	WM	21308	311	1

TWS AR+ SPM

qMRI Parameter	Tissue Class	# Significant Voxels	# Clusters	Median Cluster Size
MTsat	GM	17	1	17
	WM	482	14	17.5
PD	GM	436	27	3
	WM	19456	31	4
R1	GM	2110	26	3.5
	WM	1136	16	22.5
R2*	GM	34116	512	2
	WM	19386	285	2

TSPOON AR+ SPM

qMRI Parameter	Tissue Class	# Significant Voxels	# Clusters	Median Cluster Size
MTsat	GM	69552	1160	1
	WM	75590	164	1
PD	GM	27692	485	2
	WM	28255	109	2
R1	GM	11435	547	1
	WM	16926	95	1
R2*	GM	1347	50	2
	WM	3442	10	120.5

TWS AR- SPM

qMRI Parameter	Tissue Class	# Significant Voxels	# Clusters	Median Cluster Size
MTsat	GM	51000	540	2
	WM	67863	63	9
PD	GM	24320	331	2
	WM	27962	125	2
R1	GM	6385	188	3
	WM	14048	30	6.5
R2*	GM	1352	19	5
	WM	3177	13	49

TSPOON AR- SPM

Table 4.4: Tables showing the number of significant voxels ($p < 0.05$ FWE corrected level), the number of clusters they form, as well as the median size of these clusters for each combination of qMRI parameter and tissue class. Each table is related to a smoothing method (TWS or TSPOON) and a statistical parametric map (AR+ or AR-).

4.1.2 Differences Induced By Smoothing

The results from the F-test performed on the intercept of the one-sample t-test model, as explained in Section 3.3.2, are presented in this section.

The statistical threshold was set at $p < 0.001$ uncorrected for multiple comparison. The point here is to detect any potential difference between the maps smoothed by TWS vs TSPOON, i.e. focus on sensitivity instead of specificity.

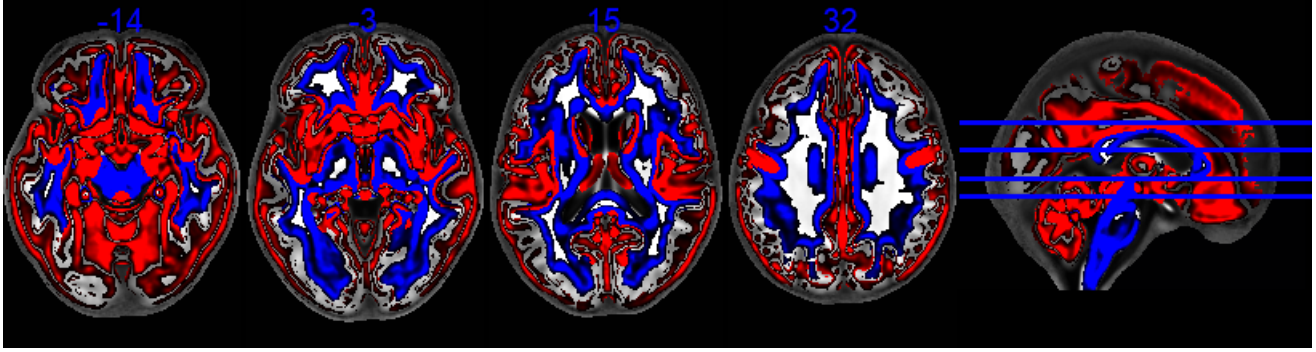


Figure 4.12: Statistical parametric maps in MNI space showing regions where MTsat maps are significantly affected by the difference between TWS and TSPOON, at the $p < 0.001$ uncorrected level. Regions in red correspond to GM, and regions in blue correspond to WM. Axial sections are displayed in a multislice format at $z = -14, -3, 15$ and 32 mm, from left to right, as illustrated on the sagittal slice (right).

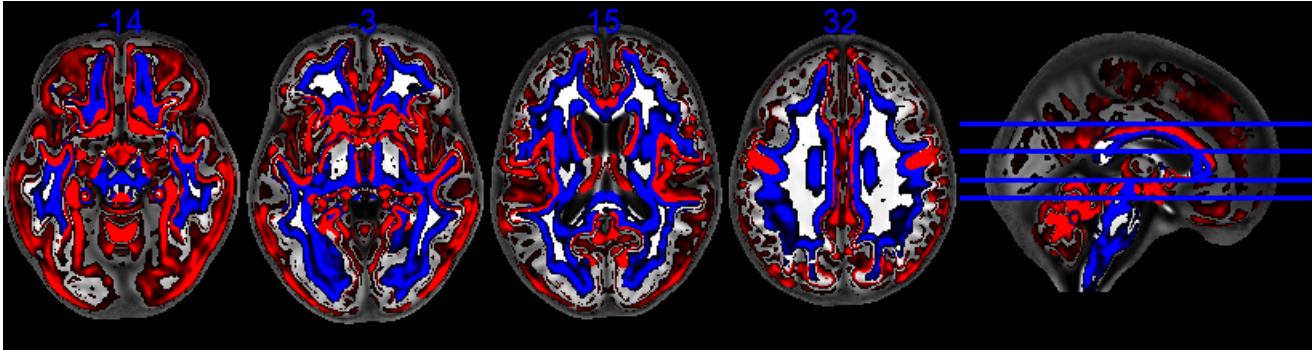


Figure 4.13: Statistical parametric maps in MNI space showing regions where PD maps are significantly affected by the difference between TWS and TSPOON, at the $p < 0.001$ uncorrected level. Regions in red correspond to GM, and regions in blue correspond to WM. Axial sections are displayed in a multislice format at $z = -14, -3, 15$ and 32 mm, from left to right, as illustrated on the sagittal slice (right).

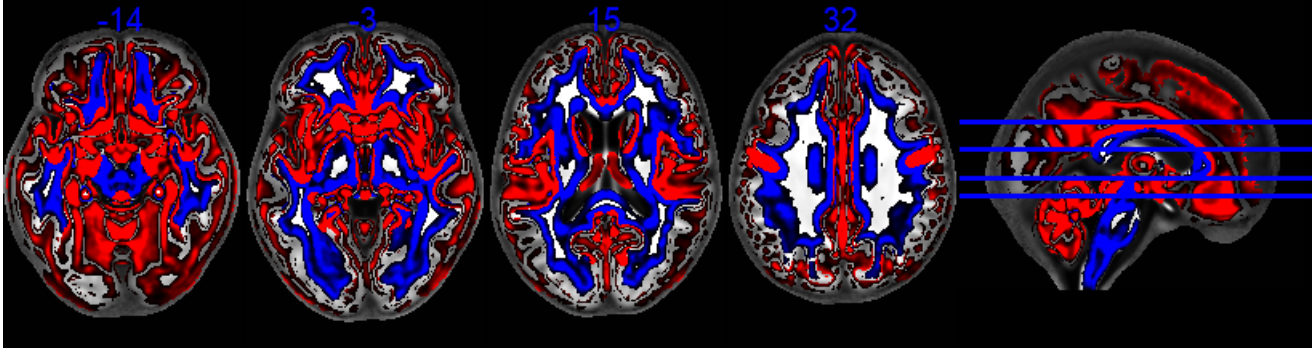


Figure 4.14: Statistical parametric maps in MNI space showing regions where R1 maps are significantly affected by the difference between TWS and TSPOON, at the $p < 0.001$ uncorrected level. Regions in red correspond to GM, and regions in blue correspond to WM. Axial sections are displayed in a multislice format at $z = -14, -3, 15$ and 32 mm, from left to right, as illustrated on the sagittal slice (right).

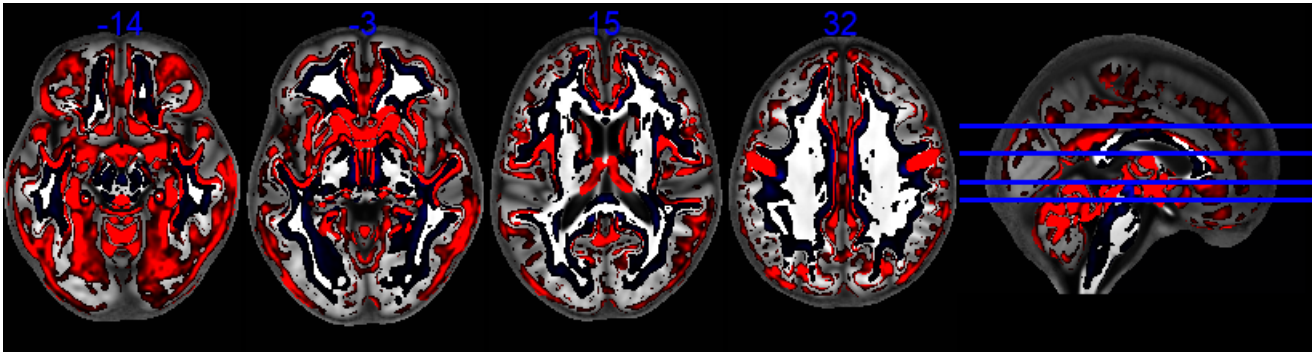


Figure 4.15: Statistical parametric maps in MNI space showing regions where R2* maps are significantly affected by the difference between TWS and TSPOON, at the $p < 0.001$ uncorrected level. Regions in red correspond to GM, and regions in blue correspond to WM. Axial sections are displayed in a multislice format at $z = -14, -3, 15$ and 32 mm, from left to right, as illustrated on the sagittal slice (right).

The results presented in Figure 4.12 show that the difference between TWS and TSPOON has a global impact on the MTsat parameter. The term "impact" is used here to encompass both increases and decreases in parameter values, as these results stem from an F-test, capturing the entirety of the variation attributable to the difference between TWS and TSPOON. Across the various slices, it is evident that the disparity between the two smoothing methods significantly affects nearly all brain regions, with the exception of certain non-frontal areas located deep within the white matter, as exemplified by slice at $z = 32$ mm.

For the PD parameter (shown in Figure 4.13), the difference between TWS and TSPOON also exerts a considerable influence. However, the significant regions observed are notably finer compared to those seen in MTsat (4.12). These refined regions are particularly evident in both gray matter and at the boundaries between tissue classes, as shown in slices at $z = -14$ and 15 mm.

Similarly, the R1 parameter (shown in Figure 4.14) is significantly affected by the difference between the two smoothing methods. The spatial distribution of its significant regions closely resembles that observed for the qMRI MTsat parameter.

Finally, the analysis of the R2* parameter (shown in Figure 4.15) reveals trends akin to those seen in the PD parameter. Significant regions in the gray matter are more localized and concentrated near the

borders between tissue classes. However, in the white matter, significant regions are much less discernible, though they are present.

4.1.3 Brain 1D Profile

In this section, a 1D profile within the brain is selected for analysis as explained in Section 3.3.3. Along this profile, the smoothed warped into warped signals in MNI space obtained using TWS and TSPOON will be compared within the white matter (WM) and gray matter (GM). Before delving into the signal analysis, the rationale behind the selection of the 1D profile and the representative brain subject is outlined.

Profile Selection

To begin, the warped signal in MNI space of any given brain exhibits inter-subject variability due to anatomical differences between individuals. However, these variations are limited, as the composition of tissue classes (e.g., GM, WM) remains consistent relative to specific positions in the brain, with only minor inter-subject differences. Given that this subject-specific variability is negligible in the context of this analysis, the first subject was chosen for practical convenience.

Regarding the selection of the 1D profile coordinates, the focus is on capturing the behavior of smoothed signals at the boundaries between tissue classes (i.e., GM and WM) and their overall characteristics. To achieve this, the selected 1D profile minimizes the presence of cerebrospinal fluid (CSF) to maximize the relevance of the observations. Additionally, the anteroposterior axis is preferred, as it corresponds to the brain's longest dimension, offering a more comprehensive view of the signal transitions. The selected 1D profile is illustrated in Figure 4.16.

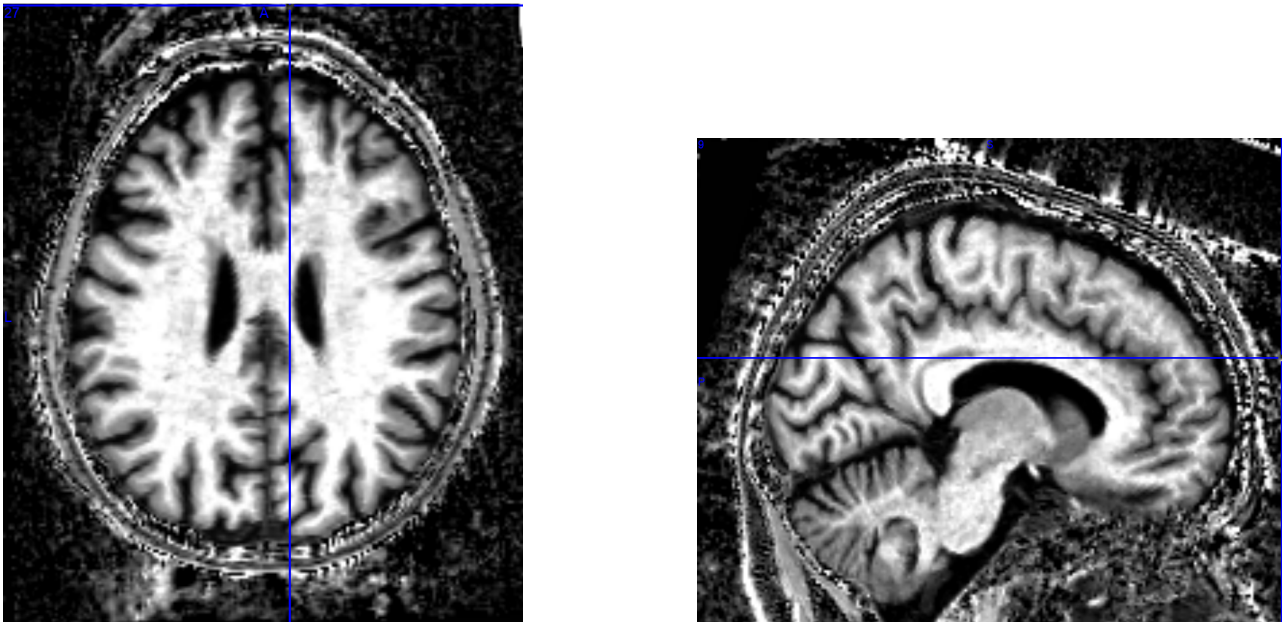


Figure 4.16: 1D profile selected in the warped MTsat map in MNI space of the first subject according to axial and sagittal cuts.

Tissue-Specific Signals

In Figures 4.17, 4.18, 4.19 and 4.20, five distinct graphs are presented for analysis. The central graph C illustrates the binary signals derived from the masks of the two tissue classes under consideration (i.e., gray matter (GM) and white matter (WM)). These binary signals reflect the purpose of a tissue mask, which

is to indicate whether a given voxel belongs to a specific tissue type. The masks displayed correspond to the WTA masks generated as described in Section 3.3.3, which are subsequently utilized to reconstruct a single map from the tissue-specific maps.

The graphs B and D represent the denominators used in the TWS and TSPOON smoothing processes (labeled as TWS sGM/WM and TSPOON sMask GM/WM, respectively) as well as the density of the corresponding tissue class (i.e., GM or WM density). These denominators are defined in the smoothing functions outlined in Section 3.2.3, while the density represents the segmented tissue class probability maps utilized for mask formation.

Lastly, the graphs A and E display the signals warped into MNI space derived from the normalized MNI maps, alongside the corresponding signals from the TWS and TSPOON smoothed maps.

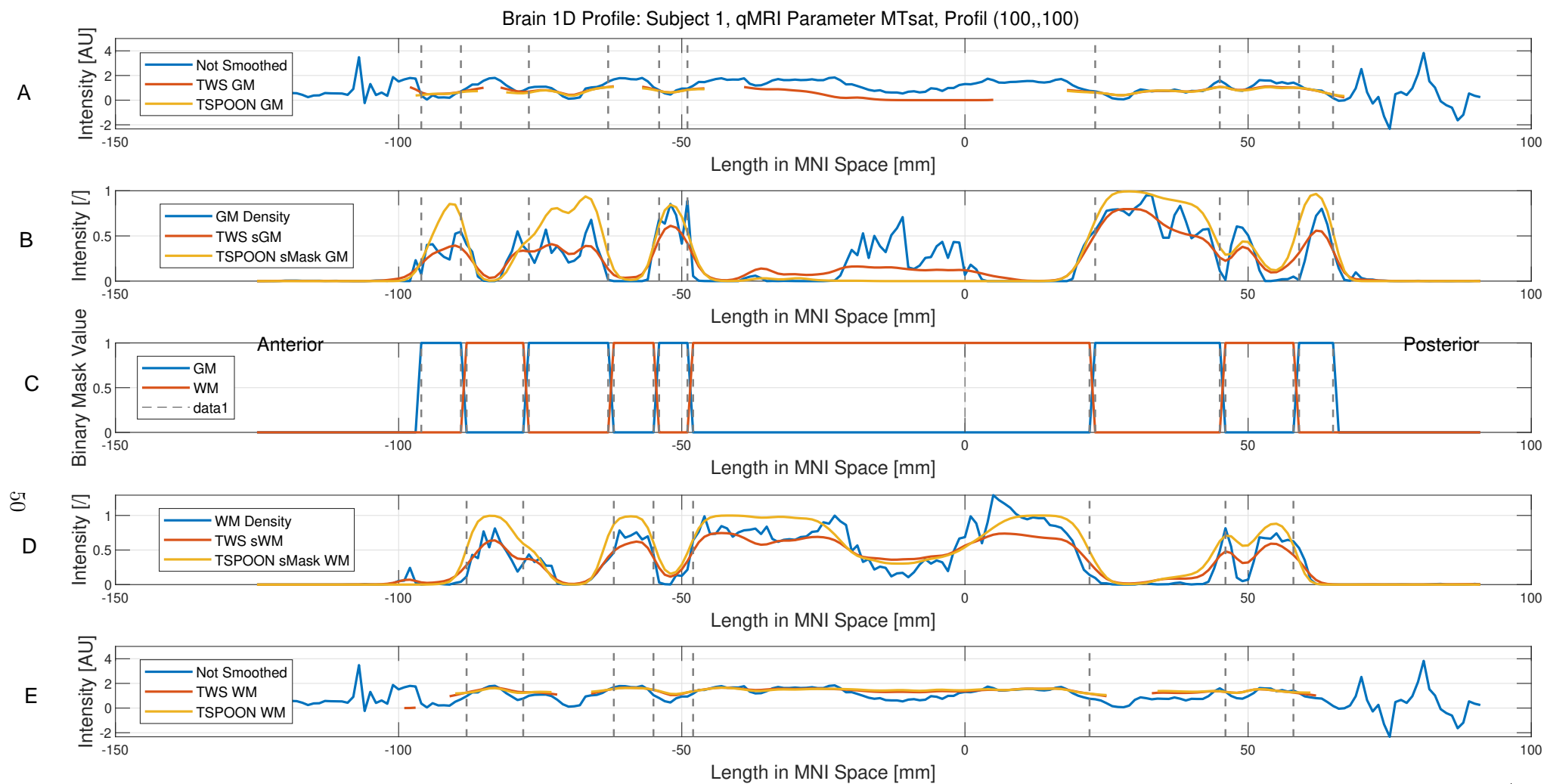


Figure 4.17: Brain 1D profile warped into MNI space for MTsat parameter, subject 1. Graph A show WTA masks. Graphs B and D show the TWS and TSPOON denominator signals and the tissue density signal. Graphs A and E show the TWS and TSPOON smoothed signals and the original one. The results are showed in both GM and WM.

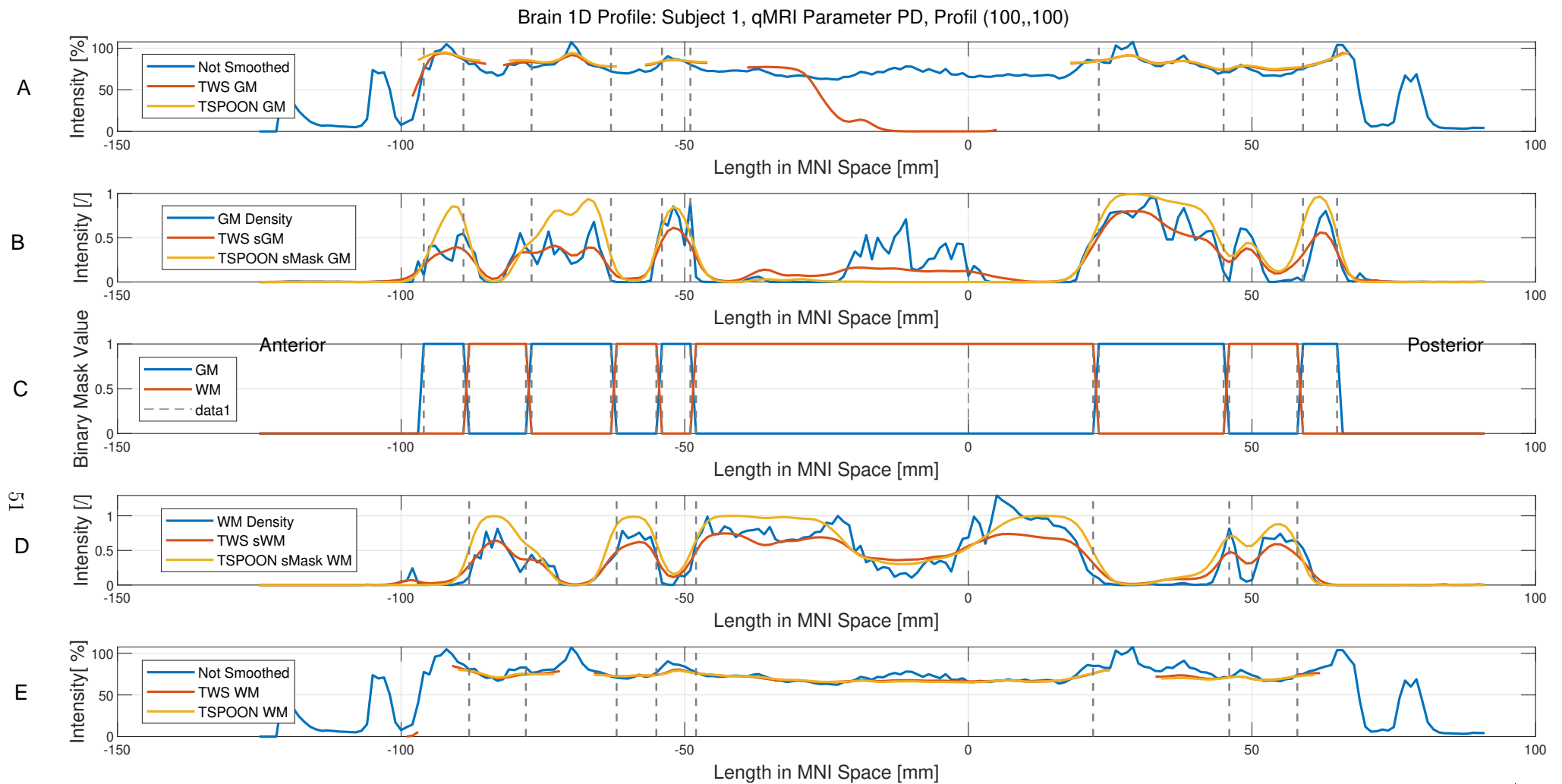


Figure 4.18: Brain 1D profile warped into MNI space for PD parameter, subject 1. Graph A show WTA masks. Graphs B and D show the TWS and TSPOON denominator signals and the tissue density signal. Graphs A and E show the TWS and TSPOON smoothed signals and the original one. The results are showed in both GM and WM.

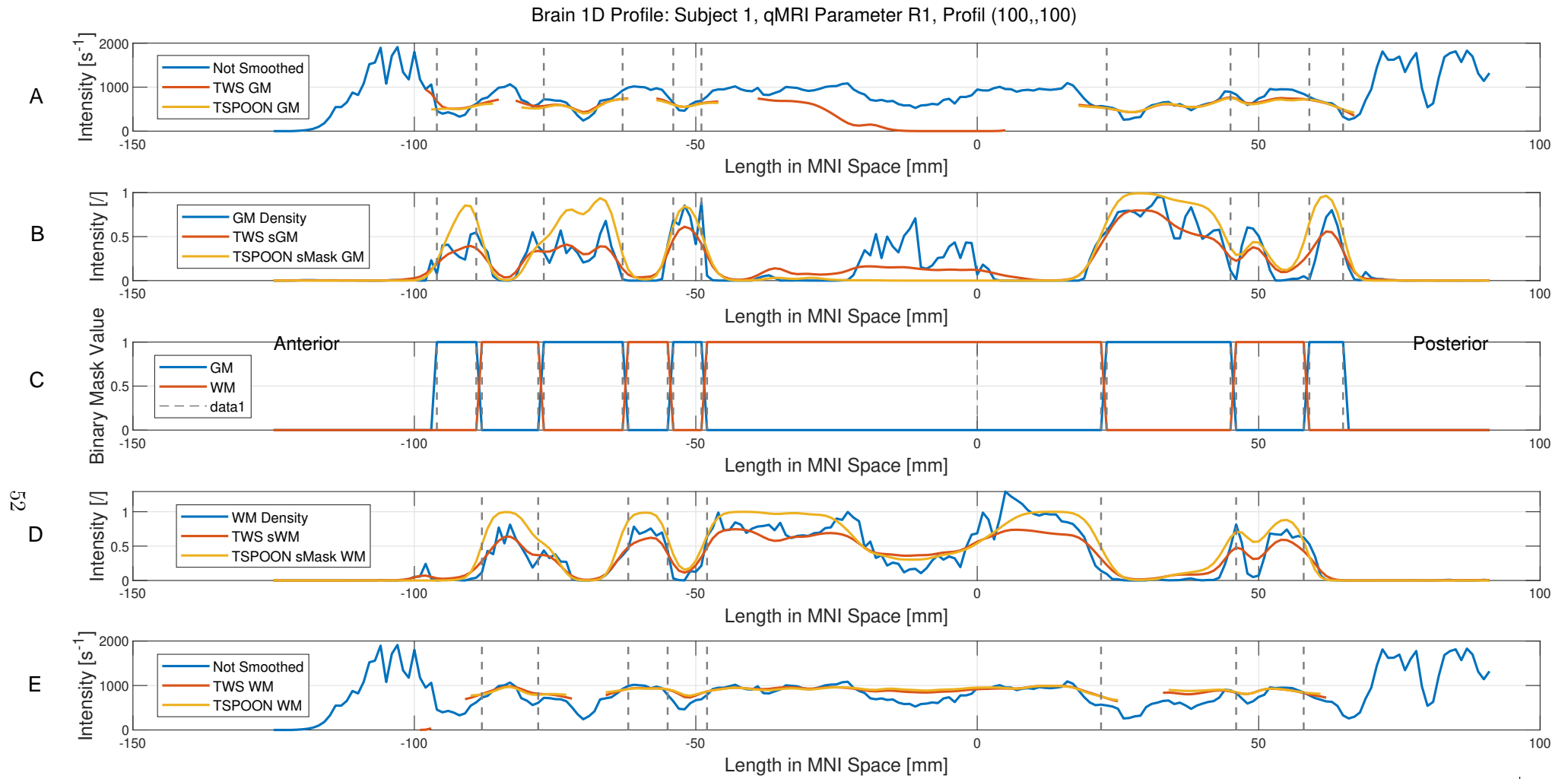


Figure 4.19: Brain 1D profile warped into MNI space for R1 parameter, subject 1. Graph A show WTA masks. Graphs B and D show the TWS and TSPOON denominator signals and the tissue density signal. Graphs A and E show the TWS and TSPOON smoothed signals and the original one. The results are showed in both GM and WM.

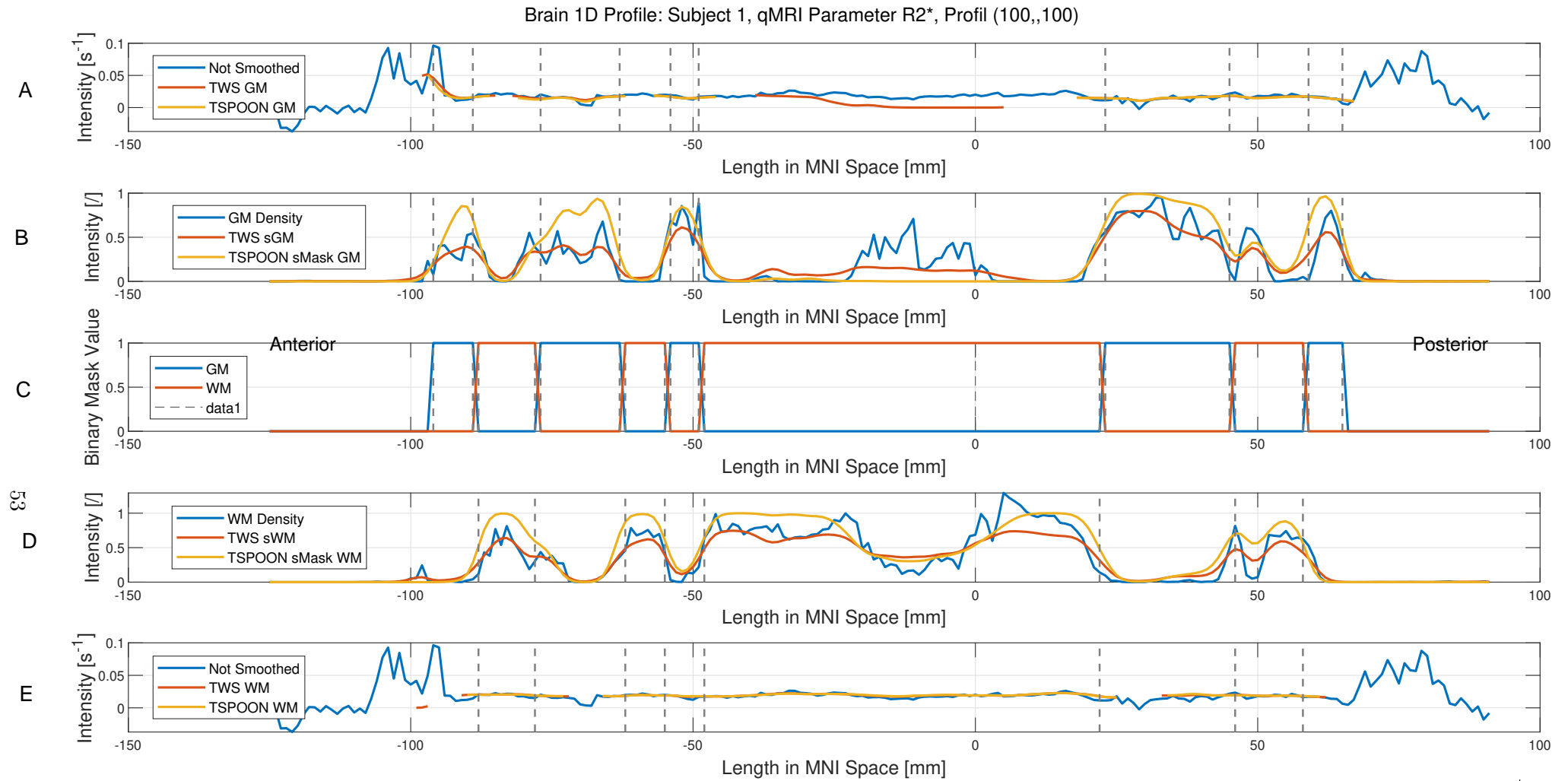


Figure 4.20: Brain 1D profile warped into MNI space for R2* parameter, subject 1. Graph A show WTA masks. Graphs B and D show the TWS and TSPOON denominator signals and the tissue density signal. Graphs A and E show the TWS and TSPOON smoothed signals and the original one. The results are showed in both GM and WM.

We begin the analysis of these graphs by noting that the intensity of warped signals in MNI space varies depending on the qMRI parameter, as expected due to the differing measurements involved. This variation allows for the analysis of the smoothing behavior under varying signal amplitudes.

Within the analyzed tissue classes (indicated by dashed vertical lines), the TWS and TSPOON smoothing methods yield similar signals for **R2*** (Figure 4.20). However, subtle differences are evident, such as the faster decline of the TSPOON signal compared to TWS around -90 mm in gray matter, after which the signals converge. Additionally, around -70 mm in GM, the TSPOON signal displays a dip that is slightly weaker than that of TWS.

This pattern is further observed for the **MTsat** parameter in Figure 4.17, with differences evident around 70 mm in GM and -80 mm in white matter. Conversely, for the **PD** parameter in Figure 4.18, the TSPOON signal surpasses that of TWS, particularly in GM at -90 mm and -70 mm, as well as in WM around -80 mm. For the **R1** parameter (Figure 4.19), however, this trend reverses: the TSPOON signal is weaker than TWS in white matter at -80 mm and in gray matter at -90 , -70 and -55 mm.

Focusing on the extensive white matter segment between approximately -50 and 20 mm, the **R1** parameter in Figure 4.19 reveals that the TSPOON signal remains relatively constant, while the TWS signal exhibits minor fluctuations, including a slight increase near -30 mm and decreases around -20 and 0 mm. Similar trends are noted for the **PD** parameter in Figure 4.18, with the TWS signal showing slight increases around -20 and 0 mm. The MTsat parameter corroborates this behavior, whereas the low amplitude of the R2* signal precludes such observations.

On a broader scale, the denominator signal for TSPOON often exceeds that of TWS. The TSPOON denominator signal stabilizes into plateaus (regions of near-constant value) predominantly within extensive segments of uniform tissue, while smaller tissue regions exhibit minimal stabilization. Conversely, the TWS denominator stabilizes more readily within small tissue regions and aligns closely with the tissue density signal, giving the impression of additional smoothing. This behavior is particularly pronounced when incorporating TPMs (with a 5% threshold). In the extensive white matter segment, however, the TWS denominator displays fewer plateaus compared to TSPOON but also exhibits fewer peaks.

Finally, it is worth noting an additional observation: the TWS signal occasionally extends into regions where it should not be present. While this characteristic is not problematic (since tissue masks are applied during the merging of results) it remains independent of the qMRI parameter considered. This is evident, for example, in the TWS signal within gray matter between -35 and 5 mm and in white matter around -95 mm.

Merged Signals

We now turn our attention to the signal resulting from the fusion of the gray matter and white matter signals, accounting for the GM and WM tissue masks. This fusion can be interpreted as the reconstruction of a single brain image, which may have practical utility in certain applications. In our analysis, this merged signal allows us to examine the behavior of the two smoothing methods during the integration of gray and white matter, offering an opportunity to identify potential trends at the boundaries between these two tissue classes.

Figure 4.21 illustrates the merged signal for the qMRI R1 parameter, selected due to its high amplitude. Nonetheless, analogous observations can be made for the other qMRI parameters, as detailed in Appendix B.5.

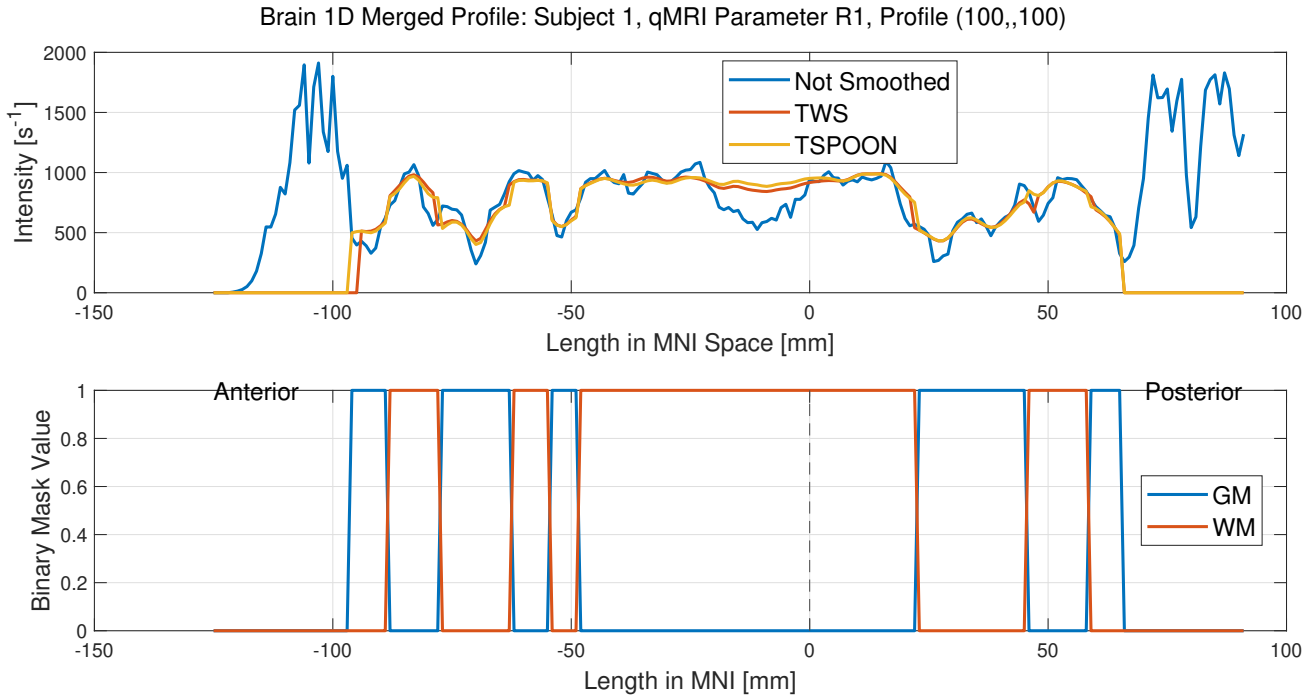


Figure 4.21: Brain 1D Profile for R1 parameter, subject 1: TWS and TSPOON smoothed and merged signals.

The transitions between gray and white matter generally exhibit expected behavior, as they align closely with the initial normalized MNI signal without introducing significant anomalies for either smoothing method. However, subtle differences between the two methods are evident at specific locations, including around -90 , -78 , -63 , 22 , 45 , and 58 mm. It is noteworthy that in other GM/WM or WM/GM transitions, no discernible differences are observed between the TSPOON and TWS signals.

At approximately -90 mm, the TSPOON signal exhibits a quicker onset compared to the TWS signal. However, it is important to note that this transition involves a non-considered tissue class (i.e. here transition between CSF and GM). In contrast, at -78 mm and -63 mm, the TWS signal shows more pronounced decreases and increases during WM/GM and GM/WM transitions, respectively. Similarly, at 22 mm, the WM/GM transition is initiated by the TWS signal, followed by the TSPOON signal.

A particularly notable difference is observed at 45 mm, where the TSPOON signal forms an upward peak while the TWS signal exhibits a downward peak. This discrepancy may be attributable to a phase shift, with TWS responding slightly ahead of TSPOON. Consequently, TWS reflects the decline of the warped signal in MNI space while TSPOON still captures its rise. Lastly, at 58 mm, the TSPOON signal is observed to decrease first during a WM/GM transition.

As described in Sections 3.1.1 and 3.3, the complete brain image was reconstructed to obtain the merged signals in GM and WM. Figure 4.22 shows the quantitative maps warped into MNI space and smoothed using TWS and TSPOON for subject 1 and MTsat parameter. A visual inspection reveals that the central white matter appears more uniform with TSPOON than with TWS. This observation supports the notion that TSPOON is less sensitive to fine variations within large regions of the same tissue type, as exemplified in Figure 4.19, which shows that the TSPOON signal remains relatively constant, while the TWS signal exhibits minor fluctuations.

Note: Large regions of the same tissue type are observed only for WM, not for GM. This may be

explained by the fact that GM can be considered, to some extent, as an envelope surrounding WM.

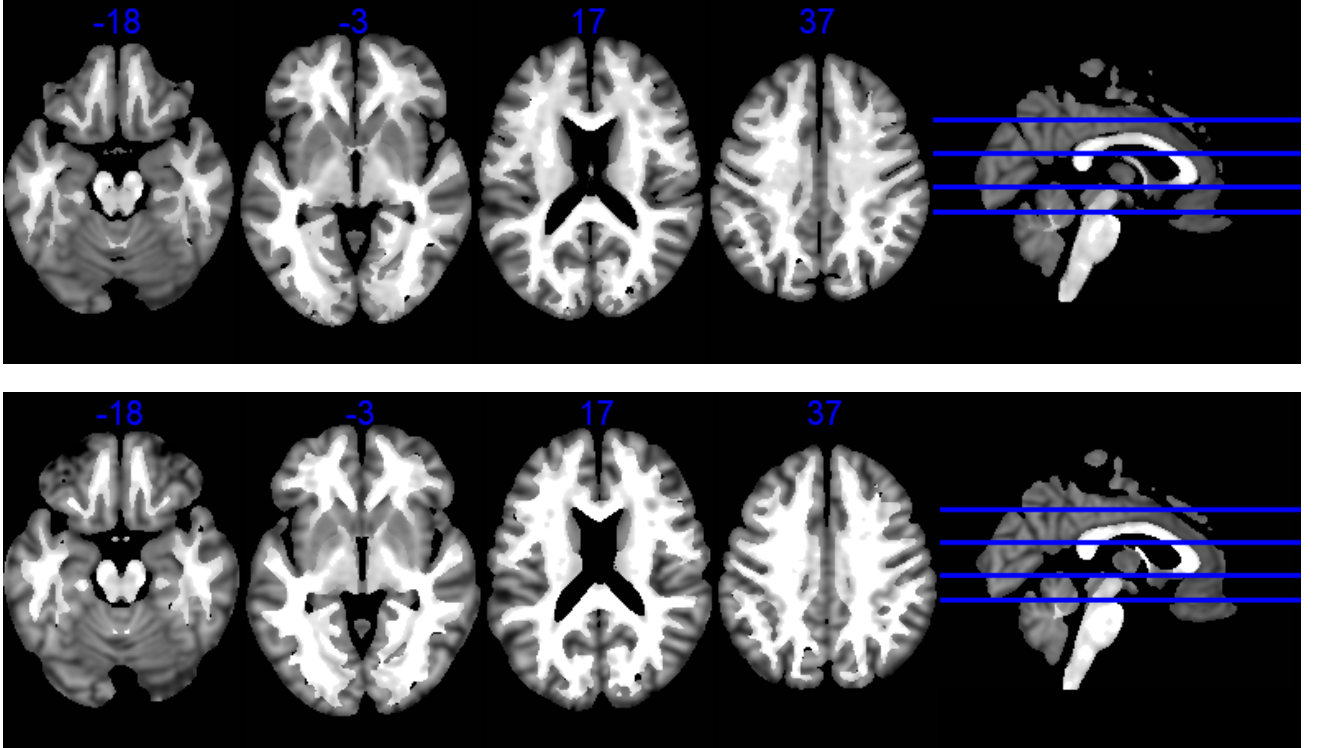


Figure 4.22: Quantitative maps warped into MNI space and smoothed using TWS (top image) and TSPOON (bottom image) for subject 1 and MTsat parameter. The four axial slices are located at $z = -18, -3, 17$ and 37 mm, from left to right, as illustrated on the sagittal slice (right).

4.2 fMRI

This section presents the results obtained from the analysis detailed in Section 3.4. To maintain clarity and focus, only the most pertinent findings are discussed here, while additional results are provided in Appendix C.

From the first-level statistical analysis outlined in Section 3.1.2, only the "*T-contrast Faces > Scrambled Faces*" is considered. This specific contrast was selected among others due to its representation of a broad functional test, making it particularly suitable for this exploratory study. For the second-level statistical analysis described in Section 3.4, attention is restricted to the two F-contrasts that reveal all spatial differences in gray matter and white matter.

Figure 4.25 highlight the regions of the statistical parametric map where the contrast map *Faces > Scrambled Faces* is significantly influenced by the smoothing methods. This figure demonstrate that, in both gray matter and white matter, the choice of smoothing method has a significant impact on specific regions. Although these significant regions are smaller than those found in the qMRI dataset (Section 4.1.2), they are still present. It is worth noting that, as expected, they generally appear to concentrate on the boundary regions between GM and WM. This could suggest that interfaces between different tissue types are sensitive to smoothing, thereby influencing the partial volume effect (PVE), including in fMRI.

Figures 4.23 and 4.24 present data from the statistical parametric maps, highlighting the regions where the contrast map *Faces > Scrambled Faces* is significantly influenced by the smoothing methods. It is

particularly noted that a height statistical T threshold of 8.0302 was applied to threshold these regions in both GM and WM.

The figures also show that the effective smoothing is higher in GM (FWHM: $x = 5.9$ mm, $y = 5.6$ mm, $z = 6.5$ mm) than in WM (FWHM: $x = 4.8$ mm, $y = 4.7$ mm, $z = 5.7$ mm). This can be explained by differences in signal properties specific to MRI types. fMRI data measure variations in the BOLD signal, which are strongly influenced by oxygenation and blood flow (Section 2.1). These variations are more localized and distinct in GM, where neuronal networks are denser and neuronal activity is directly associated with the BOLD signal (Section 1.1). In WM, where the BOLD signal is generally weaker, activations are less pronounced, resulting in less prominent smoothing. This explains why effective smoothing is greater in GM than in WM in fMRI.

Additional significant results are observed at the uncorrected threshold of $p < 0.001$ for regions of the statistical parametric map where the contrast maps *Faces* > *Scrambled Faces* exhibit notable increases across the three smoothing methods in both gray and white matter. These findings are presented in Appendix C.

Statistics: *p*-values adjusted for search volume

set-level		cluster-level				peak-level					mm mm mm		
<i>p</i>	<i>c</i>	<i>p</i> _{FWE-corr}	<i>q</i> _{FDR-corr}	<i>k</i> _E	<i>p</i> _{uncorr}	<i>p</i> _{FWE-corr}	<i>q</i> _{FDR-corr}	<i>F</i>	(<i>Z</i> _E)	<i>p</i> _{uncorr}			
0.358	34	0.888	0.446	6	0.069	0.028	0.054	19.75	4.86	0.000	-28	-62	-48
		1.000	0.446	2	0.277	0.052	0.054	18.65	4.74	0.000	20	-6	-16
		1.000	0.446	2	0.277	0.923	0.905	12.42	3.91	0.000	-6	24	24
		0.997	0.446	3	0.186	0.993	0.905	11.25	3.71	0.000	52	-10	16
		1.000	0.446	2	0.277	0.996	0.905	11.02	3.67	0.000	40	-4	10
		1.000	0.446	1	0.446	0.997	0.905	10.99	3.67	0.000	-12	-46	66
		0.984	0.446	4	0.131	0.998	0.905	10.79	3.64	0.000	26	-80	24
		0.997	0.446	3	0.186	0.999	0.905	10.51	3.58	0.000	26	-8	-14
		1.000	0.446	1	0.446	1.000	0.905	10.38	3.56	0.000	16	-76	-34
		1.000	0.446	2	0.277	1.000	0.905	10.24	3.54	0.000	-54	-46	-10
		1.000	0.446	1	0.446	1.000	0.905	9.99	3.49	0.000	24	-36	6
		1.000	0.446	1	0.446	1.000	0.905	9.84	3.46	0.000	34	-4	10
		1.000	0.446	1	0.446	1.000	0.905	9.66	3.43	0.000	10	48	18
		1.000	0.446	1	0.446	1.000	0.905	9.48	3.39	0.000	14	-98	6
		1.000	0.446	1	0.446	1.000	0.905	9.33	3.36	0.000	-24	-56	-20
		1.000	0.446	1	0.446	1.000	0.905	9.33	3.36	0.000	-56	-8	-10
		1.000	0.446	1	0.446	1.000	0.905	9.27	3.35	0.000	34	-40	-14
		1.000	0.446	1	0.446	1.000	0.905	9.24	3.34	0.000	-36	8	46
		1.000	0.446	2	0.277	1.000	0.905	9.19	3.33	0.000	58	-32	2
		1.000	0.446	1	0.446	1.000	0.924	9.07	3.31	0.000	-6	-46	-10

table shows 3 local maxima more than 8.0mm apart

Height threshold: $F = 8.03$, $p = 0.001$ (1.000)
 Extent threshold: $k = 0$ voxels
 Expected voxels per cluster, $\langle k \rangle = 1.830$
 Expected number of clusters, $\langle c \rangle = 31.61$
 FWEp: 18.717, FDRp: Inf, FWEc: Inf, FDRc: Inf

Degrees of freedom = [2.0, 47.0]
 FWHM = 5.9 5.6 6.5 mm mm mm; 2.9 2.8 3.2 {voxels}
 Volume: 381008 = 47626 voxels = 778.7 resels
 Voxel size: 2.0 2.0 2.0 mm mm mm; (resel = 26.46 voxels)
 Page 1

Figure 4.23: Data on the statistical parametric map showing regions where the contrast map *Faces* > *Scrambled Faces* is significantly affected by the smoothing methods in GM, at the $p < 0.001$ uncorrected level.

Statistics: *p-values adjusted for search volume*

set-level		cluster-level				peak-level					mm mm mm		
p	c	$p_{\text{FWE-corr}}$	$q_{\text{FDR-corr}}$	k_E	p_{uncorr}	$p_{\text{FWE-corr}}$	$q_{\text{FDR-corr}}$	F	(Z_E)	p_{uncorr}			
0.012	52	1.000	0.325	1	0.325	0.139	0.315	16.58	4.49	0.000	-14	-4	30
		1.000	0.325	1	0.325	0.176	0.315	16.18	4.44	0.000	30	2	14
		0.998	0.325	2	0.168	0.570	0.569	14.24	4.18	0.000	24	42	8
		0.998	0.325	2	0.168	0.896	0.663	13.07	4.01	0.000	42	-12	-20
		1.000	0.325	1	0.325	0.919	0.663	12.88	3.98	0.000	-42	4	-32
		0.972	0.325	3	0.096	0.959	0.663	12.43	3.91	0.000	-24	-58	32
		0.998	0.325	2	0.168	0.963	0.663	12.36	3.90	0.000	44	-28	-12
		1.000	0.325	1	0.325	0.999	0.882	11.10	3.69	0.000	14	12	26
		0.998	0.325	2	0.168	1.000	0.882	10.79	3.63	0.000	-24	-20	38
		1.000	0.325	1	0.325	1.000	0.882	10.54	3.59	0.000	-18	-32	2
		1.000	0.325	1	0.325	1.000	0.882	10.33	3.55	0.000	36	-40	-8
		1.000	0.325	1	0.325	1.000	0.882	10.29	3.54	0.000	0	-30	-18
		1.000	0.325	1	0.325	1.000	0.882	10.28	3.54	0.000	-14	0	50
		1.000	0.325	1	0.325	1.000	0.882	10.27	3.54	0.000	-20	-56	28
		0.998	0.325	2	0.168	1.000	0.882	10.23	3.53	0.000	-30	-36	46
		1.000	0.325	1	0.325	1.000	0.882	10.20	3.53	0.000	-26	4	20
		0.998	0.325	2	0.168	1.000	0.882	10.17	3.52	0.000	-8	-20	-24
		0.887	0.325	4	0.059	1.000	0.882	10.13	3.52	0.000	34	-38	26
		0.972	0.325	3	0.096	1.000	0.908	9.88	3.47	0.000	28	32	16
		0.998	0.325	2	0.168	1.000	0.908	9.86	3.46	0.000	14	-6	34

table shows 3 local maxima more than 8.0mm apart

Height threshold: $F = 8.03$, $p = 0.001$ (1.000)Extent threshold: $k = 0$ voxelsExpected voxels per cluster, $\langle k \rangle = 1.114$ Expected number of clusters, $\langle c \rangle = 37.09$

FWEp: 18.361, FDRp: Inf, FWEc: Inf, FDRc: Inf

Degrees of freedom = [2.0, 47.0]

FWHM = 4.8 4.7 5.7 mm mm mm; 2.4 2.4 2.8 {voxels}

Volume: 312192 = 39024 voxels = 1427.2 resels

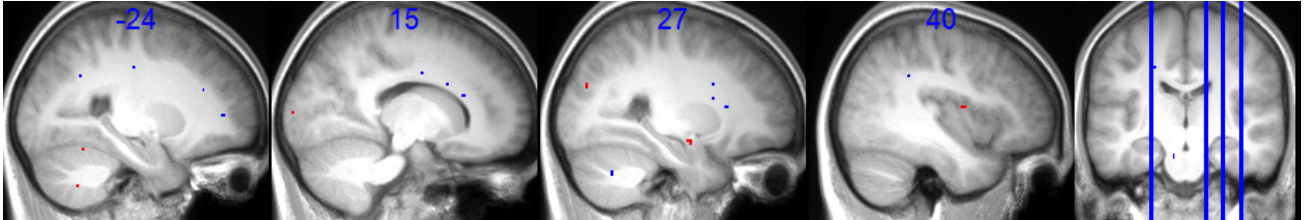
Voxel size: 2.0 2.0 2.0 mm mm mm; (resel = 16.11 voxels)

Page 1

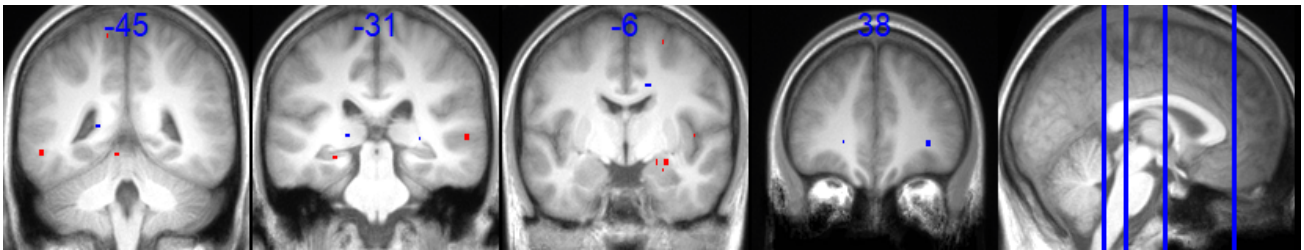


1

Figure 4.24: Data on the statistical parametric map showing regions where the contrast map *Faces* > *Scrambled Faces* is significantly affected by the smoothing methods in WM, at the $p < 0.001$ uncorrected level.



The four sagittal slices are located at $z = -24, 15, 27$ and 46 mm, from left to right, as illustrated on the coronal slice (right).



The four coronal slices are located at $z = -45, -31, -6$ and 38 mm, from left to right, as illustrated on the sagittal slice (right).

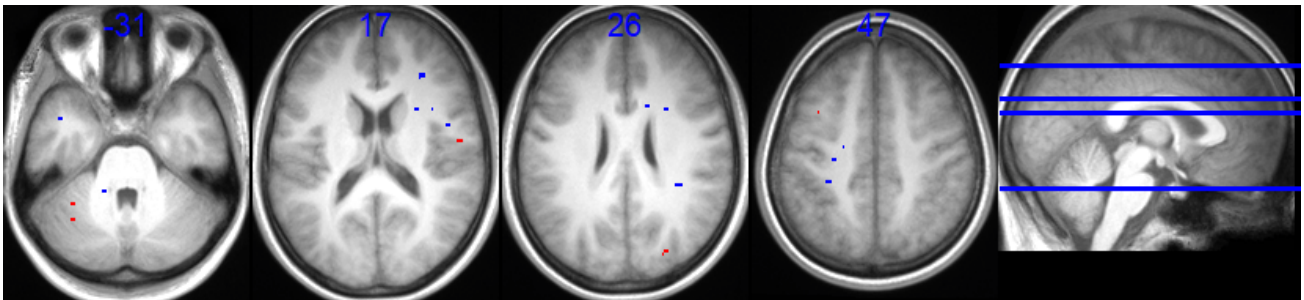


Figure 4.25: Statistical parametric maps identifying regions (red for GM and blue for WM) in which the contrast map *Faces* > *Scrambled Faces* is significantly affected by the smoothing methods, at the $p < 0.001$ uncorrected level. The results are superimposed on the mean T1w anatomical map for the cohort in MNI space. The four axial slices are located at $z = -31, 17, 28$ and 47 mm, from left to right, as illustrated on the sagittal slice (right).

Chapter 5

Discussion

5.1 Quantitative MRI

In this section, qMRI results will be discussed by distinguishing two types of results. The first ones come from the statistical parametric maps (SPM) that reproduce the results of the article by Callaghan and al. [2] (Section 4.1.1) and their statistics in Section 4.1.1. While the second ones come directly from the smoothed quantitative maps in Sections 4.1.2 and 4.1.3.

5.1.1 SPM-Based

Before delving into this first part of the discussion, it is important to put things into perspective. An approach that identifies more significant regions is not inherently superior to another. A significant region indicates activation based on a statistical test, which is performed on a quantitative map derived from processed measurements of signals acquired during the image acquisition. While this process aims to approximate reality as closely as possible, it does not guarantee that a statistically significant region is also biologically meaningful.

For the **MTsat** parameter, we examine the results of the AR- contrast. MTsat reveals an enlargement of large significant regions with TSPOON and a proliferation of smaller significant regions with TWS (Figure 4.1). A lower effective smoothing (reduced smoothing effect in Figure 4.5) means that TSPOON preserves more local details from the original data, while TWS applies a stronger smoothing effect. Surprisingly, TWS detects more small regions than TSPOON, which is counterintuitive.

Additionally, TWS results in larger average of T-values than TSPOON and these T-values are markedly higher in extreme cases (Figure 4.6). Similarity measures indicate a good overall correspondence between TWS and TSPOON results (Table 4.2). Furthermore, TSPOON has a higher statistical threshold (T_{thresh}) for significance in both GM and WM compared to TWS (Figure 4.10). Finally, in both GM and WM, TWS detects a greater number of significant voxels and clusters, while TSPOON exhibits larger median cluster sizes (Table 4.4).

The cluster data cannot be fully explained by the effective smoothing, which would intuitively suggest the opposite. Nevertheless, the larger median cluster size observed with TSPOON can not be attributed to its reduced smoothing effect. Indeed less intense smoothing retains fine local variations while also leading to the fragmentation of significant regions into smaller, more numerous clusters. In contrast, more intense smoothing homogenizes spatial variations, tending to group spatially proximate voxels into a single significant region, resulting in larger clusters. This idea seems even less correct since the smaller significant regions detected with TWS do not overlap with the larger significant regions identified by TSPOON.

For MTsat, observations in both GM and WM align with the following conclusions:

- TWS results in larger average of T-values than TSPOON.
- TSPOON exhibits a higher statistical threshold (T_{thresh}) for significance compared to TWS.
- TWS results on stronger effective smoothing than TSPOON.

The **PD** parameter shows that in WM, both methods produce comparable results, with TWS detecting slightly more small regions. In GM, however, almost no significant regions are observed with either method (Figure 4.2). TSPOON exhibits a smaller effective smoothing compared to TWS (Figure 4.5). Additionally, TSPOON tends to produce slightly larger average of T-values than TWS in GM, while the opposite is true in WM. Extreme cases in both tissues reveal a tendency for TWS to produce significantly higher T-values than TSPOON (Figure 4.7). Similarity measures indicate good agreement between the two methods in WM and a moderate one in GM (Table 4.2). TSPOON also demonstrates higher significance T_{thresh} than TWS in both tissues (Figure 4.10). Finally, TWS detects a greater number of significant voxels in both tissues. However, the number of significant clusters is larger with TSPOON in GM and with TWS in WM, in contrast to the median cluster size (Table 4.4).

Interpreting the GM results to identify the effect of either smoothing method is challenging. TSPOON results in larger T-values and higher significance T_{thresh} than TWS. In contrast, in WM, the results align with those observed for MTsat, forming a kind of recurring observations.

The **R1** parameter demonstrates that in WM, no significant differences between the methods can be noted, while in GM, TWS identifies larger significant regions and detects more small regions than TSPOON (Figure 4.3). In both WM and GM, TSPOON shows less effective smoothing than TWS (Figure 4.5). Furthermore, TWS results in slightly larger average of T-values than TSPOON, with much larger differences observed in extreme cases (Figure 4.8). Similarity measures indicate good overall agreement between TWS and TSPOON in WM but not in GM (Table 4.2). TSPOON also exhibits higher significance T_{thresh} than TWS in both tissues (Figure 4.10). Finally, TWS detects a greater number of significant voxels and clusters in both tissues, while TSPOON presents the largest median cluster size, which is consistent with expectations (Table 4.4).

The cluster data cannot be fully explained by effective smoothing, as previously discussed in MTsat section. However, the results in both GM and WM align with the observed recurring pattern.

The qMRI parameter **R2*** reveals that in WM, TWS identifies larger significant regions compared to TSPOON, while TSPOON detects a greater number of smaller clusters. In GM, TWS produces overall larger significant regions (Figure 4.4). In both WM and GM, TSPOON shows less effective smoothing than TWS (Figure 4.5). Compared to the other qMRI parameters, R2* exhibits the smallest difference in effective smoothing values between the TWS and TSPOON approaches in both tissues. In GM, TWS results in slightly larger average of T-values than TSPOON, while the reverse is true in WM (Figure 4.9). Additionally, R2* in WM shows the smallest mean difference and the narrowest limits of agreement. Similarity measures indicate good overall correspondence between TWS and TSPOON results in both GM and WM (Table 4.2). TSPOON demonstrates higher significance T_{thresh} than TWS in GM, while the opposite is true in WM (Figure 4.10). Finally, TWS identifies a greater number of significant voxels and clusters in both tissues, while TSPOON consistently produces the largest median cluster sizes (Table 4.4).

The cluster data cannot be fully explained by effective smoothing, as previously discussed in MTsat section. The R2* results in GM align with the observed recurring pattern, while interpreting the ones in WM is more challenging. TWS exhibits stronger effective smoothing, higher significance thresholds and slightly lower intensity values than TSPOON, which may seem paradoxical.

Recurring Pattern Discussion

The observation that TSPOON has a higher statistical threshold T_{thresh} for significance despite lower T-values average and weaker smoothing appears in GM for MTsat, R1 and R2* and in WM for MTsat, PD and R1. This observation can initially appear counterintuitive. However, this can be explained by the following intuitive approach.

In the context of controlling the family-wise error rate (FWE), the statistical threshold T_{thresh} increases as the number of independent comparisons increases. This phenomenon applies to all FWE correction methods, albeit with nuances depending on the specific approach employed, such as Bonferroni correction, Random Field Theory (RFT) or permutation-based methods.

The purpose of FWE correction is to control the global risk of Type I errors across multiple statistical tests. When data are more independent, the number of effective comparisons increases because there is less redundancy between tests. This increase in independent tests necessitates stricter thresholds (T_{thresh}) to maintain the desired overall significance level (e.g., $\alpha = 0.05$). For example, in the Bonferroni correction, which assumes full independence, the threshold is adjusted linearly based on the total number of tests. In RFT, the number of comparisons is moderated by accounting for spatial dependencies introduced by smoothness. While T_{thresh} still increases with the number of independent tests, the dependency structure reduces the total number of effective comparisons. Permutation-based methods empirically estimate the distribution of test statistics and adjust T_{thresh} accordingly. If the data are highly independent, the permutation approach identifies more extreme values, leading to stricter thresholds.

The independence of data plays a central role. When data are spatially or temporally dependent (e.g., smoothed neuroimaging data), the effective number of comparisons is reduced. This lowers the stringency of the threshold because dependencies group nearby or similar tests together. Conversely, in datasets with minimal dependence (e.g., non-lissée neuroimaging data or independent voxel-level comparisons), each test contributes uniquely, increasing the effective number of comparisons and therefore T_{thresh} .

Although all FWE correction methods align with the general principle that T_{thresh} rises with increasing independence, the exact relationship varies. Bonferroni correction treats all comparisons as independent, making it the most straightforward and conservative approach. RFT adjusts for spatial smoothness, resulting in a less strict T_{thresh} when compared to Bonferroni for highly smoothed datasets. Permutation-based methods adaptively model independence by analyzing the data's empirical behavior, which can lead to thresholds tailored to the specific dataset.

Thus, the statistical threshold T_{thresh} increases with the number of independent comparisons, reflecting the independence of the underlying data. This independence of the data could be explained by the effective smoothing in particular.

Effective smoothing could influence the number of independent comparisons by altering the spatial correlation of voxels. Heavily smoothed data results in neighboring voxels having more similar intensity values, reducing the number of independent comparisons because smoothed voxels are more correlated. In practice, this means fewer independent statistical tests are required, as neighboring voxels provide redundant information. Conversely, minimal smoothing increases the number of independent voxels, leading to a greater total number of statistical tests and necessitating stricter significance thresholds to control the false discovery rate.

Thus, the observations repeatedly made in GM for MTsat, R1, and R2*, and in WM for MTsat, PD and R1, could suggest that TSPOON exhibits voxels in the SPM that are more independent from each other than those in TWS, as indicated by the higher statistical thresholds and the smaller effective

smoothing in TSPOON.

5.1.2 Smoothed Quantitative Maps -Based

In this section the qMRI results from the smoothed quantitative maps will be discussed by distinguishing two types of results. The first are those that apply a one-sample t-test on the difference of TWS and TSPOON signals in Section 4.1.2. The second ones come from the more intuitive approach of the 1D cranial profile in Section 4.1.3.

Spatial Differences Induced By Smoothing

In the context of the differences induced by smoothing (Section 4.1.2) and the observations regarding TSPOON and TWS, several interpretations can be drawn based on the identified differences.

Overall, many brain regions are significantly influenced by the smoothing approach employed. However, these effects are predominantly localized to the borders between GM and WM, underscoring the relevance of this study for partial volume effect (PVE) management. Notably, the $R2^*$ parameter exhibits substantial differences induced by smoothing within GM, while the effects in WM are nearly negligible. This suggests an opportunity for further investigation into the behavior of the $R2^*$ parameter in WM, particularly given its distinct characteristics following the application of the GLM in Section 5.1.1.

The minimal significant regions observed within GM can be better understood by analyzing the contrast image directly, without applying a significance threshold. Figures D.1 and D.2 illustrate the contrast images showing areas where the $R2^*$ parameter is influenced by the difference between TWS and TSPOON smoothing methods in GM and WM, respectively. The map derived from GM displays relatively uniform intensities (ranging from 0 to approximately 100), while the map derived from WM exhibits much greater variability (ranging from 0 to over 1200). It is well-established that increased variability reduces statistical power, complicating the detection of significant differences due to noisier or less homogeneous signals. This elevated variability in WM is unlikely to result from anatomical factors (e.g., the complexity of axone fibers and their orientation), as other qMRI parameter maps derived from WM do not display such effects. Instead, this variability may be attributed to biophysical factors specifically associated with the $R2^*$ parameter, such as iron concentration or magnetic properties.

The distinct behavior of the $R2^*$ parameter compared to other parameters in WM is also evident during a straightforward calculation of the difference between the two quantitative maps smoothed using TWS and TSPOON. For example, the difference in $R2^*$ values in WM (Figure D.4) is extremely small and barely perceptible, unlike the differences observed for other qMRI parameters in the same tissue type, as demonstrated with MTsat (Figure D.3). This behavior aligns with the Bland-Altman plot, where the $R2$ parameter in WM (Figure 4.9) shows a very low mean difference and narrow agreement limits, indicating excellent consistency between the two smoothing methods for this parameter in WM.

Figures D.3 and D.4 suggest that the smoothed signal intensity from TSPOON may be lower than that of TWS. When examining medians and means across various quantitative maps, tissue classes and subjects, it becomes evident that TWS consistently exhibits a higher median signal than TSPOON, whereas TSPOON shows a higher mean signal than TWS. This trend is particularly pronounced for qMRI parameters with larger amplitude ranges. For instance, in subject 16, the TWS-TSPOON difference for $R1$ in GM is -4.9734 , and the median is 2.0382 , indicating that TWS has a higher median but a lower mean compared to TSPOON.

A higher mean suggests that the strongest intensities significantly influence the overall signal, reflecting TSPOON's enhanced sensitivity to regions with pronounced gradients or localized anomalies. This

is particularly relevant at tissue boundaries, where the effects of smoothing differences are most apparent. Conversely, the lower median observed with TSPOON indicates that the majority of voxels in the smoothed signal exhibit lower intensities compared to TWS. This suggests that TSPOON produces a more contrasted signal distribution, emphasizing extreme values in regions with high signal intensity.

The higher mean signal of TSPOON may indicate its capacity to amplify critical gradients or regions of high intensity while maintaining contrast with neighboring areas. This can be advantageous for analyses focusing on highly differentiated regions, such as tissue boundaries. The lower median may reflect TSPOON's ability to de-emphasize minor variations or artifacts in homogeneous regions, reducing noise and enhancing reliability in low-contrast areas.

However, a higher mean signal can introduce bias if statistical analyses disproportionately rely on these high-intensity regions, potentially limiting the detection of subtle variations or patterns. The lower median suggests that regions of low signal intensity contribute less to the final model, which could pose challenges in studies where these subtle variations hold biological significance (e.g., in less homogeneous cortical regions).

On the other hand, with a higher median and lower mean, TWS offers a more evenly distributed signal, making it potentially better suited for detecting fine variations or conducting global analyses, as confirmed by the comparison between the results in Section 5.1.1. Conversely, with a higher mean and lower median, TSPOON favors strong contrasts and well-defined regions, which might make it more robust for analyses requiring high local precision.

To expand on this discussion, one could assess whether the F-test on the global dependence of qMRI parameters on the difference between TWS and TSPOON remains significant at a p-value threshold of 0.05, FWE corrected. Using the MTsat parameter as an example, the F-height threshold for MTsat in GM is 32.967 at the FWE-corrected level ($p < 0.05$), while for WM, it is 32.097 at the same significance level. These results are depicted in Figure D.5, which shows significant regions spanning many brain areas but remaining concentrated at the borders between tissue classes, as highlighted in slices at $z = 15$ and 32 mm.

1D Brain Profile Analysis

In the context of this 1D brain profile analysis (Section 4.1.3) and the observations regarding TSPOON and TWS, several interpretations can be drawn based on the identified differences. TSPOON appears more responsive, exhibiting lower minima and higher maxima. This greater responsiveness suggests that TSPOON is better able to capture pronounced or localized variations, likely due to its heightened sensitivity to abrupt changes in the signal. This responsiveness is likely tied to TSPOON's lighter smoothing method, which preserves steeper gradients and slopes. This capability could be particularly advantageous in identifying critical changes in areas with significant variability, such as interfaces between different tissue types.

Additionally, TSPOON demonstrates more consistent signals over long segments compared to TWS (Figures 4.19 and 4.22). This consistency may result from more spatially coherent smoothing, where TSPOON suppresses irrelevant or undesirable variations while preserving the overall structure of the data. Signal variations within a long segment may not be steep enough to cause significant signal variation in TSPOON. In contrast, TWS tends to preserve more anatomical details, which can be an advantage in specific contexts.

Furthermore, TSPOON's denominator is also more sensitive than that of TWS, indicating that TSPOON is better suited to detecting localized variations, especially in smaller regions where pronounced variations are present. This further supports the hypothesis. In contrast, TWS follows the density signal

more closely.

From all these elements, a hypothesis may arise: TSPOON is more sensitive to pronounced and localized signal variations near tissue boundaries than TWS. On the other hand, TWS is more sensitive to subtle signal variations occurring within the core of a tissue.

5.2 Functional MRI

In this section, the fMRI results from Section 4.2 are discussed.

Figure 4.25 illustrates the statistical parametric map identifying regions where the contrast map *Faces* > *Scrambled Faces* is significantly influenced by the smoothing methods (GS, TWS, and TSPOON) at the $p < 0.001$ uncorrected level. It was also observed that these regions tend to be located near the boundary between GM and WM. This observation aligns with findings from the qMRI results, which demonstrated smoothing-induced differences are mostly located near the tissues boundary in Section 4.1.2.

5.3 Global Discussion

In this final part we will try to bring together the ideas held in the previous parts of the discussion relating to specific results. Here are the main ideas that emerged from the various discussions:

- **From SPM-based Discussion in qMRI:** TSPOON results in consistently lower effective smoothing than TWS. TSPOON often results in higher statistical significance thresholds than TWS. This suggests that TSPOON presents voxels in the SPMs that are more independent of each other than those in TWS.
- **From Discussions on Smoothing-Induced Differences in fMRI and qMRI:** The smoothing-induced differences observed in qMRI and fMRI are mainly found at the boundaries between GM and WM. Additionally, from the quantitative maps, it can be said that TSPOON results in a more contrasted signal distribution but lower median intensity, unlike TWS.
- **From Discussion on Brain 1D Profile in qMRI:** TSPOON is more sensitive to pronounced and localized signal variations near tissue boundaries than TWS. On the other hand, TWS is more sensitive to subtle signal variations occurring within the core of a tissue.

First, we aim to determine whether the consistently higher effective smoothing of TWS and the sensitivity of TSPOON to strong gradients, combined with its insensitivity to weaker gradients, can be mathematically explained.

To begin, the systematic difference in effective smoothing appears to stem from the fundamental definitions of the two smoothing approaches, rather than from any specific qMRI parameter or tissue class.

The sensitivity of TSPOON's denominator to higher variations can be traced back to its mathematical formulation. In TWS, the denominator is defined as $g * w$, where w represents modulated tissue weights in standard space derived from the Jacobian determinants of deformation ϕ and the tissue class image warped by ϕ (Section 3.2.2). Thus, the weighting of the TWS is continuous in nature. In TSPOON, the denominator is $g * M_{TC}$, based on a binary tissue-specific mask M_{TC} (Section 3.2.3). This binary mask is less influenced by small spatial variations (as seen with w in TWS). This can be explained by the discrete nature of the mask formed from the "Majority and Greater than 20%" criterion. The TSPOON compensation is therefore more robust due to its strict categorization of tissues (WM, GM, etc.). This strict categorization makes TSPOON's weighting more sensitive by capturing clear, defined variations

without being "diluted" by continuous or noisy values, as occurs with TWS.

This analysis also provides insight into why TSPOON appears more sensitive to strong variations and less sensitive to weak variations compared to TWS. Since w is continuous, TWS attenuates weaker variations less and takes low contrast areas more into account. This makes TWS more responsive to weaker variations but less effective at clearly differentiating regions with strong variations, as the smoothing effects "dilute" distinct variations. This might also tend to increase partial volume effects (PVE). In contrast, TSPOON's binary M_{TC} , shaped by the mask's formation, allows smoothing to primarily integrate distinct variations while ignoring minor variations in more homogeneous regions (i.e. within a same tissue). Consequently, strong variations are better preserved, while weaker variations, not emphasized by M_{TC} , remain less significant.

This could explain TSPOON's stability in long tissue segments. The discrete weighting of TSPOON also explains the constancy of TSPOON within large regions of the same tissue while the continuous weighting of TWS allows to be more sensitive to fine variations within a tissue. The absence of masking used in the weighting of TWS also explains why a TWS signal specific to tissue A can exist in regions belonging to tissue B.

Effective smoothing may also be influenced by the weighting of TWS and TSPOON. TWS applies smoothing based on modulated and continuous weights, favoring a wider diffusion of information while TSPOON uses a binary mask that constrains the smoothing to specific regions, thus limiting the impact on neighboring areas. This constraint limits the extent of smoothing, potentially explaining why TSPOON consistently exhibits lower effective smoothing than TWS.

The use of an optimized mask in TSPOON may also reduce the impact of spurious or irrelevant signals by focusing solely on regions where the data are valid or significant, thereby improving the robustness of results. The mask in TSPOON appears to offer additional protection against artifacts and optimizes computational efficiency by more strictly limiting signal definition to tissue-specific regions (as opposed to TWS, where GM components may appear in WM sections). This is particularly advantageous for large-scale neuroimaging analyses.

This discussion highlights the critical importance of mask design in TSPOON. Indeed, the mask has a direct implication on the weighting used in TSPOON. The formation of the mask is based on the "Majority and Greater than 20%" criterion but it could be interesting to test other ways of forming this mask.

From this discussion, we can suggest the following conclusion:

- TSPOON may be better suited if the goal is to detect highly contrasted regions or focus on pronounced variations. This approach would also be beneficial when it is important to minimize the influence of noise or variations in homogeneous areas (i.e. within a same tissue) or when the robustness of significant regions is prioritized over their overall coverage. This leads to saying that TSPOON is more specificity oriented.
- TWS is more appropriate if the aim is to capture fine, subtle variations in the data, especially in low-variation areas (i.e. within a same tissue). This enhance sensitivity by broadly incorporating smaller or weaker signals into the statistical parametric maps. This leads to saying that TWS is more sensitivity oriented.

This higher sensitivity in TWS also explains why TWS generally identifies more significant clusters than TSPOON, even in regions where TSPOON detects none in the results reproduced from the article by Callaghan and al. [2] in Section 5.1.1.

In practice, for confirmatory analyses or studies with predefined regions of interest, TSPOON offers higher robustness and confidence in identifying significant regions without incorporating spurious signals from noisy areas. When analyzing phenomena that span larger or less sharply defined regions, TWS provides broader coverage of significant areas, which can be useful for capturing the full extent of an effect. TWS might be better suited for longitudinal or population-based studies focusing on gradual or widespread changes, such as age-related alterations in brain structure or function.

Chapter 6

Conclusions & perspectives

In this section, the conclusions and future perspectives of this study on the effects of smoothing on statistical analyses are presented.

6.1 Conclusions

Magnetic Resonance Imaging (MRI) has revolutionized the study of brain structures, enabling detailed and non-invasive analysis of the human brain. In this context, quantitative MRI (qMRI) plays a crucial role by providing precise information about the physical properties of brain tissue, such as density, relaxation, and structure. These parameters are essential for better understanding the pathophysiology of various brain disorders, as well as normal variations between individuals, making qMRI an indispensable tool in biomedical research. In the other hand, functional MRI (fMRI) measures variations in brain signal in response to stimuli or cognitive tasks.

Preprocessing of MRI data, particularly spatial smoothing, is a key step in obtaining reliable and reproducible results. Smoothing aims to reduce high-frequency random noise and improve the signal-to-noise ratio (SNR). Traditional isotropic Gaussian smoothing, while effective, introduces biases near tissue boundaries due to partial volume effects (PVE), resulting in mixed signals and reduced specificity in tissue analysis.

To address these limitations, tissue-specific smoothing methods have been developed to preserve anatomical and microstructural specificity. Among these methods are Tissue-Weighted Smoothing (TWS) and Tissue-Specific smoothed compensated (TSPOON), the latter being applicable only to white matter in Diffusion-Weighted Imaging (DWI). The objective of this master thesis is to generalize TSPOON for qMRI and fMRI and to compare the effects of TWS versus TSPOON on qMRI, as well as the effects of GS, TWS and TSPOON on fMRI.

The TWS approach applies a weighting scheme based on modulated tissue weights warped to standard space. As a result, TWS employs continuous weights that are closer to the original image. In contrast, the TSPOON approach uses a compensation scheme based on binary tissue-specific masks, normalized to standard space. Its generalization involves the creation of new tissue-specific masks following the "Majority and Greater than 20%" criterion. Due to this masking-based weighting, TSPOON employs discrete weights. These differing weighting schemes directly impact the results obtained through either approach.

In qMRI, TSPOON results in an effective smoothing consistently lower than TWS. The construction of this mask inherently leads to TSPOON exhibiting a higher mean signal intensities and lower median signal intensities compared to TWS, depending on the qMRI parameters. TSPOON is therefore more sensitive to strong variations and less so to weak variations, whereas TWS, due to the more continuous nature of its weights, is more sensitive to small variations, as confirmed by the comparison of results. Ad-

ditionally, TSPOON shows generally higher statistical significance thresholds than TWS, indicating that the voxels smoothed by TSPOON require a larger number of independent comparisons. Furthermore, the differences induced by smoothing, both in qMRI and fMRI, are predominantly observed in the boundary regions between gray matter and white matter. This discussion also highlights the critical importance of mask design in TSPOON.

Based on the discussions stemming from the various results, it can be suggested that TSPOON might be better suited for detecting highly contrasted areas or focusing on strong gradients. This approach would also be advantageous if the influence of noise or variations in homogeneous regions needs to be minimized or if the robustness of significant regions is more important than their overall coverage. In contrast, the TWS approach is better suited for capturing fine, subtle variations in the data, especially in low-variation areas (i.e. within a same tissue). This enhance sensitivity by broadly incorporating smaller or weaker signals into the statistical parametric maps.

The optimal approach depends on the balance between specificity and sensitivity required for the study's objectives. TSPOON should be prioritized when precision, robustness and sharp delineation between tissues are essential, while TWS is more appropriate for broader, exploratory analyses that seek to maximize coverage and detect subtle effects.

In conclusion, this study highlights the complexity of methodological decisions in neuroimaging and the importance of adapting tools to the scientific question at hand, echoing Gauss' 1809 quote [1]. Smoothing, preprocessing and the interpretation of results should always be approached with caution, respecting the specificities of the experimental context and the nature of the data. Statistical significance does not constitute proof of biological truth.

6.2 Perspectives

This study explored the differences between the smoothing methods TWS and TSPOON in the context of qMRI data. However, several aspects remain to be further investigated to better understand the impact of smoothing on the obtained results. In particular, it would be valuable to examine in more detail the distribution of residual values after applying both methods. This could help identify any trends or anomalies that may not be captured by traditional statistical tests, as well as assess the effect of each method on adherence to normality assumptions. A deeper analysis of the residuals could also provide insights into the robustness and sensitivity of the smoothing methods to different scales of signal variation.

In this study, the tissue-specific mask used in TSPOON showed interesting results, but there is still room for improvement in optimizing how these masks are constructed. Testing alternative methods for generating tissue masks for TSPOON could further enhance the method's ability to detect specific brain regions while preserving fine details. For instance, using machine learning techniques to refine mask construction could better capture complex tissue variations and reduce biases in smoothing results.

The findings of this study suggest that TSPOON could offer significant advantages as a smoothing method for analyzing qMRI data. Due to its responsiveness to local gradients, while maintaining heightened sensitivity to fine structures, TSPOON may be particularly suited for contexts where precise detection of small brain structures is crucial. We therefore propose integrating TSPOON as a new smoothing method in the hMRI toolbox, enabling researchers to take advantage of its benefits in future studies. This method could potentially provide better results than traditional techniques under certain conditions, particularly in the study of regions with high tissue heterogeneity. Such an addition would offer users a valuable alternative to meet specific signal analysis needs in neuroimaging.

An interesting perspective for the smoothing methods explored in this study would be to evaluate them on other imaging modalities, such as functional MRI (fMRI), diffusion-weighted imaging (DWI) or positron emission tomography (PET). Functional MRI, which measures variations in brain signal in response to stimuli or cognitive tasks, could benefit from smoothing methods that are more sensitive to local gradients, such as TSPOON, which can better capture subtle brain activations in specific regions. Similarly, DWI, a quantitative imaging modality often used to study microstructural properties of the brain, could leverage advanced smoothing techniques like TSPOON or TWS to improve the accuracy of derived metrics such as those obtained from Neurite Orientation Dispersion and Density Imaging (NODDI) [62]. PET, another quantitative modality, which provides information about metabolic or molecular processes in the brain, might also benefit from tailored smoothing approaches to enhance signal detection and localization of subtle changes in tracer uptake. Testing the applicability of TSPOON and TWS in these contexts would allow for an assessment of their generalizability and potential to adapt to various imaging techniques, while contributing to advances in neuroscience research, particularly in areas such as brain microstructure and metabolic imaging.

Appendix A

Methods: Additional Discussions & Examples

A.1 Discussion on different methods to apply GS

The difference in results between *spm_smooth* and *imgaussfilt3* arises from how each function handles NaN values during convolution. In *spm_smooth*, part of the SPM software suite, NaN values in the input image are treated as zeros before performing the convolution. This behavior is explicitly implemented in the *spm_conv_vol.c* code [63], where lines 22 and 23 ensure that non-finite values such as NaN are replaced with 0.0. As a result, *spm_smooth* minimizes the propagation of NaN values into the smoothed output, allowing meaningful smoothing even in images containing undefined regions.

In contrast, *imgaussfilt3*, a MATLAB function for 3D Gaussian filtering, does not automatically handle NaN values in this way. Instead, NaN values are propagated during the convolution process. This means that if a NaN is present in the vicinity of a voxel being smoothed, the output for that voxel will also be set to NaN, leading to the "absorption" of NaN values and potentially large regions of undefined results in the smoothed output. This difference in handling non-finite values can lead to stark contrasts in the output images, with *imgaussfilt3* producing results that may not be usable in cases where the input contains substantial NaN regions, whereas *spm_smooth* produces more robust outputs in such scenarios.

For example, the same contrast image (con0002) from the first subject of the fMRI dataset [52] [53] using the same processing as the article [55] was used as an example to apply the two implementations of Gaussian smoothing (Figure A.1). We can clearly observe the absorption problem present in the image on the right, smoothed by *imgaussfilt3*.

A.2 TSPOON: Discussion about Handling Division by Zero

The avoidance of division by zero is a critical aspect of this method (Equation 3.3). By setting areas below 5% intensity to zero and subsequently converting them to NaN, the process restricts calculations to valid regions. This ensures that divisions only take place where tissue representation is sufficient, maintaining the mathematical and statistical soundness of the output. The use of NaN prevents propagation of errors and ensures that any subsequent data analysis remains robust.

To reach this avoidance by thresholding at 5%, two different ways can be used:

- *spm_imcalc* which is part of the SPM (Statistical Parametric Mapping) toolbox [51]
- A custom thresholding function with a similar 5% threshold following a similar design than the function which converts 0 to NaN.

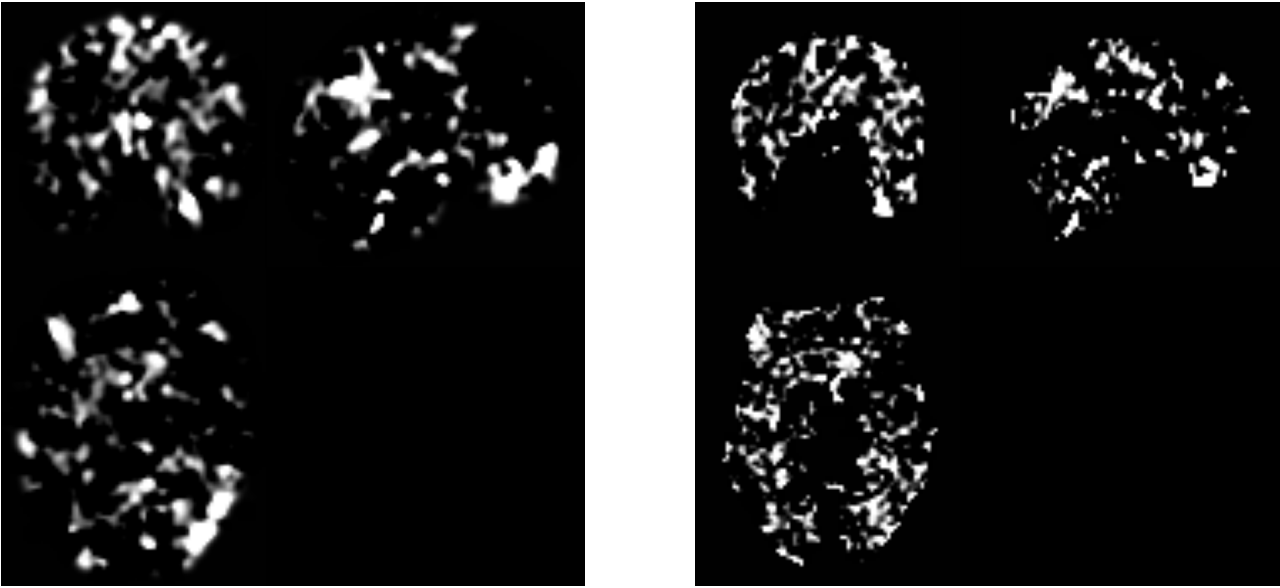


Figure A.1: The image on the right shows the contrast smoothed by *spm_smooth*, while the one on the left is smoothed with *imgaussfilt3*.

Using *spm_imcalc* with a condition like $i1. * (i1 > 0.05)$ is preferable because it combines efficiency, reliability and integration within the SPM framework. It provides a tested, community-backed solution that ensures precision, error handling and ease of use, whereas custom implementations, while potentially more tailored, carry risks related to optimization, error handling and compatibility.

An alternative strategies for managing small values was also considered: Using an intracranial volume (ICV) mask can refine the scope of analysis to relevant brain regions, minimizing the impact of peripheral or negligible values. This solution allows to remove and define as NaN all voxels that were outside of this ICV mask by hypothesizing that all voxels of very low intensity were located outside the brain.

The ICV mask was built on the basis of the average of tissue-specific masks of the entire population. This mpyenne then underwent an isotropic Gaussian smoothing of kernel width $2[mm]$. Finally, a thresholding was carried out at a value of 50% in such a way that the final mask made it possible to identify all the voxels whose probability of being in the middle brain is 50%. Let's insist on the fact that this average brain is defined on the specific population of the database.

However, this solution would have been possible if the initial hypothesis was respected, which is not the case: very low intensities are also present within the mask itself (which is logical since it is a tissue-specific mask).

A.3 Comparison between Jaccard, Dice & Cohen's kappa

To illustrate the difference between Cohen's Kappa, Jaccard Index (JI) and Dice coefficient (DC), two datasets with 10,000 points, all worth zero except for 10 that are worth one in each dataset are considered. However, these 10 points worth one are not in the same place between the two datasets. So the union of the points worth one is null.

For Jaccard Index and Dice coefficient, we have:

$$JI = \frac{|A \cap B|}{|A \cup B|} = \frac{|A \cap B|}{|A| + |B| - |A \cap B|} = \frac{9980}{10000 + 10000 - 9980} = 0.996$$

$$DC = \frac{2 \times |A \cap B|}{|A| + |B|} = \frac{2 \times 9980}{10000 + 10000} = 0.998$$

Both Jaccard and Dice give a high similarity measure because the overlap between the sets is almost complete. For Cohen's Kappa, we calculate the observed agreement (P_o) and the expected agreement by chance (P_e):

$$P_o = \frac{9980}{10000} = 0.998$$

$$P_e = \frac{9990}{10000} \frac{9990}{10000} + \frac{10000 - 9990}{10000} \frac{10000 - 9990}{10000} = \left(\frac{9990}{10000} \right)^2 + \left(\frac{10}{10000} \right)^2$$

$$= \frac{99800100}{10^8} + \frac{100}{10^8} = \frac{998002}{10^6} = 0.998002$$

Cohen's Kappa (κ) is then calculated using:

$$\kappa = \frac{P_o - P_e}{1 - P_e}$$

. Substituting the values:

$$\kappa = \frac{0.998 - 0.998002}{1 - 0.998002} = \frac{-210^{-6}}{1.99810^{-3}} \approx -10^{-3}$$

Thus, Cohen's Kappa in this case is approximately 0. This significant difference highlights how Cohen's Kappa adjusts for the chance agreement, providing a more nuanced measure of agreement than Jaccard and Dice in situations where data distribution is highly imbalanced. Indeed, 0 suggests agreement equivalent to random chance.

Now the same two datasets where all the elements are zero except for 10 elements in each dataset are considered. This time, 5 non-zero elements are overlapping between the two datasets such that their union equals 5. For Jaccard and Dice coefficients, we have:

$$JI = \frac{|A \cap B|}{|A \cup B|} = \frac{|A \cap B|}{|A| + |B| - |A \cap B|} = \frac{9990}{10000 + 10000 - 9990} = 0.997$$

$$DC = \frac{2 \times |A \cap B|}{|A| + |B|} = \frac{2 \times 9990}{10000 + 10000} = 0.999$$

For Cohen's Kappa, we calculate the observed agreement (P_o) and the expected agreement by chance (P_e):

$$P_o = \frac{9990}{10000} = 0.999$$

$$P_e = \frac{9990}{10000} \frac{9990}{10000} + \frac{10000 - 9990}{10000} \frac{10000 - 9990}{10000} = \left(\frac{9990}{10000} \right)^2 + \left(\frac{10}{10000} \right)^2$$

$$= \frac{99800100}{10^8} + \frac{100}{10^8} = \frac{998002}{10^6} = 0.998002$$

Cohen's Kappa (κ) is then calculated using:

$$\kappa = \frac{P_o - P_e}{1 - P_e}$$

. Substituting the values:

$$\kappa = \frac{0.999 - 0.998002}{1 - 0.998002} = \frac{9.9810^{-4}}{1.99810^{-3}} \approx 0.4995$$

Thus, Cohen's Kappa in this case is approximately 0.5 suggesting an average agreement between the two datasets while Jaccard and Dice always show a very good agreement. We can see that, for the same expected agreement, the closer the observed agreement is to one, the higher the Cohen's Kappa.

Finally, it is generally true that the Dice coefficient is higher than the Jaccard index for the same two sets. This is due to the way the two metrics are calculated. Let's recall the formulas for both:

- **Jaccard Index** is defined as:

$$JI(A, B) = \frac{|A \cap B|}{|A \cup B|}$$

- **Dice Coefficient** is defined as:

$$DC(A, B) = \frac{2|A \cap B|}{|A| + |B|}$$

The Dice coefficient is essentially a harmonic mean of the two sets' proportions and places more emphasis on the intersection. When you simplify the relationship between the two, you find that:

$$DC(A, B) = \frac{2JI(A, B)}{1 + JI(A, B)}$$

This formula shows that the Dice coefficient is always equal to or greater than the Jaccard index because the factor of 2 in the numerator of the Dice coefficient's formula increases its value relative to the Jaccard index. To put it simply, for the same sets A and B , the Dice coefficient will generally yield a higher similarity score than the Jaccard index.

A.4 Additional Information: One-Sample T-Test & F-Test

This section describes the one-sample t-test model and F-test to assess difference between the smoothed maps in more detail.

A.4.1 One-Sample T-Test Pipeline

The one-sample t-test is used to determine whether a sample mean differs significantly from a hypothesized value. Indeed, the basic result of a one-sample t-test is a statistical evaluation that answers the following question: *Is the mean of the data significantly different from zero?* In a one-sample t-test, the objective is to test whether the mean of a dataset (the observed values) is statistically different from a null hypothesis fixed at zero. The provided data typically represent differences (e.g. TWS - TSPOON MPMs here) or values from a single condition. Thus, to apply this test, the null hypothesis must be assumed: the mean of the data is equal to zero ($\mu = 0$). However, there is an alternative hypothesis that is the mean of the data is different from zero ($\mu \neq 0$).

The t-statistic is calculated as follows:

$$t = \frac{\bar{x} - \mu_0}{s/\sqrt{n}}$$

where:

- \bar{x} = mean of the observed data.

- μ_0 = null hypothesis (typically 0).
- s = standard deviation of the data.
- n = number of data points.

The test results provide a value of t , which indicates how many standard deviations the observed mean (\bar{x}) deviates from the null hypothesis ($\mu_0 = 0$) and a p-value, which is a probability associated with the t-statistic, which measures the likelihood of observing a difference as extreme (or more extreme) than \bar{x} , under H_0 . If $p < \alpha$ (typically $\alpha = 0.05$), we reject H_0 , concluding that the mean is significantly different from zero. In our case, the provided data are the difference MPMs calculated as TWS_MPMs - TSPOON_MPMs. The null Hypothesis (H_0) is applied in such a way that the mean of the differences TWS_MPMs - TSPOON_MPMs is 0.

A.4.2 F-Test Pipeline

An F-test is often used to compare multiple models or assess the effect of multiple covariates. In our case, the F-test will be based on the intercept resulting from the estimation of the one-sample t-test model.

To perform an F-test within the context of a one-sample t-test [51] and verify whether the mean of the data is significantly different from zero, independently of covariates (age, sex, TIV, scanner), F-contrast has to test the overall effect while controlling for these covariates over the population. The objective is to test whether the main effect (the difference between TWS and TSPOON) is significantly different from zero while controlling for covariates. In other words, you want to test whether the difference between TWS and TSPOON exists independently of variations related to age, sex, TIV and scanner.

In the context of your model, the design matrix (X) looks like this:

$$X = \begin{bmatrix} 1 & \text{age}_1 & \text{sex}_1 & \text{TIV}_1 & \text{scanner}_1 \\ 1 & \text{age}_2 & \text{sex}_2 & \text{TIV}_2 & \text{scanner}_2 \\ \vdots & \vdots & \vdots & \vdots & \vdots \\ 1 & \text{age}_n & \text{sex}_n & \text{TIV}_n & \text{scanner}_n \end{bmatrix}$$

where:

- The first column represents the intercept (which is 1 for each subject, corresponding to the mean of the differences TWS - TSPOON).
- The other columns represent the covariates (age, sex, TIV, scanner).

The idea is to test whether the intercept is significantly different from zero while controlling for the effects of the covariates. This is done by specifying an F-contrast where only the columns associated with the intercept are tested against zero, while the covariates' effects are controlled (ignored in the test).

The F-contrast matrix to test the effect of the intercept independently of the covariates looks like this:

$$F = \begin{bmatrix} 1 & 0 & 0 & 0 & 0 \\ 0 & 0 & 0 & 0 & 0 \\ 0 & 0 & 0 & 0 & 0 \\ 0 & 0 & 0 & 0 & 0 \end{bmatrix}$$

where:

- The first row [1, 0, 0, 0, 0] corresponds to the intercept (the difference TWS - TSPOON).

- The other rows are zero, as we do not need to test the covariates directly in this contrast.

In other words, this contrast tests whether the mean of the difference MPMs between TWS and TSPOON is significantly different from zero after controlling for the effects of the covariates.

Appendix B

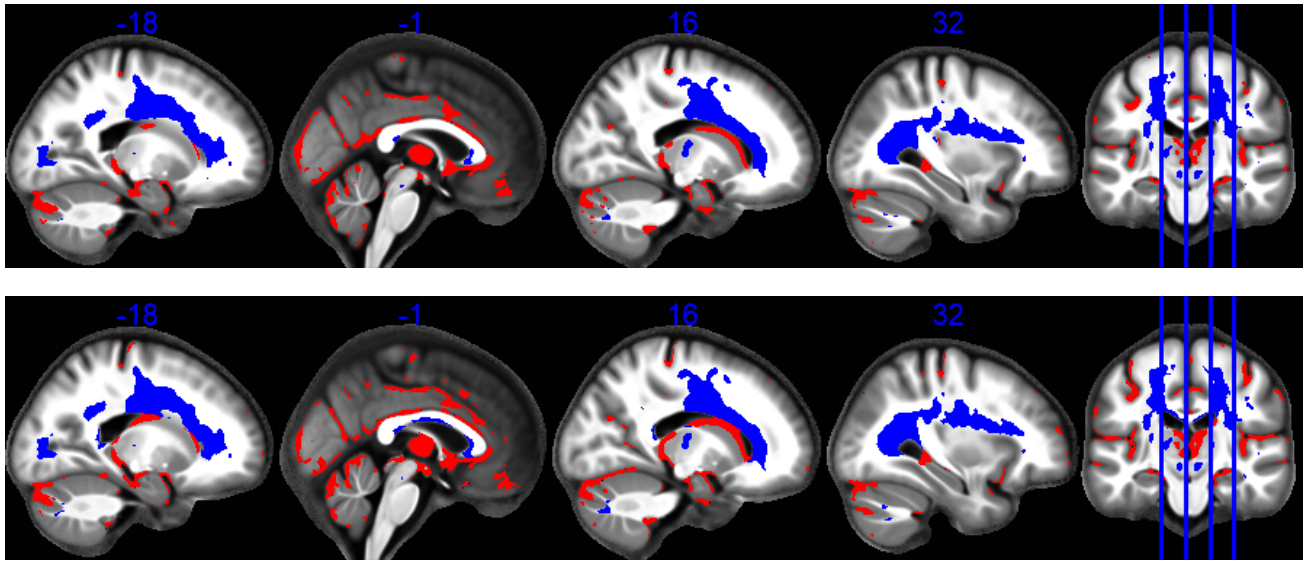
Additional qMRI Results

B.1 Comparing Results

This section presents the additional results that are also presented in the article [2].

The result displayed in Figure B.3 shows the regions where the qMRI parameter $R2^*$ significantly decreases with age, thus according to the AR- contrast. This result is well represented in the article as well, but this effect is not the one included in Table 4.1 for the qMRI parameter $R2^*$. Indeed, as explained in the article [2], a large region is observed where $R2^*$ significantly decreases with age. However, we observe many more regions where it increases than where it decreases. For reference, this parameter would be related to the amount of iron for each voxel.

Figure B.4 shows regions where the qMRI PD parameter decreases with age, but this diminishing effect was not included in this master's thesis in light of the discussion in the article [2] and is therefore not included in Table 4.1. However, it is interesting and not negligible that age can have a diminishing effect on the qMRI PD parameter in certain regions of the brain. However, from the perspective that interests us in this master's thesis, the observations between the significant regions from TWS and TSPOON remain similar to those made in the results section.



The four sagittal slices are located at $z = -18, -1, 16$ and 32 mm, from left to right, as illustrated on the coronal slice (right).

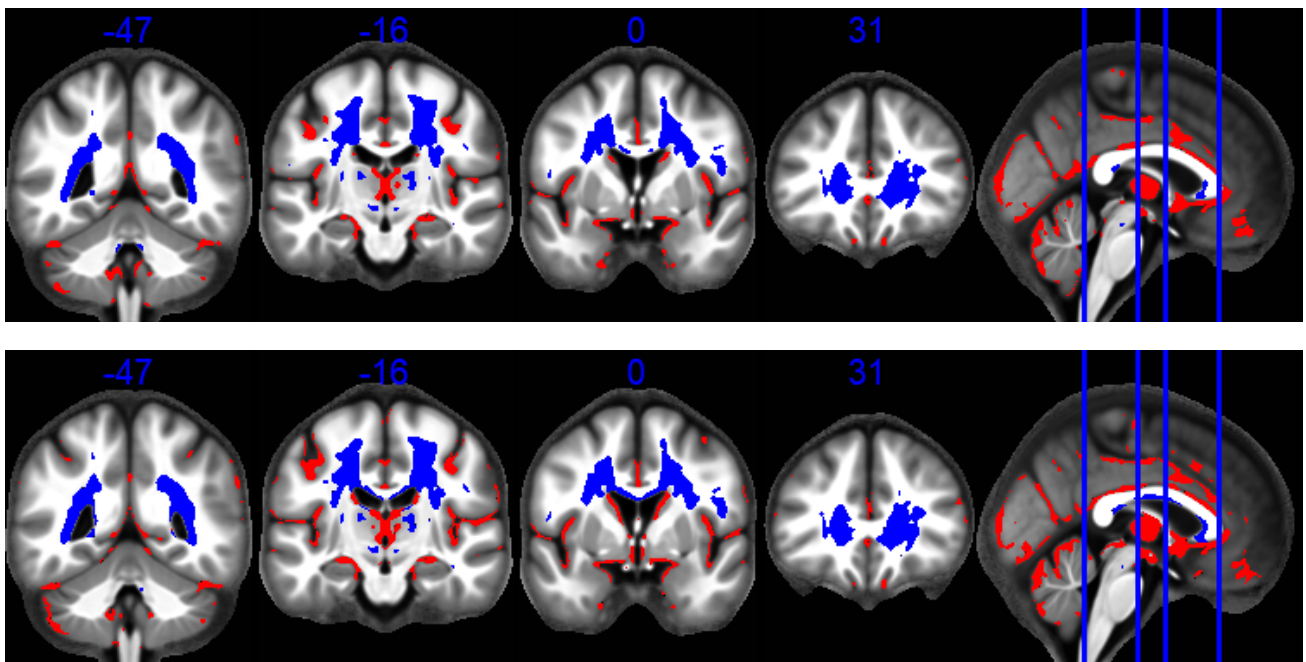
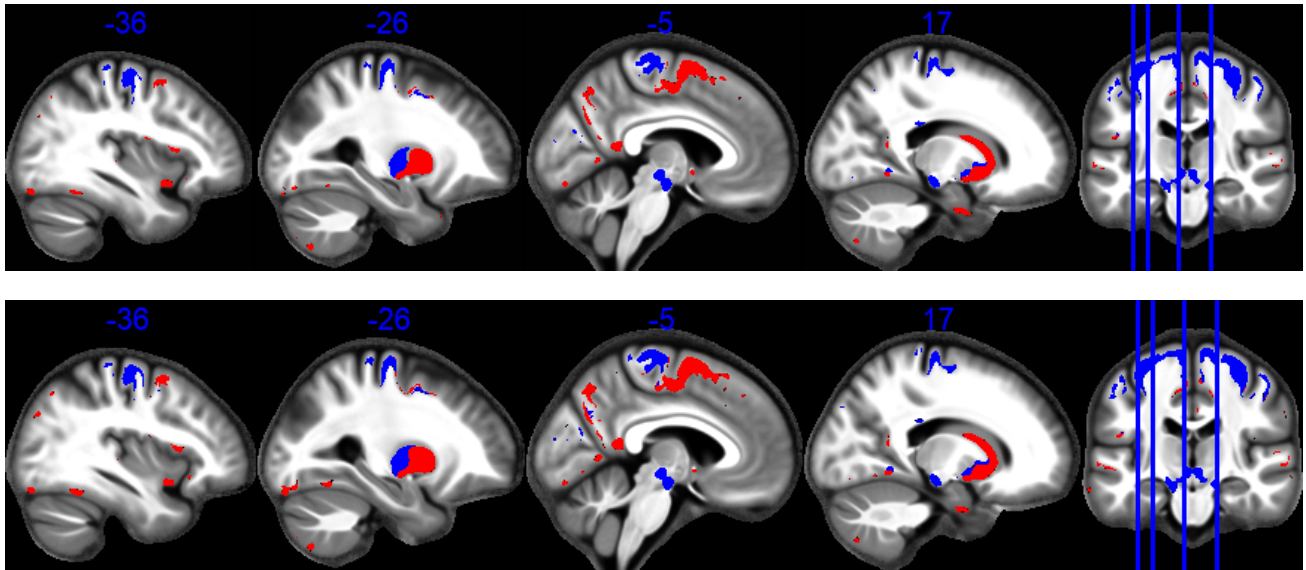


Figure B.1: Statistical parametric maps identifying regions (red for GM and blue for WM) in which MTsat significantly decreased (AR-) with age at the $p < 0.05$ FWE corrected level. The results are superimposed on the mean MT map for the cohort in MNI space. The four coronal slices are located at $z = -47, -16, 0$ and 31 mm, from left to right, as illustrated on the sagittal slice (right). The top row shows results obtained from TSPOON, while the bottom row, the TWS ones.



The four sagittal slices are located at $z = -36, -26, -5$ and 17 mm, from left to right, as illustrated on the coronal slice (right).

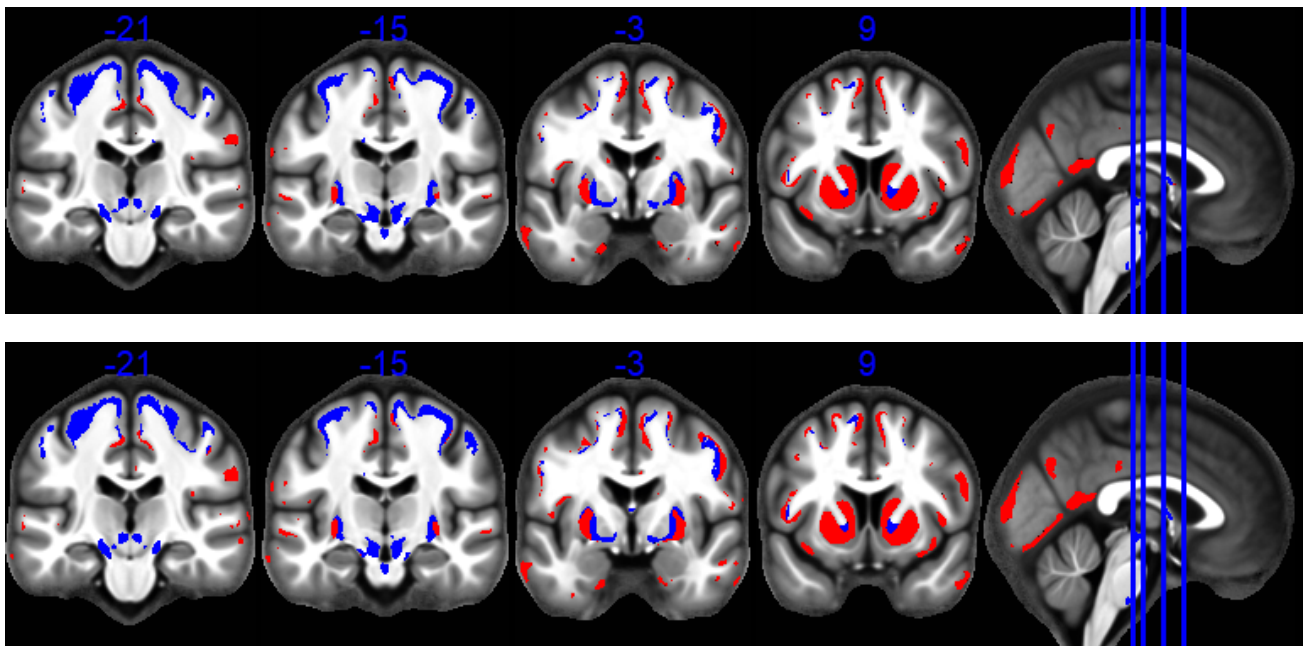


Figure B.2: Statistical parametric maps identifying regions (red for GM and blue for WM) in which $R2^*$ significantly increased (AR+) with age at the $p < 0.05$ FWE corrected level. The results are superimposed on the mean MT map for the cohort in MNI space. The four coronal slices are located at $z = -21, -15, -3$ and 9 mm, from left to right, as illustrated on the sagittal slice (right). The top row shows results obtained from TSPOON, while the bottom row, the TWS ones.

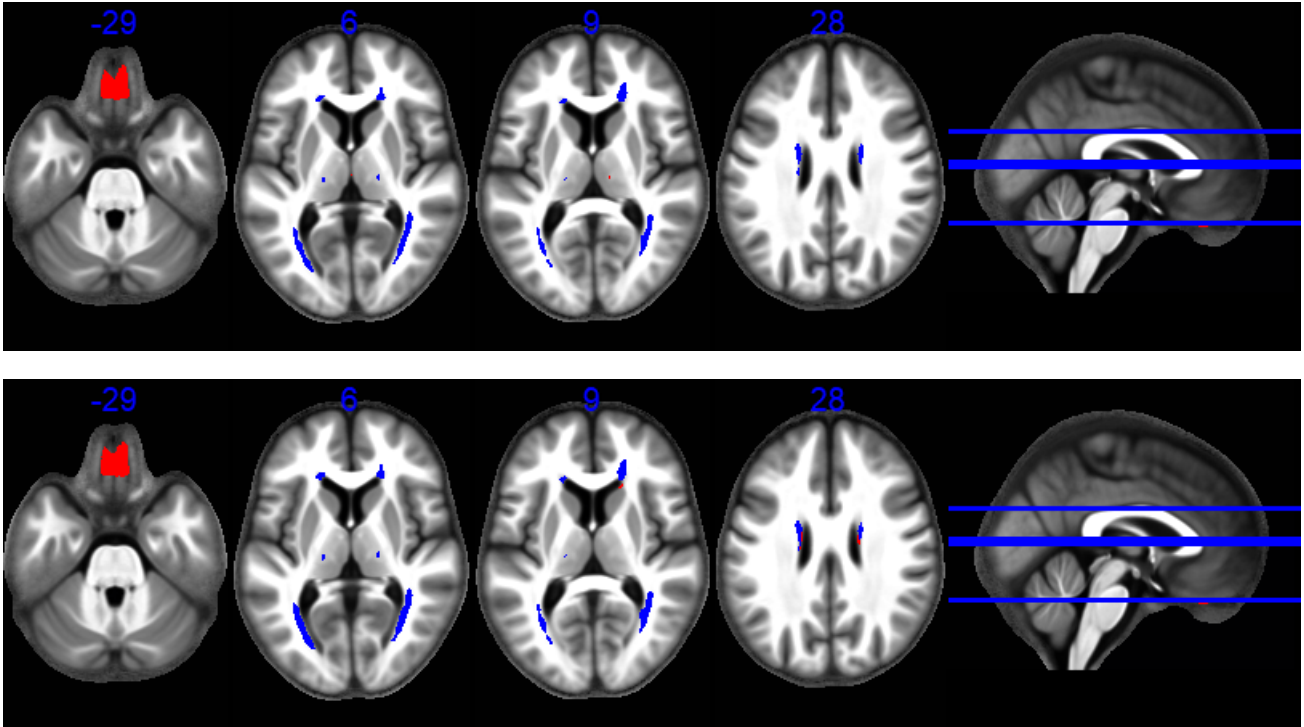


Figure B.3: Statistical parametric maps identifying regions (red for GM and blue for WM) in which $R2^*$ significantly decreased (AR-) with age at the $p < 0.05$ FWE corrected level. The results are superimposed on the mean MT map for the cohort in MNI space. The four axial slices are located at $z = -29, 6, 9$ and 28 mm, from left to right, as illustrated on the sagittal slice (right). The top row shows results obtained from TSPOON, while the bottom row, the TWS ones.

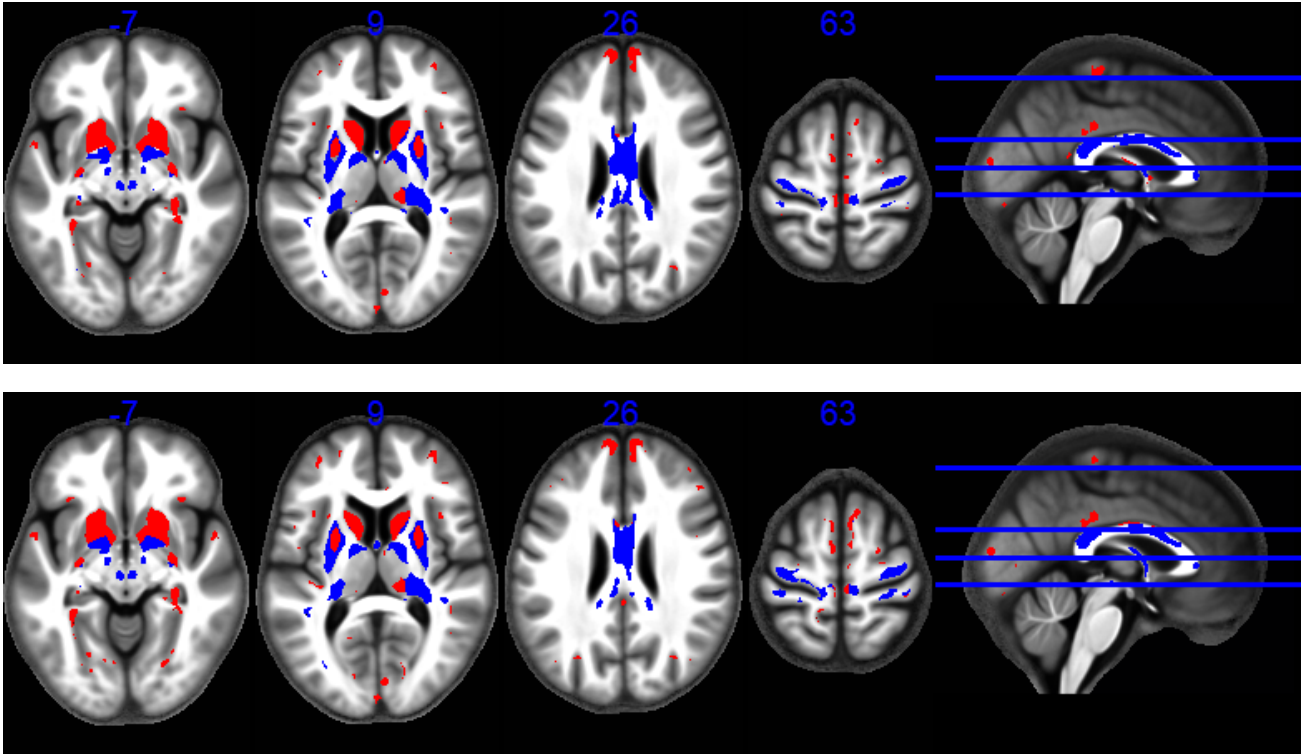


Figure B.4: Statistical parametric maps identifying regions (red for GM and blue for WM) in which PD significantly decreased (AR-) with age at the $p < 0.05$ FWE corrected level. The results are superimposed on the mean MT map for the cohort in MNI space. The four axial slices are located at $z = -7, 9, 26$ and 63 mm, from left to right, as illustrated on the sagittal slice (right). The top row shows results obtained from TSPOON, while the bottom row, the TWS ones.

B.2 Effective Smoothing

qMRI Parameter	Tissue Class	x [mm]	y [mm]	z [mm]
MTsat	GM	6.0011	5.3459	5.4897
	WM	7.7054	7.8464	7.7715
PD	GM	6.6994	6.2947	6.4081
	WM	6.4695	6.5924	6.0944
R1	GM	6.4700	5.8291	5.9162
	WM	8.7759	8.8105	8.4637
R2*	GM	6.3234	6.0499	5.9712
	WM	8.5275	8.0661	7.6273

TWS effective smoothing

qMRI Parameter	Tissue Class	x [mm]	y [mm]	z [mm]
MTsat	GM	5.7264	5.0756	5.2033
	WM	7.2763	7.4156	7.3417
PD	GM	6.5186	6.0490	6.1221
	WM	6.2726	6.4238	5.9428
R1	GM	6.2338	5.5720	5.6421
	WM	8.3697	8.4288	8.0987
R2*	GM	6.2278	5.9066	5.8114
	WM	8.4574	8.0408	7.5698

TSPOON effective smoothing

Table B.1: FWHM for TWS and TSPOON indicating the effective smoothing applied to the contrast images. These values are the same for all contrasts (AR+, AR- and AR) for each combination of qMRI parameter and tissue class.

B.3 Similarity Metrics

	Jaccard	Dice	CohenKappa
MTsat_GM_T1	0.72222	0.83871	0.83871
MTsat_GM_T2	0.59994	0.74995	0.74786
MTsat_GM_F3	0.59117	0.74306	0.74116
MTsat_WM_T1	0.63249	0.77488	0.77486
MTsat_WM_T2	0.88199	0.9373	0.93666
MTsat_WM_F3	0.87124	0.93119	0.93057
PDmap_GM_T1	0.29595	0.45673	0.45669
PDmap_GM_T2	0.69691	0.82139	0.82073
PDmap_GM_F3	0.69814	0.82224	0.82165
PDmap_WM_T1	0.89339	0.94369	0.94353
PDmap_WM_T2	0.80304	0.89076	0.89033
PDmap_WM_F3	0.83828	0.91203	0.91148
R1map_GM_T1	0.6009	0.7507	0.75063
R1map_GM_T2	0.40337	0.57486	0.57437
R1map_GM_F3	0.41771	0.58927	0.58877
R1map_WM_T1	0.75472	0.86022	0.86019
R1map_WM_T2	0.81251	0.89656	0.89633
R1map_WM_F3	0.8056	0.89234	0.89212
R2starmap_GM_T1	0.73129	0.84479	0.84397
R2starmap_GM_T2	0.63973	0.78029	0.78025
R2starmap_GM_F3	0.73355	0.8463	0.84557
R2starmap_WM_T1	0.75579	0.86091	0.86051
R2starmap_WM_T2	0.83657	0.91101	0.91097
R2starmap_WM_F3	0.75934	0.86321	0.86282

Figure B.5: Jaccard index, Dice coefficient and Cohen's kappa between the significant regions ($p < 0.05$ FWE corrected level) derived from the corresponding contrast maps (AR+ called T1, AR- called T2 and AR called F3) of TWS and TSPOON for each combination of a qMRI parameter and a tissue class.

We observe in Figure B.6 that each tissue class presents the same Jaccard index, Dice coefficient, or Cohen's kappa between the corresponding smoothed TWS and TSPOON images, regardless of the contrast map or the qMRI parameter. This result is normal since these smoothed images are defined by the denominators of the TWS and TSPOON smoothing functions in Section 3.2.3.

	Jaccard	Dice	CohenKappa
MTsat_GM_T1	0.95559	0.97729	0.97371
MTsat_WM_T1	0.95343	0.97616	0.97415
PDmap_GM_T1	0.95559	0.97729	0.97371
PDmap_WM_T1	0.95343	0.97616	0.97415
R1map_GM_T1	0.95559	0.97729	0.97371
R1map_WM_T1	0.95343	0.97616	0.97415
R2starmap_GM_T1	0.95559	0.97729	0.97371
R2starmap_WM_T1	0.95343	0.97616	0.97415
MTsat_GM_T2	0.95559	0.97729	0.97371
MTsat_WM_T2	0.95343	0.97616	0.97415
PDmap_GM_T2	0.95559	0.97729	0.97371
PDmap_WM_T2	0.95343	0.97616	0.97415
R1map_GM_T2	0.95559	0.97729	0.97371
R1map_WM_T2	0.95343	0.97616	0.97415
R2starmap_GM_T2	0.95559	0.97729	0.97371
R2starmap_WM_T2	0.95343	0.97616	0.97415
MTsat_GM_F3	0.95559	0.97729	0.97371
MTsat_WM_F3	0.95343	0.97616	0.97415
PDmap_GM_F3	0.95559	0.97729	0.97371
PDmap_WM_F3	0.95343	0.97616	0.97415
R1map_GM_F3	0.95559	0.97729	0.97371
R1map_WM_F3	0.95343	0.97616	0.97415
R2starmap_GM_F3	0.95559	0.97729	0.97371
R2starmap_WM_F3	0.95343	0.97616	0.97415

Figure B.6: Jaccard index, Dice coefficient and Cohen's kappa between TWS and TSPOON for each contrast maps (AR+ called T1, AR- called T2 and AR called F3) of a combination of a qMRI parameter and a tissue class.

B.4 Threshold Scatter Plot

As reminder, scatter plots representing the different possible combinations of qMRI parameters and tissue class. The coordinates of these points represent the threshold above which a voxel will be considered significant depending on the smoothing method (hMRI_TWS and generalized TSPOON here). In the order of position starting from the origin of the graph: R1-WM, R2*-WM MT-WM, PD-WM, PD-GM, R2*-GM, R1-GM, MTsat-GM and the order is the same for AR+, AR- and AR.

As we can see, the scatter plot of AR- in Figure B.7 is exactly the same than the one of AR+ in Figure 4.10. While the scatter plot of AR in Figure B.8 has a similar appearance than the both previous ones of AR+ and AR- but the thresholding values are larger as we can see in the Table B.2.

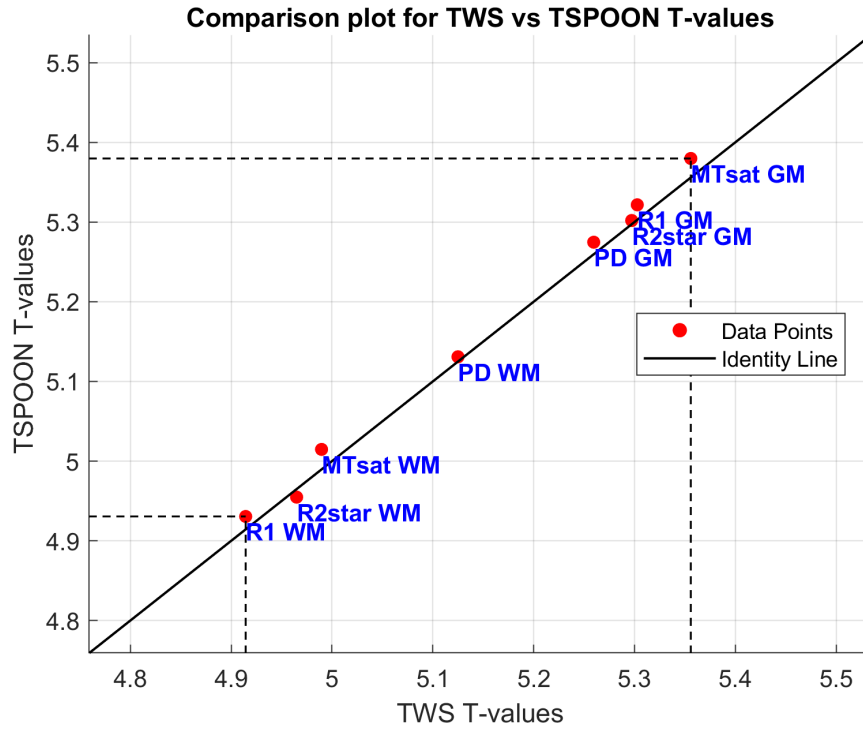


Figure B.7: Scatter plot of AR- representing the different possible combinations of qMRI parameters and tissue class. The coordinates of these points represent the threshold above which a voxel will be considered significant depending on the smoothing method (TWS and TSPOON here). In the order of position starting from the origin of the graph: R1-WM, R2*-WM MTsat-WM, PD-WM, PD-GM, R2*-GM, R1-GM, MTsat-GM and the order is the same for AR+, AR- and AR.

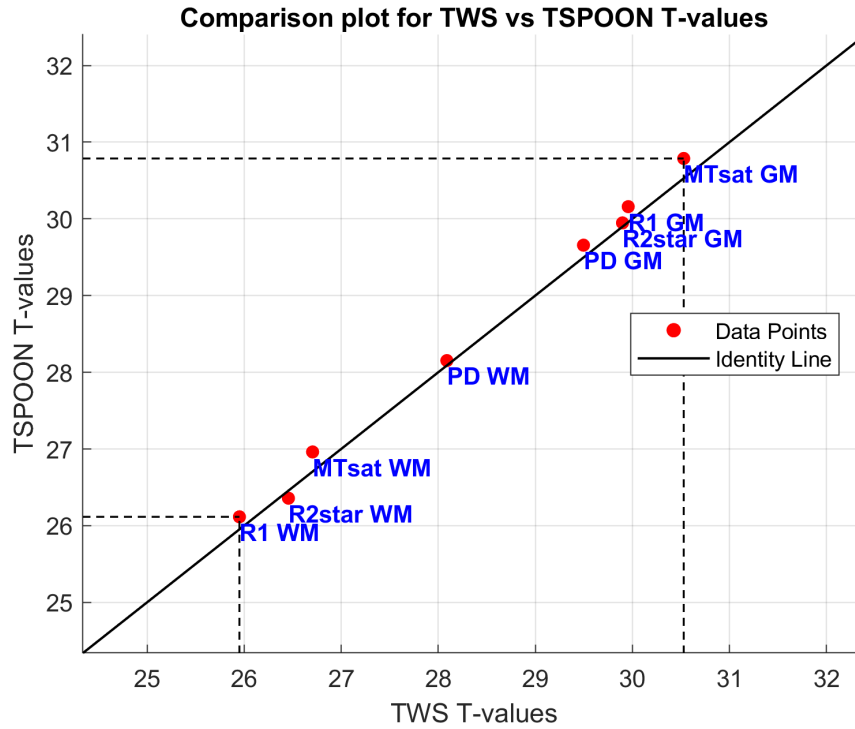


Figure B.8: Scatter plot of AR representing the different possible combinations of qMRI parameters and tissue class. The coordinates of these points represent the threshold above which a voxel will be considered significant depending on the smoothing method (TWS and TSPOON here). In the order of position starting from the origin of the graph: R1-WM, R2*-WM MTsat-WM, PD-WM, PD-GM, R2*-GM, R1-GM, MTsat-GM and the order is the same for AR+, AR- and AR.

TWS	GM	WM
MTsat	30.5289	26.7056
PD	29.4964	28.0887
R1	29.9571	25.9521
R2*	29.8982	26.4570

TSPOON	GM	WM
MTsat	30.7873	26.9617
PD	29.6572	28.1524
R1	30.1593	26.1157
R2*	29.9477	26.3581

Table B.2: F-value threshold at $p < 0.05$ FWE corrected level for TWS (left) and TSPOON (right) for AR.

B.5 Brain 1D: merged signals

Through Figures B.9 B.10 and B.11, we observe that the hypothesis made regarding the direction of the peak around 175 mm depends on the MNI signal, knowing that the TWS signal is ahead of the TSPOON signal, as evidenced by the PD parameter (Figure B.10) where it is the TSPOON signal that shows a downward peak while the TWS signal shows an upward one. Moreover, it can also be observed that during a transition from a non-considered tissue class (here CSF) to a considered one (here GM), the TSPOON signal always starts faster than the TWS signal.

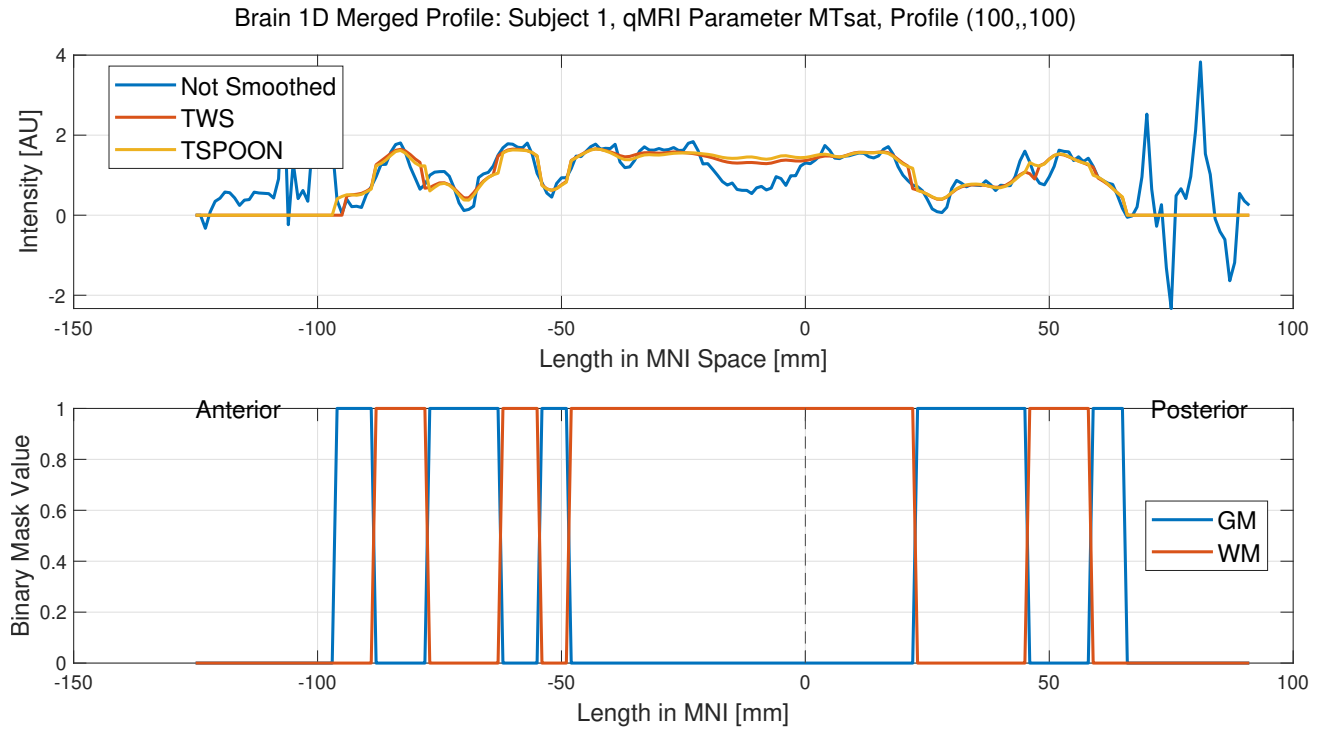


Figure B.9: Brain 1D Profile for MTsat parameter: TWS and TSPOON smoothed and merged signals.

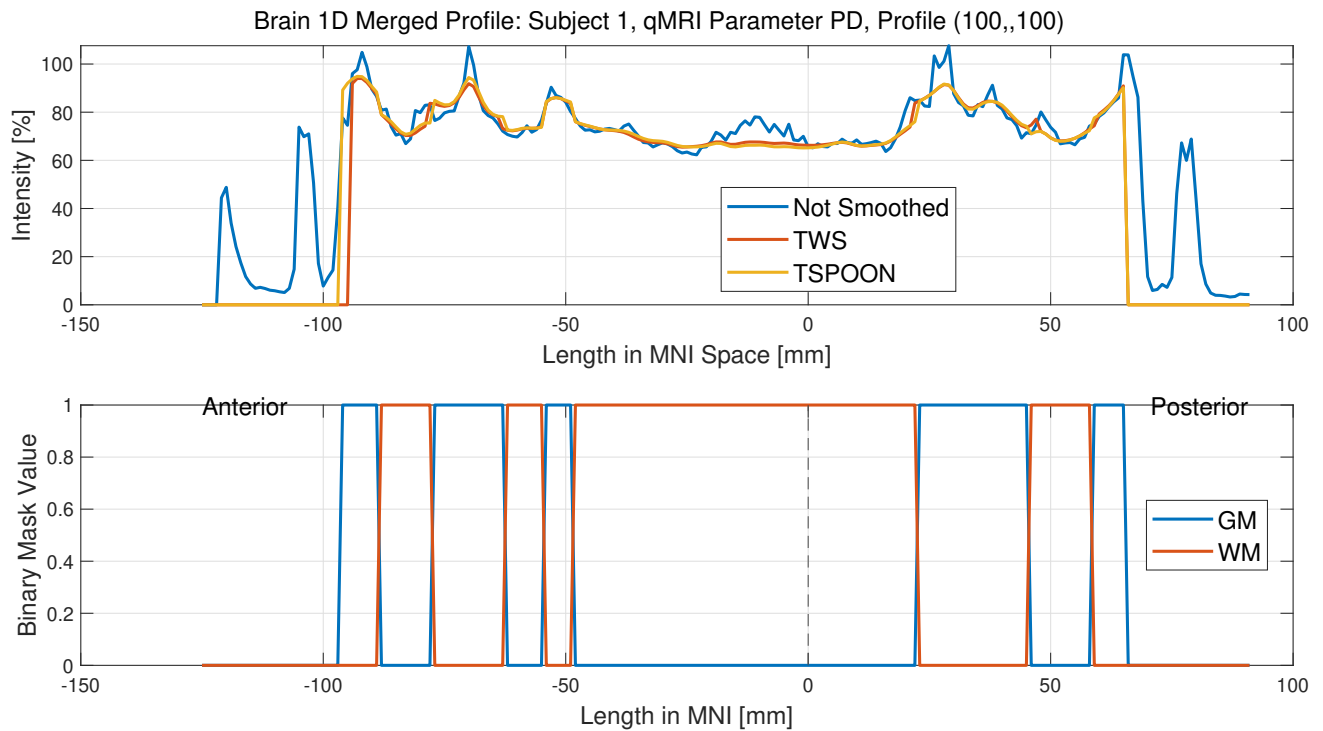


Figure B.10: Brain 1D Profile for PD parameter: TWS and TSPOON smoothed and merged signals.

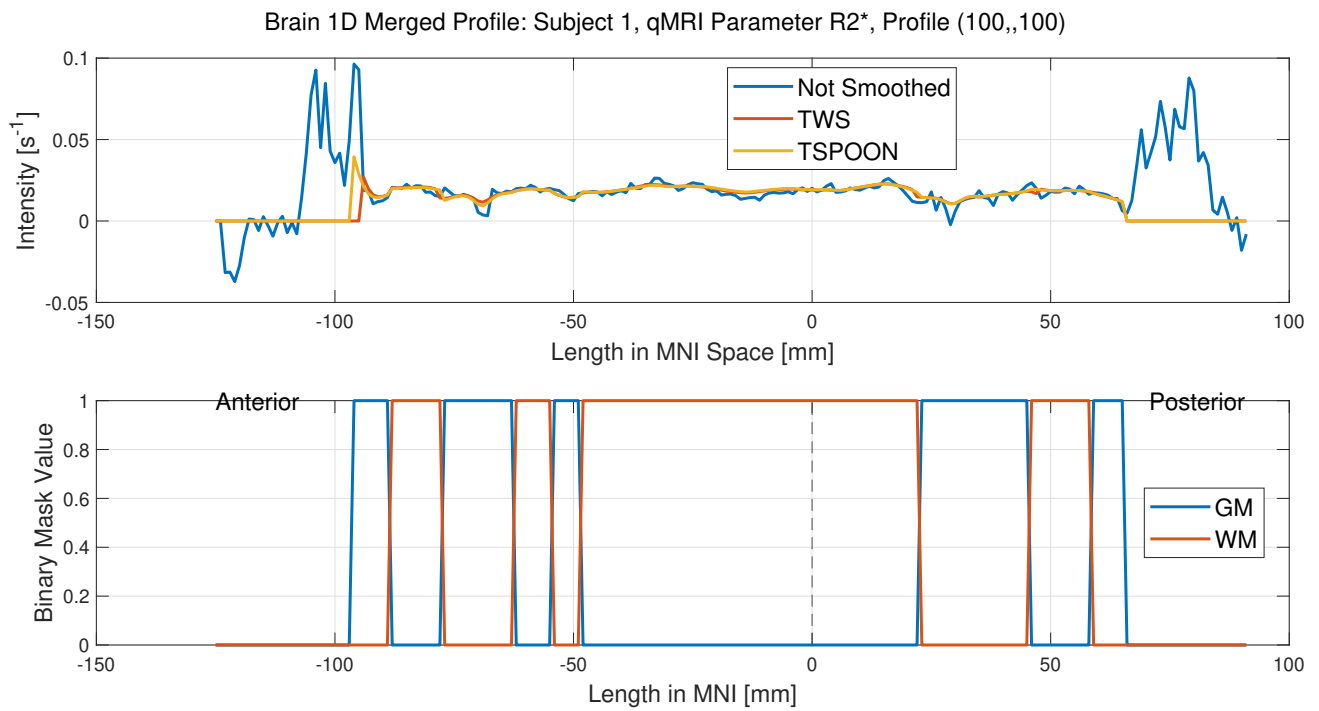
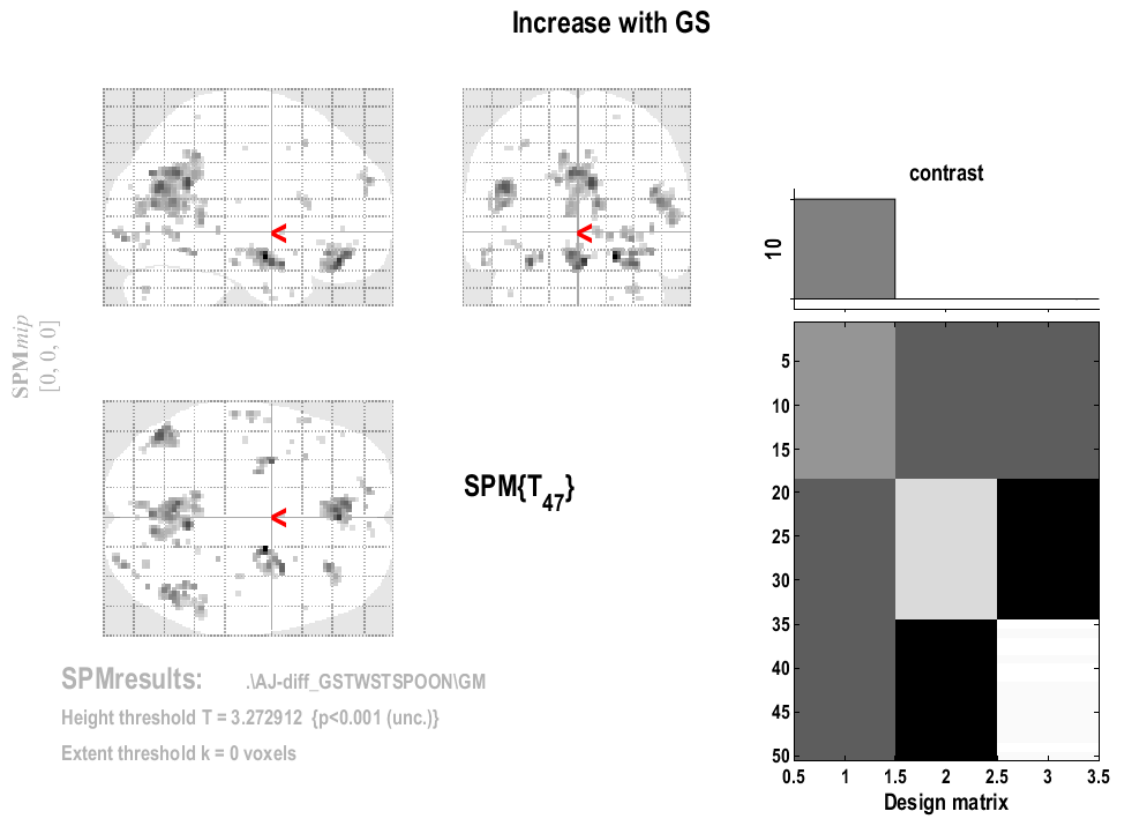


Figure B.11: Brain 1D Profile for R2star parameter: TWS and TSPOON smoothed and merged signals.

Appendix C

Additional fMRI Results

The Figures C.1 C.5 C.3 C.2 C.6 and C.4 present the other significant results from the contrast statistical parametric maps obtained after the application of the GLM (Section 3.4) on the statistical parametric map *Faces > Scrambled Faces*. Significant results are observed at the $p < 0.001$ uncorrected level for regions of the statistical parametric map *Faces > Scrambled Faces* that significantly increase through the three smoothing methods, both in gray matter and white matter.



Statistics: p -values adjusted for search volume

set-level		cluster-level				peak-level					mm mm mm		
p	c	$p_{FWE-corr}$	$q_{FDR-corr}$	k_E	p_{uncorr}	$p_{FWE-corr}$	$q_{FDR-corr}$	T	(Z_E)	p_{uncorr}			
0.000	57	0.001	0.000	71	0.000	0.000	0.000	8.63	6.65	0.000	20	-6	-16
						0.004	0.004	6.13	5.23	0.000	32	4	-20
						0.060	0.023	5.36	4.71	0.000	30	-4	-18
		0.000	0.000	138	0.000	0.000	0.001	7.16	5.86	0.000	2	38	-18
						0.004	0.004	6.16	5.25	0.000	-6	42	-14
						0.995	0.331	3.91	3.62	0.000	0	32	-10
		0.000	0.000	244	0.000	0.001	0.002	6.66	5.56	0.000	6	-52	26
						0.003	0.004	6.20	5.28	0.000	-6	-58	32
						0.014	0.010	5.78	5.00	0.000	0	-74	32
		0.000	0.000	139	0.000	0.001	0.004	6.43	5.42	0.000	-46	-68	24
						0.077	0.026	5.28	4.66	0.000	-46	-62	14
						0.995	0.331	3.91	3.62	0.000	-46	-58	24
		0.009	0.003	45	0.000	0.002	0.004	6.33	5.36	0.000	-30	-2	-20
						0.198	0.051	5.00	4.46	0.000	-24	-10	-16
		0.048	0.012	31	0.002	0.024	0.014	5.62	4.89	0.000	30	32	-14
		0.029	0.010	35	0.001	0.026	0.014	5.60	4.88	0.000	10	-72	14
		0.000	0.000	86	0.000	0.027	0.014	5.59	4.87	0.000	46	-60	16
						0.039	0.017	5.48	4.80	0.000	44	-66	22
						0.999	0.425	3.79	3.52	0.000	50	-48	18
		0.661	0.172	11	0.045	0.100	0.031	5.20	4.60	0.000	30	-90	-6

table shows 3 local maxima more than 8.0mm apart

Height threshold: $T = 3.27$, $p = 0.001$ (1.000)

Extent threshold: $k = 0$ voxels

Expected voxels per cluster, $\langle k \rangle = 2.683$

Expected number of clusters, $\langle c \rangle = 23.95$

FWEp: 5.407, FDRp: 5.052, FWEc: 31, FDRc: 20

Degrees of freedom = [1.0, 47.0]

FWHM = 5.9 5.6 6.5 mm mm mm; 2.9 2.8 3.2 {voxels}

Volume: 381008 = 47626 voxels = 778.7 resels

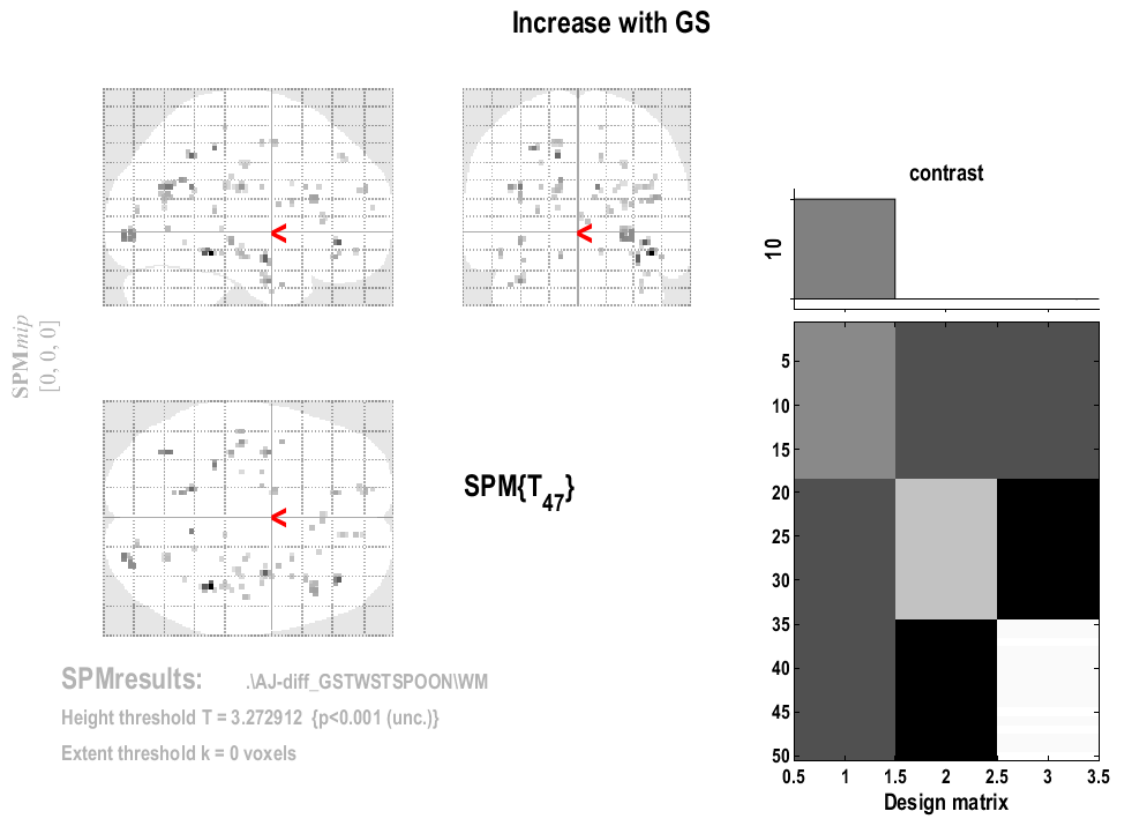
Voxel size: 2.0 2.0 2.0 mm mm mm; (resel = 26.46 voxels)

Page 1

< >

1

Figure C.1: Statistical parametric map showing regions where the contrast map *Faces > Scrambled Faces* is significantly increased by gaussian smoothing in GM, at the $p < 0.001$ uncorrected level.



Statistics: p -values adjusted for search volume

set-level		cluster-level				peak-level					mm mm mm		
p	c	$p_{\text{FWE-corr}}$	$q_{\text{FDR-corr}}$	k_E	p_{uncorr}	$p_{\text{FWE-corr}}$	$q_{\text{FDR-corr}}$	T	(Z_E)	p_{uncorr}			
0.000	59	0.564	0.364	8	0.031	0.007	0.052	5.92	5.09	0.000	42	-38	-14
		0.782	0.364	6	0.056	0.317	0.386	4.80	4.31	0.000	38	38	-8
		0.673	0.364	7	0.041	0.372	0.386	4.76	4.28	0.000	34	-6	-16
		0.951	0.364	4	0.111	0.549	0.427	4.64	4.19	0.000	-14	-50	42
		0.782	0.364	6	0.056	0.796	0.511	4.44	4.04	0.000	-36	-64	24
		0.951	0.364	4	0.111	0.820	0.511	4.41	4.01	0.000	-28	-36	46
		0.101	0.233	16	0.004	0.847	0.511	4.38	3.99	0.000	24	-90	-4
		1.000	0.418	1	0.418	0.862	0.511	4.36	3.97	0.000	10	-50	24
		0.378	0.364	10	0.017	0.957	0.610	4.18	3.83	0.000	-36	-4	-30
		0.999	0.418	2	0.251	0.981	0.698	4.09	3.77	0.000	-12	-56	28
		0.880	0.364	5	0.078	0.985	0.698	4.07	3.74	0.000	-42	-20	24
		0.564	0.364	8	0.031	0.994	0.787	3.99	3.68	0.000	44	24	18
		0.951	0.364	4	0.111	0.996	0.787	3.97	3.66	0.000	-36	-26	-8
		0.988	0.418	3	0.163	0.997	0.805	3.93	3.64	0.000	-12	36	-16
		0.673	0.364	7	0.041	0.999	0.808	3.87	3.59	0.000	-36	-64	20
		1.000	0.418	1	0.418	1.000	0.808	3.82	3.55	0.000	-42	4	-32
		0.951	0.364	4	0.111	1.000	0.808	3.79	3.52	0.000	-48	-20	-14
		0.782	0.364	6	0.056	1.000	0.808	3.78	3.51	0.000	-14	54	22
		0.880	0.364	5	0.078	1.000	0.808	3.77	3.50	0.000	-14	0	50
		1.000	0.418	1	0.418	1.000	0.808	3.73	3.48	0.000	-12	-60	26

table shows 3 local maxima more than 8.0mm apart

Height threshold: $T = 3.27$, $p = 0.001$ (1.000)
 Extent threshold: $k = 0$ voxels
 Expected voxels per cluster, $\langle k \rangle = 1.633$
 Expected number of clusters, $\langle c \rangle = 27.13$
 FWEp: 5.349, FDRp: Inf, FWEc: Inf, FDRc: Inf

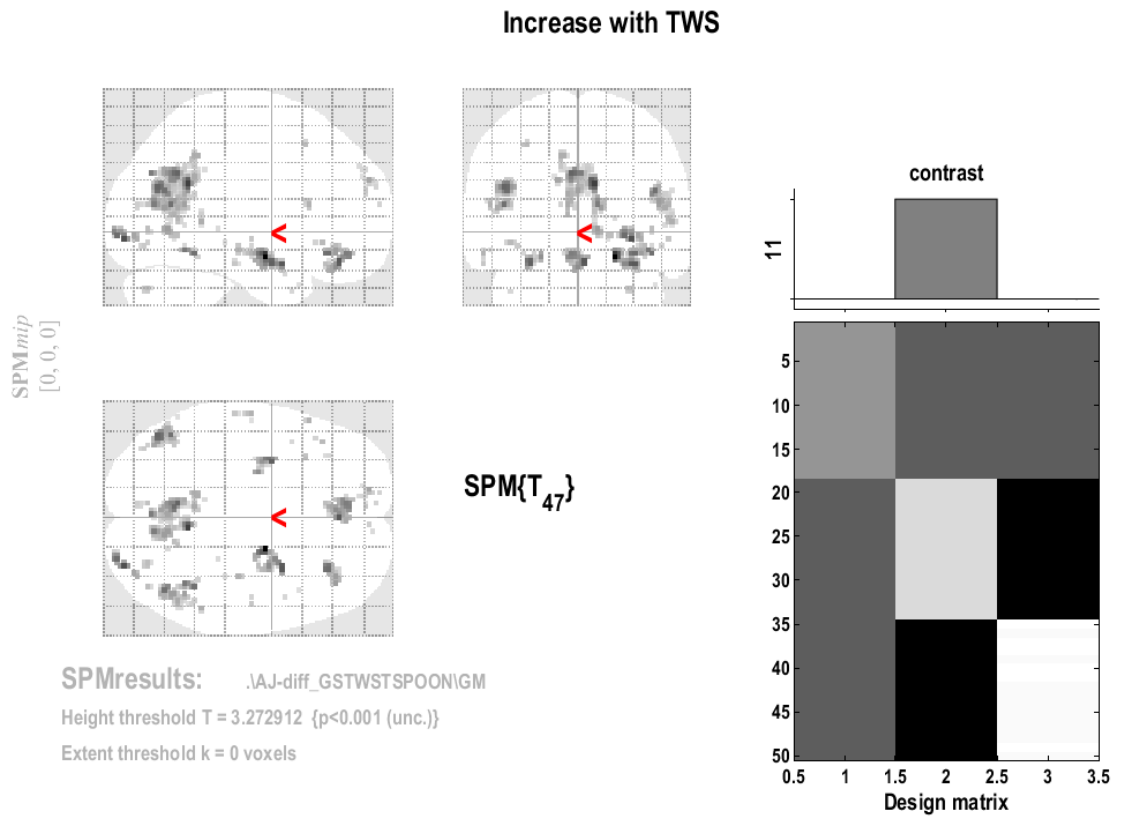
Degrees of freedom = [1.0, 47.0]
 FWHM = 4.8 4.7 5.7 mm mm mm; 2.4 2.4 2.8 {voxels}
 Volume: 312192 = 39024 voxels = 1427.2 resels
 Voxel size: 2.0 2.0 2.0 mm mm mm; (resel = 16.11 voxels)

Page 1



1

Figure C.2: Statistical parametric map showing regions where the contrast map *Faces > Scrambled Faces* is significantly increased by gaussian smoothing in WM, at the $p < 0.001$ uncorrected level.



Statistics: p -values adjusted for search volume

set-level		cluster-level				peak-level					mm mm mm		
p	c	$p_{\text{FWE-corr}}$	$q_{\text{FDR-corr}}$	k_E	p_{uncorr}	$p_{\text{FWE-corr}}$	$q_{\text{FDR-corr}}$	T	(Z_E)	p_{uncorr}			
0.000	54	0.000	0.000	80	0.000	0.000	0.000	7.98	6.32	0.000	20	-6	-16
						0.006	0.010	6.01	5.15	0.000	32	4	-20
						0.201	0.054	5.00	4.45	0.000	30	-4	-18
		0.014	0.004	41	0.001	0.001	0.006	6.50	5.46	0.000	8	-52	26
						1.000	0.537	3.70	3.45	0.000	4	-54	34
		0.362	0.092	16	0.019	0.003	0.010	6.20	5.27	0.000	30	-90	-6
		0.000	0.000	83	0.000	0.005	0.010	6.08	5.19	0.000	2	38	-18
						0.070	0.027	5.31	4.67	0.000	-6	42	-14
						0.988	0.324	3.97	3.67	0.000	-6	30	-20
		0.004	0.001	52	0.000	0.010	0.013	5.87	5.06	0.000	-30	-2	-20
						0.333	0.079	4.85	4.34	0.000	-24	-10	-16
		0.000	0.000	184	0.000	0.013	0.014	5.80	5.01	0.000	-6	-58	32
						0.067	0.027	5.32	4.68	0.000	0	-74	32
						0.654	0.154	4.51	4.09	0.000	-2	-68	22
		0.000	0.000	102	0.000	0.015	0.014	5.75	4.98	0.000	-46	-70	24
						0.030	0.018	5.56	4.85	0.000	-46	-62	14
						0.998	0.419	3.84	3.56	0.000	-42	-60	22
		0.014	0.004	41	0.001	0.021	0.017	5.66	4.92	0.000	32	32	-14
						0.504	0.124	4.66	4.20	0.000	40	36	-12
		0.593	0.156	12	0.038	0.034	0.018	5.52	4.82	0.000	42	-48	-14

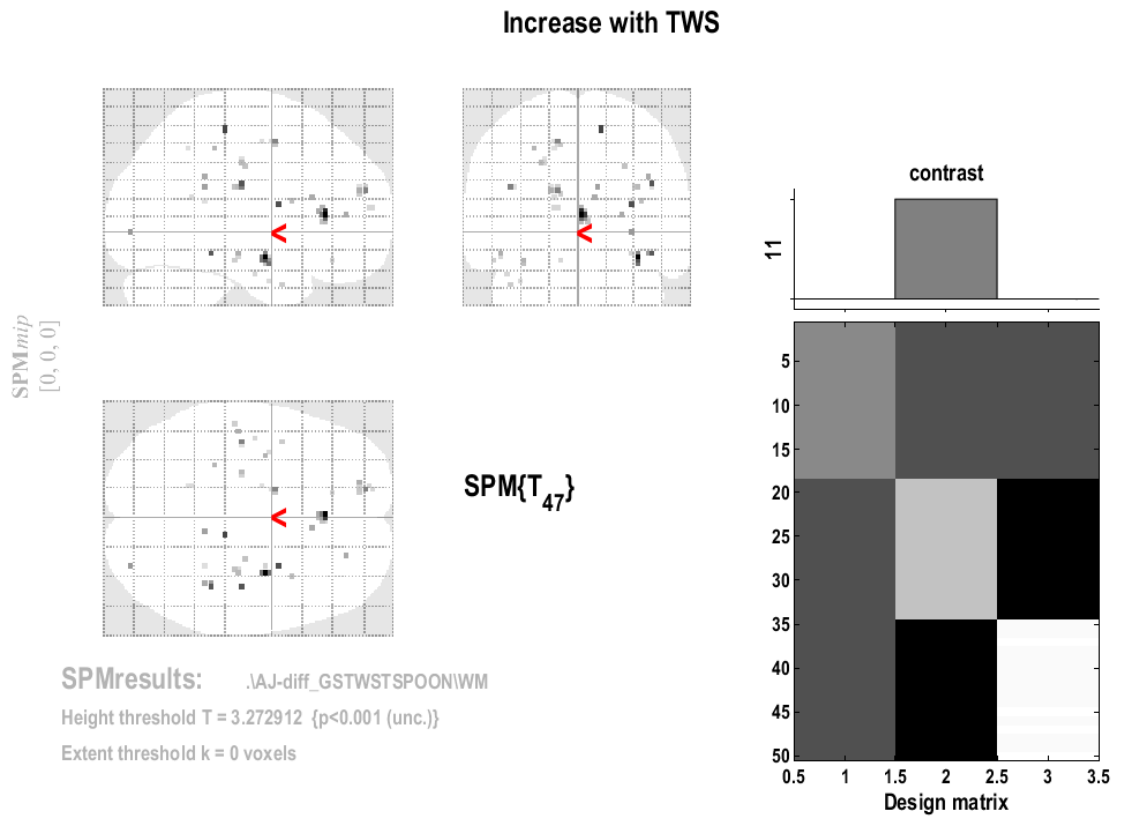
table shows 3 local maxima more than 8.0mm apart

Height threshold: $T = 3.27$, $p = 0.001$ (1.000)
 Extent threshold: $k = 0$ voxels
 Expected voxels per cluster, $\langle k \rangle = 2.683$
 Expected number of clusters, $\langle c \rangle = 23.95$
 FWEp: 5.407, FDRp: 5.266, FWEc: 41, FDRc: 25

Degrees of freedom = [1.0, 47.0]
 FWHM = 5.9 5.6 6.5 mm mm mm; 2.9 2.8 3.2 {voxels}
 Volume: 381008 = 47626 voxels = 778.7 resels
 Voxel size: 2.0 2.0 2.0 mm mm mm; (resel = 26.46 voxels)
 Page 1



Figure C.3: Statistical parametric map showing regions where the contrast map *Faces > Scrambled Faces* is significantly increased by TWS in GM, at the $p < 0.001$ uncorrected level.



Statistics: p -values adjusted for search volume

set-level		cluster-level				peak-level					mm mm mm		
p	c	$p_{\text{FWE-corr}}$	$q_{\text{FDR-corr}}$	k_E	p_{uncorr}	$p_{\text{FWE-corr}}$	$q_{\text{FDR-corr}}$	T	(Z_E)	p_{uncorr}			
0.152	33	0.564	0.418	8	0.031	0.494	0.549	4.67	4.21	0.000	34	-6	-16
		0.158	0.209	14	0.006	0.500	0.549	4.67	4.21	0.000	0	30	8
		0.999	0.418	2	0.251	0.939	0.829	4.23	3.87	0.000	12	-30	58
		1.000	0.418	1	0.418	0.964	0.829	4.16	3.82	0.000	30	2	14
		0.999	0.418	2	0.251	0.971	0.829	4.14	3.80	0.000	42	-20	26
		0.999	0.418	2	0.251	0.979	0.829	4.10	3.77	0.000	42	-38	-14
		0.999	0.418	2	0.251	0.999	0.949	3.85	3.57	0.000	-42	-20	24
		0.999	0.418	2	0.251	0.999	0.949	3.85	3.57	0.000	-14	54	22
		0.951	0.418	4	0.111	0.999	0.949	3.84	3.57	0.000	-14	0	50
		1.000	0.418	1	0.418	1.000	0.949	3.71	3.45	0.000	30	-86	-2
		1.000	0.418	1	0.418	1.000	0.949	3.66	3.41	0.000	10	-42	24
		1.000	0.418	1	0.418	1.000	0.949	3.62	3.38	0.000	8	22	18
		1.000	0.418	1	0.418	1.000	0.949	3.62	3.38	0.000	40	-42	30
		1.000	0.418	1	0.418	1.000	0.949	3.61	3.37	0.000	24	42	8
		0.880	0.418	5	0.078	1.000	0.949	3.60	3.37	0.000	-18	50	22
		0.999	0.418	2	0.251	1.000	0.949	3.59	3.35	0.000	-48	-22	-14
		0.999	0.418	2	0.251	1.000	0.949	3.56	3.34	0.000	-34	-6	-18
		1.000	0.418	1	0.418	1.000	0.949	3.54	3.31	0.000	-28	-36	46
		0.988	0.418	3	0.163	1.000	0.949	3.52	3.30	0.000	-24	-20	38
		0.988	0.418	3	0.163	1.000	0.949	3.52	3.30	0.000	34	-22	24

table shows 3 local maxima more than 8.0mm apart

Height threshold: $T = 3.27$, $p = 0.001$ (1.000)
Extent threshold: $k = 0$ voxels
Expected voxels per cluster, $\langle k \rangle = 1.633$
Expected number of clusters, $\langle c \rangle = 27.13$
FWEp: 5.349, FDRp: Inf, FWEc: Inf, FDRc: Inf

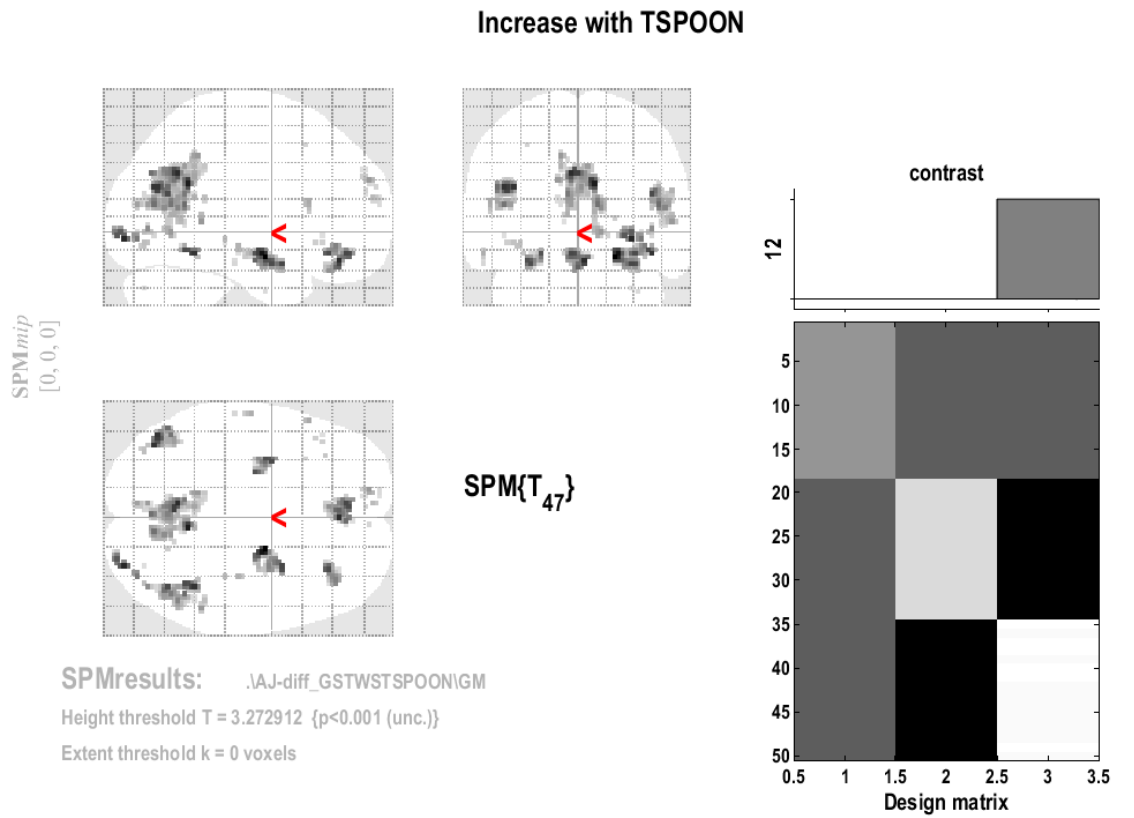
Degrees of freedom = [1.0, 47.0]
FWHM = 4.8 4.7 5.7 mm mm mm; 2.4 2.4 2.8 {voxels}
Volume: 312192 = 39024 voxels = 1427.2 resels
Voxel size: 2.0 2.0 2.0 mm mm mm; (resel = 16.11 voxels)

Page 1

< >

1

Figure C.4: Statistical parametric map showing regions where the contrast map *Faces > Scrambled Faces* is significantly increased by TWS in WM, at the $p < 0.001$ uncorrected level.



Statistics: p -values adjusted for search volume

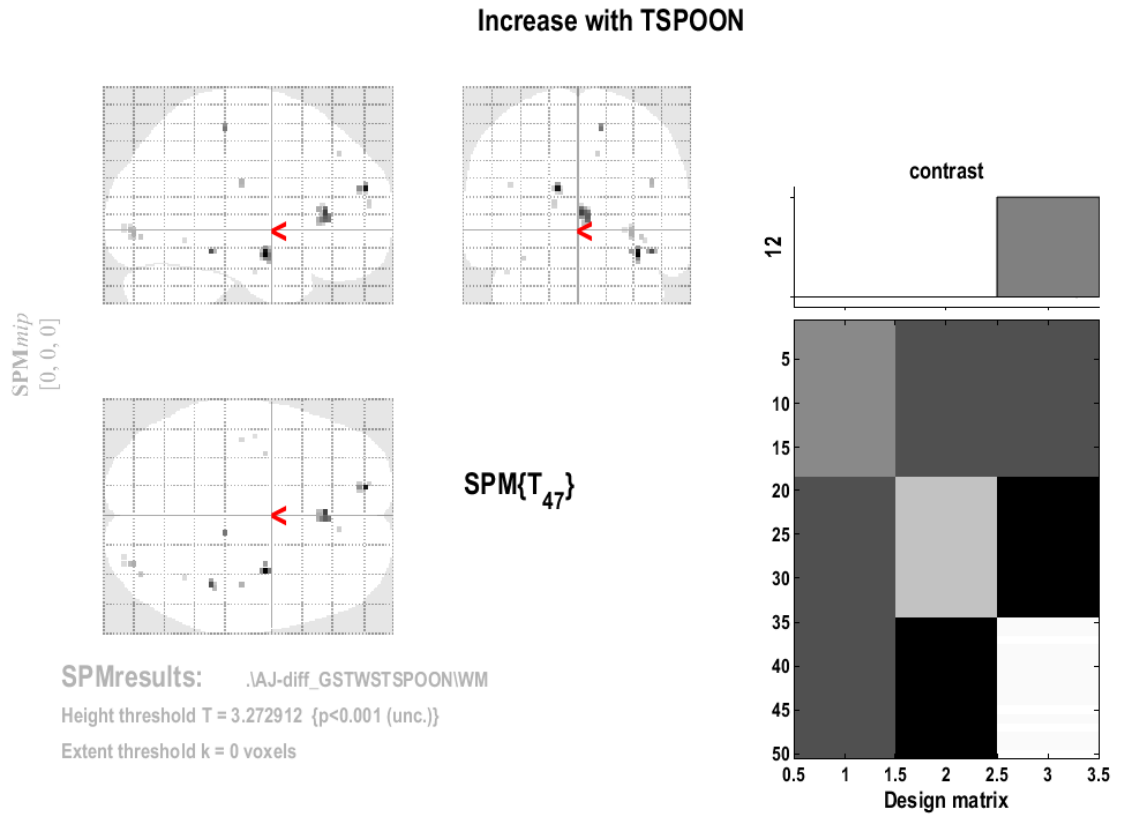
set-level		cluster-level				peak-level					mm mm mm		
p	c	$p_{FWE-corr}$	$q_{FDR-corr}$	k_E	p_{uncorr}	$p_{FWE-corr}$	$q_{FDR-corr}$	T	(Z_E)	p_{uncorr}			
0.001	41	0.000	0.000	118	0.000	0.000	0.002	7.00	5.76	0.000	20	-6	-16
						0.018	0.010	5.70	4.94	0.000	30	4	-20
						0.399	0.063	4.77	4.29	0.000	30	-4	-18
						0.001	0.005	6.43	5.42	0.000	8	-52	26
						0.003	0.006	6.21	5.28	0.000	-6	-58	32
		0.362	0.070	16	0.019	0.157	0.034	5.07	4.51	0.000	0	-74	32
						0.003	0.006	6.27	5.32	0.000	30	-90	-6
						0.004	0.006	6.15	5.24	0.000	2	38	-18
						0.018	0.010	5.70	4.95	0.000	-6	42	-14
						0.640	0.111	4.52	4.10	0.000	-4	32	-24
		0.000	0.000	136	0.000	0.005	0.006	6.06	5.19	0.000	-40	-72	24
						0.139	0.032	5.11	4.53	0.000	-50	-64	24
						0.210	0.040	4.99	4.44	0.000	-46	-62	14
						0.006	0.006	6.03	5.16	0.000	42	-48	-14
						0.019	0.010	5.69	4.94	0.000	32	32	-14
		0.277	0.056	18	0.014	0.396	0.063	4.77	4.29	0.000	38	36	-10
						0.005	0.001	4.99	4.44	0.000	-30	-2	-20
						0.019	0.010	5.68	4.93	0.000	-24	-12	-14
						0.035	0.013	5.51	4.82	0.000	42	-64	20
						0.000	0.000	5.63	4.90	0.000	46	-54	14
		0.000	0.000	134	0.000	0.023	0.010	5.63	4.90	0.000			
						0.121	0.031	5.15	4.56	0.000			

table shows 3 local maxima more than 8.0mm apart

Height threshold: $T = 3.27$, $p = 0.001$ (1.000)
Extent threshold: $k = 0$ voxels
Expected voxels per cluster, $\langle k \rangle = 2.683$
Expected number of clusters, $\langle c \rangle = 23.95$
FWEp: 5.407, FDRp: 4.908, FWEc: 49, FDRc: 24

Degrees of freedom = [1.0, 47.0]
FWHM = 5.9 5.6 6.5 mm mm mm; 2.9 2.8 3.2 {voxels}
Volume: 381008 = 47626 voxels = 778.7 resels
Voxel size: 2.0 2.0 2.0 mm mm mm; (resel = 26.46 voxels)
Page 1

Figure C.5: Statistical parametric map showing regions where the contrast map *Faces > Scrambled Faces* is significantly increased by TSPOON in GM, at the $p < 0.001$ uncorrected level.

Statistics: p -values adjusted for search volume

set-level		cluster-level				peak-level					mm mm mm		
p	c	$p_{\text{FWE-corr}}$	$q_{\text{FDR-corr}}$	k_E	p_{uncorr}	$p_{\text{FWE-corr}}$	$q_{\text{FDR-corr}}$	T	(Z_E)	p_{uncorr}			
0.985	17	0.245	0.088	12	0.010	0.176	0.219	4.98	4.44	0.000	34	-6	-16
		0.673	0.233	7	0.041	0.325	0.219	4.80	4.31	0.000	-14	54	22
		0.019	0.012	24	0.001	0.793	0.379	4.44	4.04	0.000	0	30	8
		0.951	0.378	4	0.111	0.872	0.379	4.34	3.96	0.000	42	-38	-14
		0.999	0.418	2	0.251	0.983	0.500	4.08	3.76	0.000	12	-30	56
		1.000	0.418	1	0.418	1.000	0.774	3.79	3.52	0.000	30	-6	-14
		0.782	0.239	6	0.056	1.000	0.817	3.65	3.41	0.000	30	-84	-4
		0.999	0.418	2	0.251	1.000	0.817	3.63	3.39	0.000	42	-20	26
		1.000	0.418	1	0.418	1.000	0.957	3.48	3.26	0.001	36	-80	-6
		0.999	0.418	2	0.251	1.000	0.957	3.42	3.22	0.001	-16	56	14
		1.000	0.418	1	0.418	1.000	0.957	3.41	3.20	0.001	10	38	42
		1.000	0.418	1	0.418	1.000	0.957	3.40	3.20	0.001	-34	-6	-18
		1.000	0.418	1	0.418	1.000	0.957	3.35	3.16	0.001	-42	-20	24
		1.000	0.418	1	0.418	1.000	0.957	3.32	3.13	0.001	38	-54	-8
		1.000	0.418	1	0.418	1.000	0.957	3.32	3.13	0.001	30	-90	0
		1.000	0.418	1	0.418	1.000	0.957	3.30	3.11	0.001	-44	-12	-26
		1.000	0.418	1	0.418	1.000	0.957	3.29	3.11	0.001	26	-90	-2

table shows 3 local maxima more than 8.0mm apart

Height threshold: $T = 3.27$, $p = 0.001$ (1.000)
 Extent threshold: $k = 0$ voxels
 Expected voxels per cluster, $\langle k \rangle = 1.633$
 Expected number of clusters, $\langle c \rangle = 27.13$
 FWEp: 5.349, FDRp: Inf, FWEc: 24, FDRc: 24

Degrees of freedom = [1.0, 47.0]
 FWHM = 4.8 4.7 5.7 mm mm mm; 2.4 2.4 2.8 {voxels}
 Volume: 312192 = 39024 voxels = 1427.2 resels
 Voxel size: 2.0 2.0 2.0 mm mm mm; (resel = 16.11 voxels)

Figure C.6: Statistical parametric map showing regions where the contrast map *Faces > Scrambled Faces* is significantly increased by TSPOON in WM, at the $p < 0.001$ uncorrected level.

Appendix D

Additional Results for Discussion

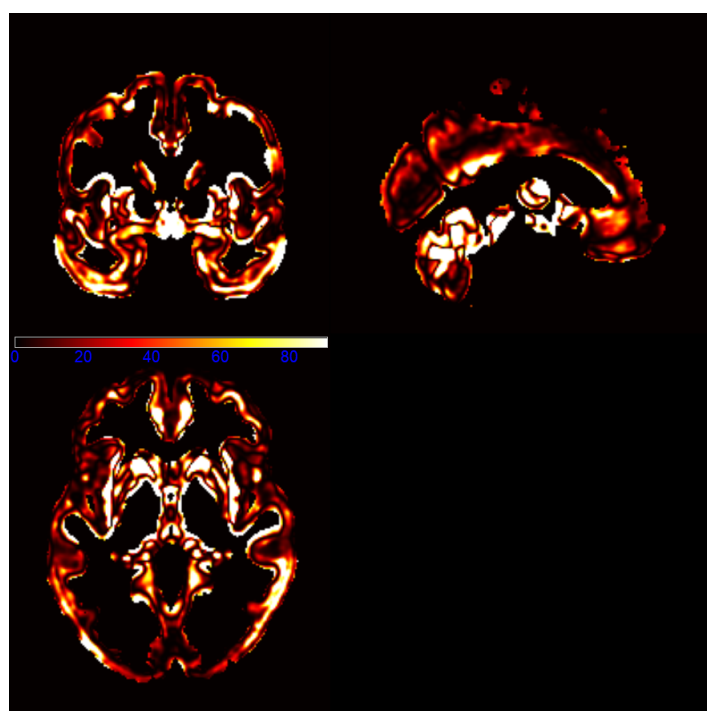


Figure D.1: Statistical parametric maps showing regions where $R2^*$ is affected by the difference between TWS and TSPOON in gray matter.

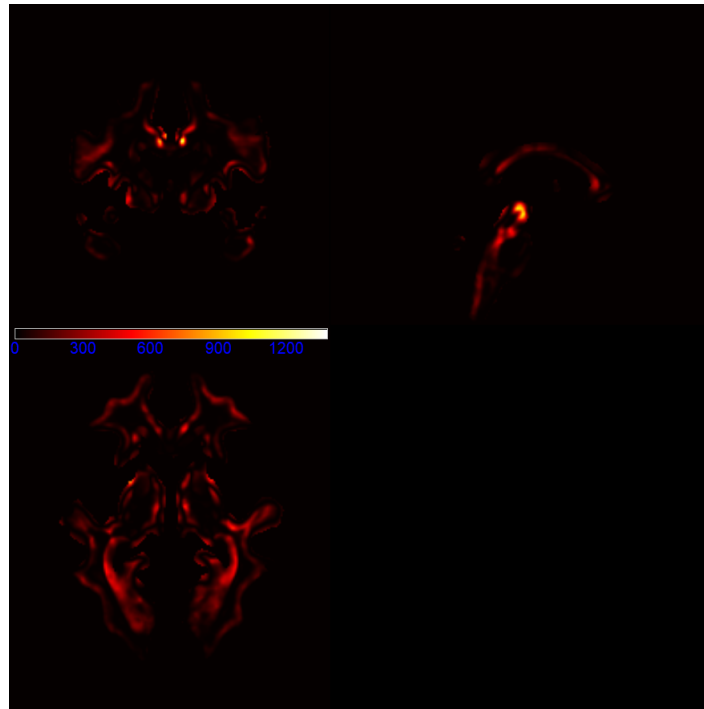


Figure D.2: Statistical parametric maps showing regions where $R2^*$ is affected by the difference between TWS and TSPOON in white matter.

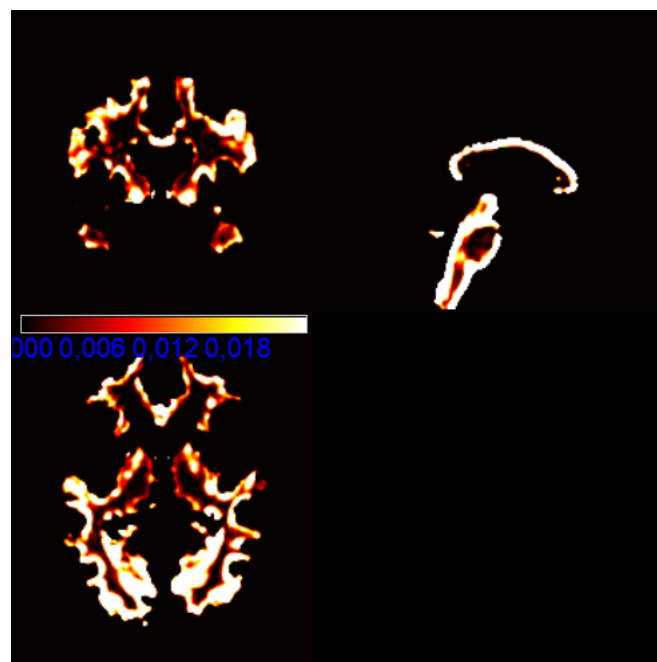


Figure D.3: Quantitative map for subject 1 and MTsat qMRI parameter showing the difference TWS and TSPOON in the white matter.

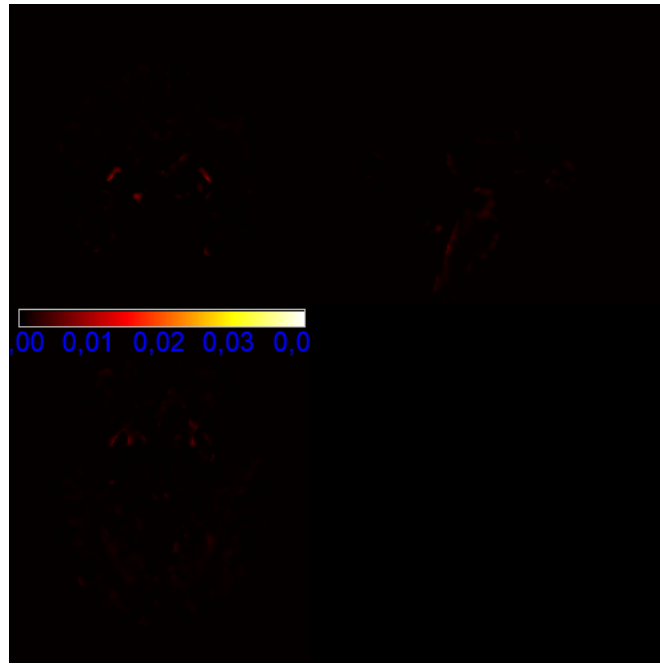


Figure D.4: Quantitative map for subject 1 and R2* qMRI parameter showing the difference TWS and TSPOON in the white matter.

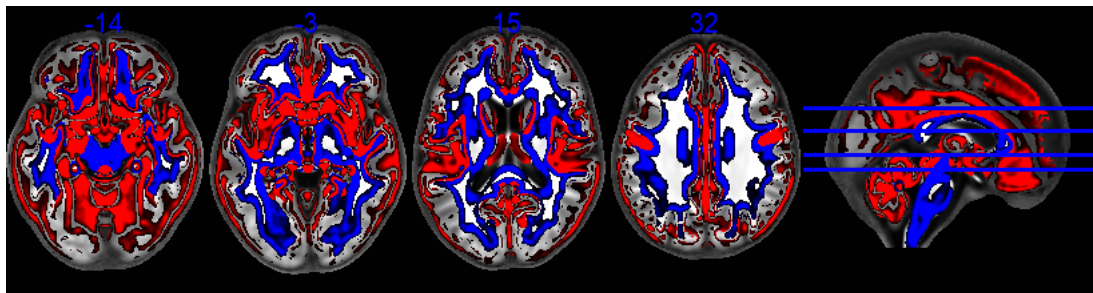


Figure D.5: Statistical parametric maps showing regions where MTsat is significantly affected by the difference between TWS and TSPOON, at the $p < 0.05$ FWE corrected level. Regions in red correspond to GM, and regions in blue correspond to WM. Axial sections are displayed in a multislice format.

Index

- κ : Cohen's Kappa, 27
- AFNI: Analysis of Functional NeuroImages, 4
- AR+: Age-related Increase, 36
- AR-: Age-related Decrease, 36
- AR: Age-related Effect, 36
- BIDS: Brain Imaging Data Structure, 15
- BOLD: Blood-Oxygen-Level-Dependent, 5
- CSF: Cerebrospinal Fluid, 1
- CT: Computed Tomography, 3
- DARTEL: Diffeomorphic Anatomical
Registration Through Exponentiated
Lie Algebra, 12
- DC: Dice Coefficient, 27
- DMN: Default Mode Network, 5
- DTI: Diffusion Tensor Imaging, 6
- DWI: Diffusion Weighted Imaging, 5
- EEG: ElectroEncephaloGraphy, 19
- FA: Fractional Anisotropy, 6
- FCD: Focal Cortical Dysplasia, 9
- FDR: False Discovery Rate, 17
- fMRI: functional MRI, 3
- FMRIB: Oxford Centre for Functional MRI of
the Brain, 4
- FSL: FMRIB Software Library, 4
- FWE: Family wise error, 42
- FWE: Family-Wise Error, 16
- FWER: Family-Wise Error Rate, 17
- FWHM: Full Width at Half Maximum, 18
- GBM: Glioblastoma, 6
- GLM: General Linear Model, 10
- GM: Gray Matter, 1
- GS: Gaussian Smoothing, 14
- HGGs: High-Grade Gliomas, 8
- hMRI: in vivo Histology MRI, 8
- HRF: Hemodynamic Response Function, 20
- ICV: IntraCranial Volume, 19
- Jl: Jaccard Index, 27
- MEG: MagnetoEncephaloGraphy, 19
- MMSE: Mini Mental State Examination, 15
- MNI: Montreal Neurological Institute, 11
- MPM: Multi-Parametric Mapping, 3
- MRI: Magnetic Resonance Imaging, 2
- MS: Multiple Sclerosis, 9
- MTsat: Magnetization Transfer Saturation, 7
- PCA: Principal Component Analysis, 6
- PD: Proton Density, 7
- PVE: Partial Volume Effect, 13
- qMRI: Quantitative MRI, 5
- qMRIs: Quantitative MRI Maps, 16
- R1: Longitudinal Relaxation Rate, 7
- R2*: Effective Transverse Relaxation Rate, 7
- RMSE: Root Mean Squared Error, 23
- rs-fMRI: resting-state fMRI, 5
- SN: Salience Network, 5
- SNR: Signal-to-Noise Ratio, 3
- SPM: Statistical Parametric Mapping toolbox, 4
- SPM: Statistical Paramter Map, 36
- T1w: T1-weighted, 8
- tb-fMRI: task-based fMRI, 5
- TIV: Total Intracranial Volume, 16
- TLE: Temporal Lobe Epilepsy, 9
- TPM: Tissue Probability Map, 22
- TR: Repetition Time, 10
- TSPOON: Tissue-Specific smOOthing
CompeNsated, 14
- TWS: Tissue-Weighted Smoothing, 14
- VBA: Voxel-Based Analyses, 23
- VBM: Voxel-Based Morphometry, 16
- VBQ: Voxel-Based Quantification, 16, 21
- w-qMaps: Warped Quantitative Maps, 16
- WM: White Matter, 1
- WTA: Winner-Takes-All, 19

Bibliography

- [1] C. F. Gauss, *Theoria motus corporum coelestium in sectionibus conicis solem ambientium*. Hamburg: Perthes et Besser, 1809, book ID: 000391854. [Online]. Available: <https://dspace.library.uu.nl/handle/1874/352162>
- [2] M. F. Callaghan, P. Freund, B. Draganski, E. Anderson, M. Cappelletti, R. Chowdhury, J. Diedrichsen, and al., "Widespread age-related differences in the human brain microstructure revealed by quantitative magnetic resonance imaging," *Neurobiology of Aging*, vol. 35, no. 8, pp. 1862–1872, August 2014.
- [3] E. G. Figueiredo, N. N. Rabelo, and L. C. Welling, *Brain Anatomy and Neurosurgical Approaches: A Practical, Illustrated, Easy-to-Use Guide*, 1st ed. Cham: Springer International Publishing, 2023.
- [4] E. R. Kandel, J. H. Schwartz, T. M. Jessell, and S. Mack, *Principles of Neural Science*, 5th ed. New York: McGraw-Hill, 2012.
- [5] H. O. de Beeck and C. Nakatani, *Introduction to Human Neuroimaging*, ser. Higher Education from Cambridge University Press. Cambridge: Cambridge University Press, 2019.
- [6] G. Drewes, E.-M. Mandelkow, K. Baumann, J. Goris, W. Merlevede, and E. Mandelkow, "Dephosphorylation of tau protein and alzheimer paired helical filaments by calcineurin and phosphatase-2a," *FEBS Letters*, vol. 336, no. 3, pp. 425–432, 1993.
- [7] F. Weber and H. Knopf, "Incidental findings in magnetic resonance imaging of the brains of healthy young men," *Journal of the Neurological Sciences*, vol. 240, no. 1–2, pp. 81–84, 2006. [Online]. Available: <https://doi.org/10.1016/j.jns.2005.09.008>
- [8] R. Kanai, B. Bahrami, B. C. Duchaine, A. Janik, M. J. Banissy, and G. Rees, "Online social network size is reflected in human brain structure," *Proceedings of the Royal Society B: Biological Sciences*, vol. 279, no. 1732, pp. 1327–1334, 2012. [Online]. Available: <https://doi.org/10.1098/rspb.2011.1959>
- [9] R. W. McGugin, A. Roche, J. Ma, and I. Gauthier, "Challenges in replication: Does amygdala gray matter volume relate to social network size?" *Cognitive, Affective & Behavioral Neuroscience*, vol. 24, no. 4, pp. 707–719, 2024. [Online]. Available: <https://doi.org/10.3758/s13415-024-01185-w>
- [10] A. Owen, M. Coleman, M. Boly, M. Davis, S. Laureys, and J. Picard, "Detecting awareness in the vegetative state," *Science*, September 2006. [Online]. Available: <https://doi.org/10.1126/science.1130197>
- [11] C. S. Kidwell, J. A. Chalela, J. L. Saver, S. Starkman, M. D. Hill, A. M. Demchuk, J. A. Butman, and et al., "Comparison of mri and ct for detection of acute intracerebral hemorrhage," *JAMA*, vol. 292, no. 15, pp. 1823–1830, 2004. [Online]. Available: <https://doi.org/10.1001/jama.292.15.1823>
- [12] P. Kaur and G. S. Gaba, "Computational neuroscience models and tools: A review," in *Bio-Inspired Neurocomputing*, A. K. Bhoi, P. K. Mallick, C.-M. Liu, and V. E. Balas, Eds. Singapore: Springer, 2021, pp. 403–417.

- [13] A. N. Pisarchik, "Computational and mathematical methods for neuroscience," *Applied Sciences*, vol. 14, no. 23, p. 11296, January 2024.
- [14] D. Bzdok, "Classical statistics and statistical learning in imaging neuroscience," *Frontiers in Neuroscience*, vol. 11, October 2017.
- [15] Wikipedia contributors, "Smoothing," <https://en.wikipedia.org/w/index.php?title=Smoothing&oldid=1259180295>, November 2024, accessed: 23 November 2024.
- [16] A. Kawaguchi, "Statistical analysis of brain mri data," *Japanese Journal of Biometrics*, vol. 33, no. 2, pp. 145–174, 2013.
- [17] GitHub contributors, "Spm toolboxes," <https://github.com/spm-toolboxes>, December 2024, accessed: 25 December 2024.
- [18] FSL contributors, "Fsl," <https://fsl.fmrib.ox.ac.uk/fsl/docs/#/>, December 2024, accessed: 26 December 2024.
- [19] R. Cox, "Afni," <https://github.com/afni/afni>, December 2024, accessed: 19 December 2024.
- [20] C. Candemir, "Spatial smoothing effect on group-level functional connectivity during resting and task-based fmri," *Sensors*, vol. 23, no. 13, p. 5866, January 2023.
- [21] F. M. Cozzi, R. C. Mayrand, Y. Wan, and S. J. Price, "Predicting glioblastoma progression using mr diffusion tensor imaging: A systematic review," *Journal of Neuroimaging: Official Journal of the American Society of Neuroimaging*, vol. 35, no. 1, p. e13251, 2025. [Online]. Available: <https://doi.org/10.1111/jon.13251>
- [22] N. Weiskopf, S. Mohammadi, A. Lutti, and M. F. Callaghan, "Advances in mri-based computational neuroanatomy: From morphometry to in-vivo histology," *Current Opinion in Neurology*, vol. 28, no. 4, p. 313, August 2015.
- [23] K. Tabelow, E. Balteau, J. Ashburner, M. F. Callaghan, B. Draganski, G. Helms, and F. Kherif, "hmri – a toolbox for quantitative mri in neuroscience and clinical research," *NeuroImage*, vol. 194, pp. 191–210, January 2019.
- [24] GitHub, "hmri-group," Online resource, <https://github.com/hMRI-group>. Consulted on the 21st of October, 2024.
- [25] N. Weiskopf, J. Suckling, G. Williams, M. M. Correia, B. Inkster, R. Tait, C. Ooi, E. T. Bullmore, and A. Lutti, "Quantitative multi-parameter mapping of r1, pd*, mt, and r2* at 3t: A multi-center validation," *Frontiers in Neuroscience*, vol. 7, p. 95, 2013.
- [26] G. Reuter, E. Lommers, E. Balteau, J. Simon, C. Phillips, F. Scholtes, D. Martin, A. Lombard, and P. Maquet, "Multiparameter quantitative histological mri values in high-grade gliomas: A potential biomarker of tumor progression," *Neuro-Oncology Practice*, August 2020.
- [27] N. Vandeleene, C. Guillemin, S. Dauby, F. Requier, M. Charonitis, D. Chylinski, E. Balteau, P. Maquet, E. Lommers, and C. Phillips, "Using quantitative magnetic resonance imaging to track cerebral alterations in multiple sclerosis brain: A longitudinal study," *Brain and Behavior*, April 2023.
- [28] A. Seiler, U. Noth, P. Hok, A. Reilander, M. Maiworm, S. Baudrexel, and S. Meuth, "Multiparametric quantitative mri in neurological diseases," *Frontiers in Neurology*, vol. 12, p. 640239, 2021.
- [29] K. J. Friston, S. Williams, R. Howard, R. S. Frackowiak, and R. Turner, "Movement-related effects in fmri time-series," *Magnetic Resonance in Medicine*, vol. 35, no. 3, pp. 346–355, March 1996.

- [30] Wikibooks contributors, "Neuroimaging data processing/processing/steps/realignment," https://en.wikibooks.org/wiki/Neuroimaging_Data_Processing/Processing/Steps/Realignment, December 2024, accessed: 25 December 2024.
- [31] Wikibooks Contributors, "Neuroimaging data processing/processing/steps/slice timing," https://en.wikibooks.org/wiki/Neuroimaging_Data_Processing/Processing/Steps/Slice_Timing, December 2024, accessed: 25 December 2024.
- [32] R. Sladky, K. J. Friston, J. Trostl, R. Cunnington, E. Moser, and C. Windischberger, "Slice-timing effects and their correction in functional mri," *NeuroImage*, vol. 58, no. 2, pp. 588–594, September 2011.
- [33] J. Ashburner and K. Friston, "Multimodal image coregistration and partitioning—a unified framework," *NeuroImage*, vol. 6, no. 3, pp. 209–217, October 1997.
- [34] Wikibooks contributors, "Neuroimaging data processing/processing/steps/coregistration and normalization," https://en.wikibooks.org/wiki/Neuroimaging_Data_Processing/Processing/Steps/Coregistration_and_Normalization, December 2024, accessed: 25 December 2024.
- [35] J. Ashburner and K. J. Friston, "Unified segmentation," *NeuroImage*, vol. 26, no. 3, pp. 839–851, July 2005.
- [36] Wikibooks contributors, "Neuroimaging data processing/processing/steps/tissue segmentation," https://en.wikibooks.org/wiki/Neuroimaging_Data_Processing/Processing/Steps/Tissue_Segmentation, December 2024, accessed: 25 December 2024.
- [37] FreeSurfer contributors, "Freesurfer," <https://surfer.nmr.mgh.harvard.edu>, December 2024, accessed: 25 December 2024.
- [38] J. Ashburner and K. J. Friston, "Nonlinear spatial normalization using basis functions," *Human Brain Mapping*, vol. 7, no. 4, pp. 254–266, 1999.
- [39] J. Talairach and G. Szikla, "Application of stereotactic concepts to the surgery of epilepsy," in *Advances in Stereotactic and Functional Neurosurgery 4*, F. J. Gillingham, J. Gybels, E. Hitchcock, G. F. Rossi, and G. Szikla, Eds. Vienna: Springer, 1980, pp. 35–54. [Online]. Available: https://doi.org/10.1007/978-3-7091-8592-6_5
- [40] G. Grabner, A. L. Janke, M. M. Budge, D. Smith, J. Pruessner, and D. L. Collins, "Symmetric atlas and model based segmentation: An application to the hippocampus in older adults," in *Medical Image Computing and Computer-Assisted Intervention – MICCAI 2006*, R. Larsen, M. Nielsen, and J. Sporring, Eds. Berlin, Heidelberg: Springer, 2006, pp. 58–66. [Online]. Available: https://doi.org/10.1007/11866763_8
- [41] A. Giff, G. Noren, J. Magnotti, A. C. Lopes, M. C. Batistuzzo, M. Hoexter, and B. Greenberg, "Spatial normalization discrepancies between native and mni152 brain template scans in gamma ventral capsulotomy patients," *Psychiatry Research: Neuroimaging*, vol. 329, p. 111595, March 2023.
- [42] R. A. Poldrack, J. A. Mumford, and T. E. Nichols, *Handbook of Functional MRI Data Analysis*. Cambridge University Press, 2011. [Online]. Available: <https://books.google.com/books?id=VjwBnVRwuD8C&pg=PA17>
- [43] J. Ashburner, "A fast diffeomorphic image registration algorithm," *NeuroImage*, vol. 38, no. 1, pp. 95–113, October 2007. [Online]. Available: <https://doi.org/10.1016/j.neuroimage.2007.07.007>

- [44] Wikipedia contributors, "Gaussian blur," https://en.wikipedia.org/w/index.php?title=Gaussian_blur&oldid=1258405901, November 2024, accessed: 19 November 2024.
- [45] E. J. Hoffman, S.-C. Huang, and M. E. Phelps, "Quantitation in positron emission computed tomography: 1. effect of object size," *Journal of Computer Assisted Tomography*, vol. 3, no. 3, p. 299, Jun 1979.
- [46] C. C. Meltzer, J. P. Leal, H. S. Mayberg, H. N. J. Wagner, and J. J. Frost, "Correction of pet data for partial volume effects in human cerebral cortex by mr imaging," *Journal of Computer Assisted Tomography*, vol. 14, no. 4, p. 561, Aug 1990.
- [47] B. Draganski, J. Ashburner, C. Hutton, F. Kherif, R. S. J. Frackowiak, G. Helms, and N. Weiskopf, "Regional specificity of mri contrast parameter changes in normal ageing revealed by voxel-based quantification (vbq)," *NeuroImage*, vol. 55, no. 4, pp. 1423–1434, April 2011.
- [48] J. E. Lee, M. K. Chung, M. Lazar, M. B. DuBray, J. Kim, E. D. Bigler, J. E. Lainhart, and A. L. Alexander, "A study of diffusion tensor imaging by tissue-specific, smoothing-compensated voxel-based analysis," *NeuroImage*, vol. 44, no. 3, pp. 870–883, February 2009.
- [49] K. J. Gorgolewski, F. Alfaro-Almagro, T. Auer, P. Bellec, M. Capotă, M. M. Chakravarty, N. W. Churchill, and et al., "Bids apps: Improving ease of use, accessibility, and reproducibility of neuroimaging data analysis methods," *PLOS Computational Biology*, vol. 13, no. 3, p. e1005209, March 2017.
- [50] Brain Imaging Data Structure contributors, "Index," <https://bids.neuroimaging.io/index>, November 2024, accessed: 25 December 2024.
- [51] The FIL Methods Group (and honorary members). (2021) Spm12 manual. Functional Imaging Laboratory (Wellcome Centre for Human Neuroimaging). <https://www.fil.ion.ucl.ac.uk/spm/>. Viewed on the 3th of December, 2024.
- [52] D. G. Wakeman and R. N. Henson, "A multi-subject, multi-modal human neuroimaging dataset," *Scientific Data*, vol. 2, p. 150001, 2015. [Online]. Available: <https://doi.org/10.1038/sdata.2015.1>
- [53] D. Wakeman and R. Henson, ""multisubject, multimodal face processing"," 2024.
- [54] N. Belyi, C. Guillemin, E. Pommier, G. Hammad, and C. Phillips, "Bidsme: Expandable bids-ifier of brain imagery datasets," *Journal of Open Source Software*, vol. 8, no. 92, p. 5575, Dec 2023. [Online]. Available: <https://doi.org/10.21105/joss.05575>
- [55] "spm/multimodalscripts," MATLAB, 2019, reprint, SPM, 6 October 2020. <https://github.com/spm/MultimodalScripts>.
- [56] "imgaussfilt3," 2024, accessed: December 23, 2024. [Online]. Available: <https://nl.mathworks.com/help/images/ref/imgaussfilt3.html>
- [57] Y. Zhang, M. Brady, and S. Smith, "Segmentation of brain mr images through a hidden markov random field model and the expectation-maximization algorithm," *IEEE Transactions on Medical Imaging*, vol. 20, no. 1, pp. 45–57, January 2001.
- [58] J. M. Bland and D. G. Altman, "Statistical methods for assessing agreement between two methods of clinical measurement," *The Lancet*, vol. 327, no. 8476, pp. 307–310, February 1986.
- [59] "Jaccard index," Online resource, Wikipedia, https://en.wikipedia.org/wiki/Jaccard_index. Viewed on the 25th of November, 2024.
- [60] "Dice-sorensen coefficient," Online resource, Wikipedia, https://en.wikipedia.org/wiki/Dice-S%C3%B8rensen_coefficient. Viewed on the 25th of November, 2024.

- [61] “Cohens kappa,” In Wikipedia, January 6 2025, https://en.wikipedia.org/wiki/Cohen%27s_kappa.
- [62] T. Mitchell, D. B. Archer, W. T. Chu, S. A. Coombes, S. Lai, B. J. Wilkes, and N. R. McFarland, “Neurite orientation dispersion and density imaging (noddi) and free-water imaging in parkinsonism,” *Human Brain Mapping*, vol. 40, no. 17, pp. 5094–5107, Dec 2019. [Online]. Available: <https://doi.org/10.1002/hbm.24760>
- [63] SPM Developers, “spm/src/spm_conv_vol.c at main · spm/spm,” https://github.com/spm/spm/blob/main/src/spm_conv_vol.c, accessed: December 15, 2024.